TITANIUM IN QUARTZ DURING GROWTH AND DEFORMATION UNDER HYDROTHERMAL-MAGMATIC CONDITIONS

by

MARISA DAWN ACOSTA

A DISSERTATION

Presented to the Department of Earth Sciences
and the Graduate School of the University of Oregon
in partial fulfillment of the requirements
for the degree of
Doctor of Philosophy

June 2020

DISSERTATION APPROVAL PAGE

Student: Marisa Dawn Acosta

Title: Titanium in Quartz during Growth and Deformation under Hydrothermal-Magmatic Conditions

This dissertation has been accepted and approved in partial fulfillment of the requirements for the Doctor of Philosophy degree in the Department of Earth Sciences by:

James Watkins	Co-chairperson
Mark Reed	Co-chairperson
Thomas Giachetti	Core Member
John Dilles	Core Member
Marina Guenza	Institutional Representative

and

Kate Mondloch Interim Vice Provost and Dean of the Graduate School

Original approval signatures are on file with the University of Oregon Graduate School.

Degree awarded June 2020

DISSERTATION ABSTRACT

Marisa Dawn Acosta

Doctor of Philosophy

Department of Earth Sciences

June 2020

Title: Titanium in Quartz during Growth and Deformation under Hydrothermal-Magmatic Conditions

Titanium in quartz is a promising tool with which to investigate processes of quartz growth and deformation. In this dissertation, I present and interpret the results of experimentally synthesized Ti-doped quartz crystals and shed light on sources of complexity that arise during non-equilibrium growth at 800°C and 1 kbar. I use images of the Ti distributions in quartz from the Butte, Montana, porphyry Cu-Mo deposit to detail the sequence of events by which barren quartz and quartz-molybdenite veins are formed. I compare temperature estimates made with Ti concentrations to other independent methods of temperature estimates to show that the dark growth bands of CL-euhedral hydrothermal quartz record near-equilibrium growth and that the bright growth bands of CL-euhedral quartz are markers of disequilibrium "kinetic effects". Lastly, I present a possible mechanism for the formation of oscillatory CL-bright and -dark growth bands under constant pressure and temperature conditions at low supersaturation.

This dissertation includes previously published and unpublished co-authored material.

CURRICULUM VITAE

NAME OF AUTHOR: Marisa Dawn Acosta

GRADUATE AND UNDERGRADUATE SCHOOLS ATTENDED:

University of Oregon, Eugene, Oregon, USA
Western Washington University, Bellingham, Washington, USA
Clark College, Vancouver, Washington, USA

DEGREES AWARDED:

Doctor of Philosophy, Earth Sciences, 2020, University of Oregon
Bachelor of Sciences, Thesis Option, Geology, 2014, Western Washington University
Associate of Arts, 2009, Clark College

AREAS OF SPECIAL INTEREST:

Economic geology
Crystal growth

PROFESSIONAL EXPERIENCE:

Graduate Employee, University of Oregon, 2014-2020]

GRANTS, AWARDS, AND HONORS:

Earth Sciences Weiser Scholarship, University of Oregon, 2020

Earth Sciences Research Excellence Award, University of Oregon, 2020

Earth Sciences Smith Scholarship, University of Oregon, 2020

PUBLICATIONS:

Acosta M. D., Watkins J. M., Reed M. H., Donovan J. J. and DePaolo D. J. (2020) Ti-in-quartz: Evaluating the role of kinetics in high temperature crystal growth experiments. Geochim. Cosmochim. Acta 281, 149–167.

ACK.NOWLEDGMENTS

I thank my parents, Raquel and Donald Clavette, for their unfailing support. Because of their unwavering love, I have become the person I am today.

I thank my advisors, Mark Reed and James Watkins, for their mentorship. Because of Mark's 'splitting' and Jim's 'lumping', I have grown into the scientist I am today.

I thank John Donovan, for his encouragement and mentorship. John taught me to never be afraid to think outside the box.

I thank my partner, Casey Coyle, for standing by my side. Because of his unquestioning support, I was able to get this far.

I thank my committee members, John Dilles, Marina Guenza, and Thomas Giachetti. Their invaluable feedback and patience was instrumental in the completion of this dissertation.

I thank my office and lab members through the years: David Zakharov, Brennan O'Connoll, Madison Ball, Larry Syu-Heng Lai, Ryan Seward, and Ellen Olsen. Their laughter and camaraderie made graduate school fun.

I thank Montana Resources and the Washington Company for access to the mine and a transformative internship. I especially am indebted to Amanda Griffith for her invaluable input on the Butte system and her friendship. I also thank my mapping partner in the pit, Kyle Eastmann.

I thank the Department of Earth Sciences as a whole, and especially Marla Trox and Sandy Thoms. I have had many constructive conversations with faculty and graduate

students, especially Marli Miller, Paul Wallace, Josh Roering, Ray Weldon, and Lief Karlstrom.

I thank the faculty and staff at the Center for Advanced Materials Characterization in Oregon (CAMCOR), specifically Julie Chouinard, Kurt Langworthy, and Valerie Brogden.

I acknowledge the National Science Foundation for funding this research through grant number EAR1524665.

I dedicate this dissertation to my beloved cat, Archibald Catamungus. R.I.P.

TABLE OF CONTENTS

Chapter Page

Chapter Page

Chapter Page

LIST OF FIGURES

Figure Page

LIST OF TABLES

CHAPTER I
INTRODUCTION

Trace element concentrations in crystals have long been used as tools to reconstruct geological histories and the chemical evolution of natural systems. Key to the rigorous application of trace element systematics to natural systems is identifying whether or not a crystal grew at or near thermodynamic equilibrium, whether that initial equilibrium is preserved in the crystal, and whether or not a crystal has been deformed. In this dissertation, I identify conditions for deviation from equilibrium during Ti-doped quartz crystal growth and use trace Ti re-equilibration during high temperature recrystallization to constrain quartz vein formation processes.

Quartz is a common crustal mineral and is stable over a wide range of pressures and temperatures. It is an important component in igneous, metamorphic, and sedimentary systems. Due to its common occurrence, developing quantitative ways to use quartz trace element systematics to unravel earth system processes is a flourishing area of research. The titanium-in-quartz geothermobarometer, TitaniQ, uses Ti concentrations in quartz to constrain either the pressure or temperature of formation, provided the other can be constrained independently. However, application of TitaniQ to natural rocks has revealed complications, and various experiments designed to identify Ti equilibrium concentrations in quartz have yielded results that do not agree from one set of experiments to the next.

In Chapter II of this dissertation, I use scanning electron microscope images and Ti concentrations of experimentally grown hydrothermal quartz to assess the conditions at which deviations from equilibrium occur. Titanium concentrations in hydrothermal quartz grown in experiments conducted at 800°C and 1 kbar span the expected range of concentrations predicted by previous calibrations of TitaniQ. Detailed observations of quartz morphology and cathodoluminescent (CL) textures show that the use of anatase or rutile in experiments has a significant influence on the (re)crystallization pathways of the TiO_2 and SiO_2 components. A kinetic model for quartz and rutile growth from a fluid can account for many of the salient features observed in these experiments, as well as those from previous studies, and suggests that Ti concentrations in quartz are sensitive to the TiO_2/SiO_2 ratio of the fluid as opposed to the absolute concentration or activity of TiO_2

dissolved in the fluid. This chapter was published in Geochimica et Cosmochimica Acta as “Ti-in-quartz: Evaluating the role of kinetics in high temperature crystal growth experiments” in May of 2020 and was co-authored by: James M. Watkins, Mark H. Reed, John J. Donovan, and Donald J. DePaolo.

In Chapter III of this dissertation, I use electron microscope images and microanalytical results to understand how Ti concentrations and distributions in quartz from the Butte, Montana porphyry Cu-Mo deposit record formation and deformation events. The Butte deposit has been mined for over 150 years and so is a particularly well-studied porphyry Cu deposit. Butte is still being actively mined, and its mining history has earned it the status of America’s largest superfund site. Natural hydrothermal quartz shows complex distributions of Ti when imaged with scanning electron microscope (SEM)-CL. Quartz from barren quartz/quartz-molybdenite veins in the Butte porphyry Cu-Mo deposit exhibit two coexisting CL textures caused by Ti heterogeneities: CL-euhedral and CL-mottled. CL-euhedral texture consists of alternating dark and light growth zones within euhedral crystals and forms during crystal growth from a fluid phase. CL-mottled quartz is patchy in CL and forms during high temperature recrystallization driven by strain of the vein as local stresses imposed by a cupola dissipate and regional stresses become dominant. CL-euhedral crystals survive deformation because they are oriented in cockscomb quartz layers and strain is preferentially accommodated by the randomly oriented crystals filling vein centers. Detailed microprobe analyses show that the dark bands of CL-euhedral textures have the same Ti concentrations as the adjacent CL-mottled and we interpret those values as being the equilibrium concentration for the pressure and temperature of crystal growth and deformation. Bright bands in CL-euhedral crystals record excess Ti and are positive kinetic excursions from equilibrium. This chapter is being prepared for submission to American Mineralogist and is co-authored by Mark H. Reed and James M. Watkins.

In Chapter IV of this dissertation, I attempt to link empirical relationships between supersaturation and impurity incorporation to molecular scale processes that might be responsible for the formation of bright bands with higher-than-equilibrium Ti concentrations in CL-euhedral crystals under isobaric, isothermal, closed system conditions. Previous experiments, as well as those from Chapter 2, show that zoned

crystals form from aqueous solutions at constant temperature and pressure, but how or why remains an open question. Some of the vein quartz grains from the Butte porphyry Cu-Mo deposit also have euhedral oscillatory growth zones when imaged with a cathodoluminescent (CL) detector. CL-dark growth bands span a narrow range of Ti concentrations, from 8 - 40 ppm, and record equilibrium Ti. CL-bright bands span a large range of Ti concentrations, from 32 ppm Ti - 332 ppm Ti, that are inconsistent with equilibrium growth. One possibility for higher-than-equilibrium Ti incorporation in quartz is a process of step pinning and recovery near the 'dead zone' of crystal growth, a region of low supersaturation where a crystal does not grow despite being in contact with a supersaturated solution. In this scenario, impurities collect at the edges of growth features on a crystal surface and prevent new layers of growth from advancing. As elementary steps, which are the smallest possible growth layer that can form, are pinned by Ti they coalesce into macrosteps. Macrosteps are larger growth layers that advance even when smaller steps cannot, although they too can become pinned by Ti sorbing to their edges. With increasing supersaturation, eventually macrosteps can overtake the pinned edges and advance across the crystal surface, incorporating excess Ti into the layer they form. I hypothesize that this process may underlie the formation of CL-bright bands.

CHAPTER II
TI-IN-QUARTZ: EVALUATING THE ROLE OF KINETICS IN HIGH TEMPERATURE CRYSTAL GROWTH EXPERIMENTS

From Acosta M. D., Watkins J. M., Reed M. H., Donovan J. J. and DePaolo D. J. (2020) Ti-in-quartz: Evaluating the role of kinetics in high temperature crystal growth experiments. Geochim. Cosmochim. Acta 281, 149–167.

1. Introduction

The titanium-in-quartz geothermobarometer (TitaniQ) was developed by Wark and Watson (2006) and takes advantage of the broad occurrence of quartz in crustal rocks and its stability across a wide range of geological environments. Over the past decade, TitaniQ has been refined experimentally (Thomas et al., 2010; 2015) and applied by others to infer the conditions and rates of crystallization in volcanic and plutonic environments (Wark et al., 2007; Shane et al., 2008; Girard and Stix, 2012, Mercer and Reed, 2013; Ackerson et al., 2018; Chamberlain et al., 2014), metamorphic environments (Behr and Platt, 2011; Bergman and Piazolo, 2012; Ashley et al., 2013), and hydrothermal systems (Betsi and Lentz, 2010; Müller et al., 2010; Vasyukova et al., 2013; Tanner et al., 2013; Mercer and Reed, 2013).

A puzzling issue that has emerged from the widespread application of the Thomas et al. calibration of TitaniQ is that it yields temperature estimates that are systematically lower, by about 100-150°C, than those given by other thermobarometers applied to the same rocks (Figure 2.1a), especially in relatively low pressure environments (< 3-4 kbar) where temperature can also be estimated by other methods. TitaniQ is based on principles of equilibrium partitioning, as applied to the experiments upon which TitaniQ is based, which were carried out at temperatures of 700 to 940ºC and pressures of 5 to 20 kbar. Thomas et al. (2010) were thorough in their analysis of run products and established multiple lines of evidence for having achieved quartz-rutile equilibrium in their experiments, including: (1) reproducible and systematic temperature- and pressure-dependences of Ti concentration in quartz, (2) homogeneous distributions of Ti in quartz, (3) inclusions of rutile in quartz, indicating co-precipitation, and (4) checking the

results by doing thermal annealing experiments (Thomas et al., 2015). If the expressions of TitaniQ represent the equilibrium case, how do we interpret the systematic differences with other thermobarometers (Figure 2.1a) and other insights derived from decades of study? Two issues emerge: one is whether equilibrium was established in the experiments or in nature, and the other concerns the extrapolation of higher-pressure data to low pressures. A related point is that natural crystals typically grow at rates that are many orders of magnitude slower than those in laboratory experiments, thus the role of kinetic effects in the experiments should be evaluated.

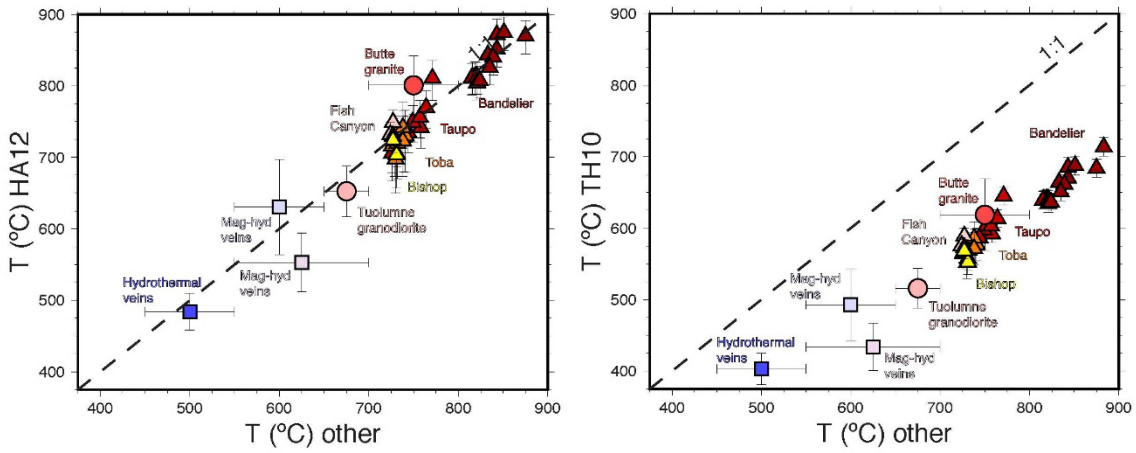

Figure 2.1 TitaniQ applied to natural samples for which temperature has been estimated by other methods (Appendix A). Triangles are volcanic samples with zircon saturation temperatures based on quartz-hosted melt inclusion compositions along the same growth zones as entrapped zircons in the quartz crystals (Kularatne and Audetat, 2014). Circles are plutonic samples. Squares are hydrothermal quartz veins with rutile inclusions and temperatures are based on quartz-hosted fluid inclusion thermometry, Zr-in-rutile thermometry in quartz veins as well as alteration envelopes around quartz veins, and thermodynamic modeling, as well as other methods (Mercer and Reed, 2013). (A) The TH10 calibration yields temperatures that are systematically lower than those estimated using other geothermometers. (B) The HA12 calibration is in better agreement with the other geothermometers.

Other researchers have grown quartz in the laboratory at pressures ranging from 1 to 10 kbar and reported lower Ti concentrations, by a factor of 2-3, than predicted by TitaniQ (Huang and Audetat, 2012; Nachlas and Hirth, 2015). In none of these latter experiments has quartz-rutile equilibrium been convincingly established, and yet, when

one applies to natural quartz the empirical expressions deduced from slow quartz growth experiments (Huang and Audetat, 2012), the temperature estimates agree with those from other thermobarometers, including those based on mineral and fluid inclusions in quartz (Figure 2.1b).

Our goal in this study is to investigate the low-pressure region with experiments at 800ºC and 1 kbar and using a range of different starting materials and experimental configurations. An important point is that different sources of SiO_2 and polymorphs of TiO_2 have been used as starting material in previous studies. Because anatase has a higher solubility than rutile, it yields a larger initial concentration of TiO_2 in the fluid phase than does rutile. As we show, anatase also has a surprisingly strong influence on the growth rate and morphology of the crystallizing SiO_2 component, suggesting a heretofore overlooked coupling between the SiO_2 and TiO_2 components. We use these new insights, combined with models of the evolution of the fluid phase composition during experiments, to evaluate the conflicting evidence from experiments and natural samples.

1.1 History of TitaniQ calibrations

Ostapenko et al. (1987, 2007) suggested that Ti in quartz could be used as a thermometer. Two decades later, the TitaniQ geothermometer was calibrated experimentally by Wark and Watson (2006) using a piston cylinder apparatus at P = 10 kbar, temperatures ranging from 600 to 1000ºC, and durations of 3 to 17 days (66 - 406 hours). At the time, Wark and Watson (2006) thought that the pressure dependency would be negligible but subsequent application of the 10 kbar calibration to natural samples yielded temperatures that were inconsistent with equilibrium mineral assemblages (e.g. Lowers et al., 2007; Ghiorso and Evans, 2008). Motivated by the possibility that such discrepancies could be due to a pressure-dependence, Thomas et al. (2010), hereafter referred to as 'TH10', ran similar experiments lasting 1-5 days at P = 5-20 kbar and T = 700-940ºC. Their results revealed that there is indeed a strong pressure dependence to TitaniQ (Figure 2.2a).

To extend TitaniQ to lower pressures, Huang and Audetat (2012) ran quartz growth experiments lasting 3-10 days at T = 600-850ºC and P = 1, 2, and 10 kbar. Their

results are significantly different from those of the previous work (Figure 2.2b). In the Huang and Audetat (2012) study, hereafter referred to as 'HA12', Ti concentrations are more variable, correlate positively with quartz growth rate, and are systematically lower than those of TH10. Because slower growth rates are generally indicative of a system closer to equilibrium, HA12 reasoned that the Ti concentrations from their slow-grown quartz crystals could be used as the basis of a new set of equilibrium calibration curves (Figure 2.2b), which as shown in Figure 2.1b, generally agree well where comparisons can be made with other temperature estimates. This implies that, the systematic nature of their results notwithstanding, the higher Ti-in-quartz from TH10 reflects far-from-equilibrium behavior.

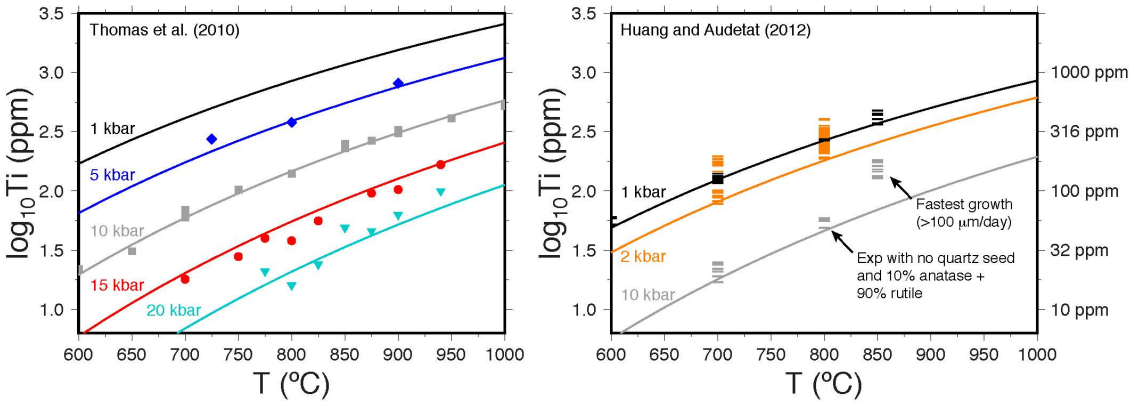

Figure 2.2 Ti concentrations in quartz from Thomas et al. (2010) are higher and more systematic than those from Huang and Audetat (2012). The TH10 experiments were done with anatase as a source of titanium whereas the HA12 experiments used rutile with the exception of one experiment that used a mixture of rutile and anatase. The HA12 curves are based on their most slowly-grown quartz, which corresponds to the lowest Ti values.

The results of HA12 and interpretation therein led Thomas et al. (2015), hereafter referred to as 'TH15', to conduct thermal annealing experiments where they used quartz starting material with higher-than-equilibrium Ti contents. The overgrowths on their quartz seeds had lower Ti, by an amount that was consistent with their previous results at 20 kbar. This, along with the generally more systematic *P* and *T* dependence of their calibration, allowed them to make a case for why their experiments reached equilibrium whereas those of HA12 did not. They concluded that HA12's low Ti concentrations were

solely a consequence of large gradients in titania activity ($a_{TiO_2}^{liq}$) persisting throughout the runs.

1.2 Equilibrium partitioning relationships

TitaniQ is intended to apply to equilibrium between coexisting quartz, rutile, and a silicate or aqueous liquid. For slowly growing quartz crystals in natural rocks, an approximation to equilibrium may be attainable, but for rapidly grown crystals in laboratory experiments, it is not guaranteed.

The amount of TiO_2 incorporated into quartz crystals *at equilibrium* with a liquid at rutile saturation is described by the relationship:

$$\mu TiO_2(qtz) = \mu TiO_2(liq) = \mu TiO_2(rt), \quad (1)$$

which states that the chemical potential of TiO_2 dissolved in quartz is equal to that of TiO_2 in rutile and the liquid. The quartz-rutile equality can be expanded to:

$$\mu^o_{TiO_2}(qtz) + RT \ln \gamma x_{TiO_2}(qtz) = \mu^o_{TiO_2}(rt) + RT \ln a_{TiO_2}(rt), \quad (2)$$

where μ^o is chemical potential at a defined standard state, R is the gas constant (8.314 J mol^{-1} K^{-1}), T is temperature in Kelvin, a is activity, x is mole fraction, and γ is the activity coefficient for TiO_2 dissolved in quartz as a solid solution constituent. This expression can be rearranged to the form:

$$\ln x_{TiO_2}(qtz) = \frac{\mu^o_{TiO_2}(rt) - \mu^o_{TiO_2}(qtz)}{RT} + \ln a_{TiO_2}(rt) - \ln \gamma_{TiO_2}(qtz), \quad (3)$$

which is essentially identical to equation 4 of TH10, except that they used the notation "k" instead of "γ" for the last term, where they referred to k as a Henry's Law constant. The first and last terms on the right-hand side of Equation (3) have an unknown P- and T-dependence that can only be determined by experiment. Equation (3) also states explicitly that if quartz and rutile coexist at equilibrium with a liquid, the mole fraction of TiO_2 in

quartz is not dependent on the activity of TiO_2 in the liquid phase. When the system departs from equilibrium, Equation (3) does not hold. For example, it is possible for quartz and rutile to grow simultaneously from a liquid phase where $\mu_{TiO_2}(liq)$ is higher than the equilibrium value in both phases. And in general, if both quartz and rutile are growing at relatively high rates, both $\mu_{TiO_2}(liq)$ and $\mu_{SiO_2}(liq)$ are likely larger than the equilibrium solubility values. How much larger is the main question for interpreting the experimental results, since crystal growth, especially at laboratory experimental rates, is an inherently non-equilibrium process. In natural settings, where quartz crystal growth rates can be several orders of magnitude slower than in the laboratory, equilibrium, or near-equilibrium, growth is a better approximation.

1.3 Requirements for maintaining equilibrium during quartz crystal growth

If quartz crystal growth in a laboratory experiment is not happening at near-equilibrium conditions, then the challenge is to estimate the SiO_2 and TiO_2 activities in the liquid phase during quartz and rutile growth. This is not necessarily an easy task, but a high degree of accuracy is not required. For example, the difference between the TH10 and HA12 TiO_2 concentrations in quartz at 10 kbar is about a factor of 3 (Figure 2.2). If that difference results from a difference in $a^{liq}_{TiO_2}$, the liquid must be oversaturated with respect to rutile by a factor of three in TH10, undersaturated by a factor of three in HA12, or some other combination that leads to a factor of three difference between the two.

If the liquid is at rutile saturation, then $a^{liq}_{TiO_2} = K_{sp,rut}$ and the degree of supersaturation is given by $\Omega_{rut} = \frac{a^{liq}_{TiO_2}}{K_{sp,rut}}$, where $\Omega_{rut} > 1$ if the liquid is saturated in anatase, since anatase has a significantly higher solubility than rutile. Effective buffering of $a^{liq}_{TiO_2}$ at $K_{sp,rut}$ requires that rutile nucleation, growth, and dissolution are fast relative to quartz growth, despite being near rutile saturation, and that diffusion of TiO_2 in the liquid phase can efficiently erase any transient concentration gradients arising from the growth or dissolution of rutile and quartz. The complication in the quartz growth experiments of both TH10 and HA12 is that as quartz grew there likely was a continually changing TiO_2/SiO_2 ratio, and SiO_2 oversaturation in the liquid (without which the quartz would

not grow). It is this issue we address below with models of what might be happening during the experiments.

2. Methods

There are a number of challenges facing low pressure experiments that have been identified previously. TH10 attempted experiments at 1 kbar in cold-seal pressure vessels (CSPVs) but were unsuccessful in growing quartz large enough to analyse by electron probe microanalysis (EPMA). When they used powdered quartz as starting material, the overgrowths were too small (< 2 μm) for a microprobe, and when they used silica glass as starting material, it led to the formation of a mixture of polycrystalline cristobalite and tridymite. Another challenge is that EPMA measurements are susceptible to contamination by secondary fluorescence of Ti from rutile crystals, even if they are tens of microns away from the primary interaction volume (Wark and Watson, 2006; Borisova et al., 2018). These issues were circumvented by HA12 by using large quartz seed crystals that could be physically separated from the surrounding rutile. However, the HA12 experiments produced a wide range of Ti concentrations and Thomas et al. (2015) suggested that this aspect of the experimental design is fundamentally flawed and accounts for differences between the HA12 and TH10 calibrations.

2.1 Experimental capsules

Our experimental approach is a hybrid of those in TH10 and HA12. In most of our experiments, a 5 mm long Pt capsule (0.127 mm wall thickness) containing only a Ti-free quartz seed crystal is placed within a 15 mm long gold capsule (0.2 or 0.4 mm wall thickness) loaded with silica glass beads, 10 μL of de-ionized water and a TiO_2 phase (Figure 2.3). The inner capsule mimics the conditions of the HA12 experiments, whereby a Ti-rich overgrowth forms on a large seed crystal. The outer capsule mimics the TH10 experiments, whereby quartz nucleates and grows in an environment where small TiO_2 particles are pervasive, which promotes buffering of $a^{\mathrm{liq}}_{\mathrm{TiO_2}}$. We also ran experiments without an inner capsule or quartz seed, but these produced mostly tridymite in runs lasting less than 10 days, confirming the behaviour documented by TH10 at low pressures. A select few of the newly formed quartz and tridymite crystals from double

capsule and single capsule experiments were painstakingly separated from nearby TiO_2 and analysed using a novel combination of the plasma focused ion beam (PFIB) and EPMA (Appendix A).

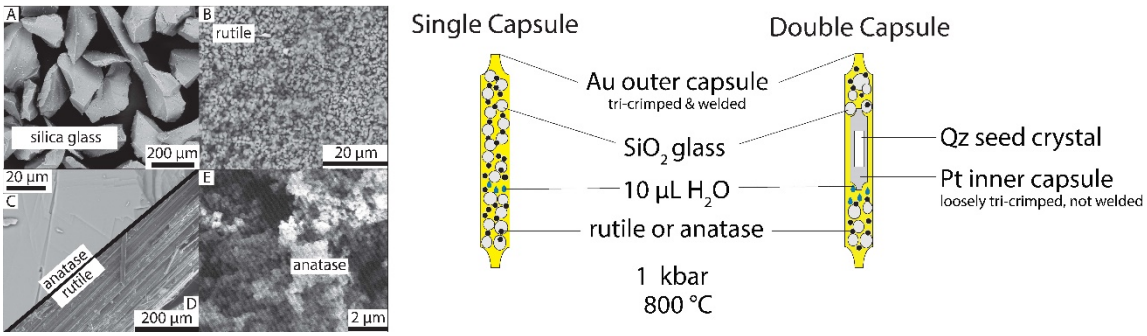

Figure 2.3 Experimental design. Left: SEM images of starting materials: (A) sieved silica glass, (B) powdered rutile, (C) a single natural crystal of anatase showing a cleavage trace, (D) a single natural rutile crystal, and (E) powdered anatase. Note the particle size difference between the powdered rutile and powdered anatase. Right: Double-capsule and single-capsule designs used in this study.

We initially planned to run experiments across a range of temperatures and pressures, but the variable results at 800°C and 1 kbar warranted continued investigation under these conditions using different SiO_2 and TiO_2 starting materials (Table 2.1). In the end, the most important variables proved to be (a) whether quartz grew on a pre-existing seed or nucleated and grew through a series of metastable precursors and (b) whether the TiO_2 starting material was powdered rutile (99.9% purity; Alfa Aesar) or powdered anatase (99% purity; Sigma-Aldrich).

2.2 Experimental runs

Experiments were run in computer-controlled, rapid-quench cold-seal pressure vessels (CSPVs) at the University of Oregon. The capsules were placed in an Inconel rod, which was then inserted into a René 41 pressure vessel. The pressure vessel was connected to a stepper motor-controlled pressure line with H_2O as the pressure medium. Pressure was measured using a digital Omega pressure transducer with a precision of ± 1 bar. Temperature was measured using a type K (chromel-alumel) thermocouple and was controlled to ±2°C.

Table 2.1 Overview of experiments including capsule design and source materials used. Dashes and blank entries indicate no data.

Capsule Design	TiO2 source	Experiment	SiO2 sieve size (microns)	Duration (hours)	Min Ti (ppm)	Max Ti (ppm)	n	Outer Quartz Ti Range (ppm)
Double Capsule Experiments	synthetic rutile	2	> 149	216	310	347	5	-
	synthetic rutile	3	> 149	214	288	315	5	-
	synthetic rutile	4	> 149	241	443	546	20	-
	synthetic rutile	7B	175 - 104	189	288	513	17	-
	synthetic rutile	8	249 - 175	260	357	482	11	-
	synthetic rutile	9B	104 - 60	306	235	356	3	-
	synthetic rutile	9C	104 - 60	247	216	570	17	-
	synthetic rutile	15	175 - 104	314	275	443	19	-
	synthetic rutile	18	175 - 104	288	272	454	10	-
	synthetic anatase	19_ana	60 - 43	526	-	-	-	-
	synthetic rutile	20	60 - 48	140	199	582	19	-
	synthetic rutile	21	60 - 43	139	278	464	29	-
	natural rutile	24b	60 - 43	161	28	62	101	14 - 487 (n=28)
	natural anatase	27_ana	175 - 104	236	105	116	7	36 - 350 (n=12)
	synthetic anatase	29_ana	175 - 104	169	126	248	23	177 - 890 (n=18)
	synthetic anatase	31_ana	175 - 104	24	111	505	14	552 - 870 (n=12)
	synthetic anatase	32_ana	175 - 104	6	275	419	8	-
	synthetic rutile	33	175 - 104	24	211	215	2	-
	synthetic rutile	34	175 - 104	6	416	673	9	-
	synthetic anatase	Qzero_ana	175 - 104	-	-	-	-	-
	synthetic rutile	Qzero	175 - 104	-	-	-	-	-
Single Capsule Experiments	synthetic anatase	35_ana	175 - 104	400	608	952	9	-
	synthetic rutile	36	175 - 104	170	437	582	2	-
	synthetic anatase	37_ana	175 - 104	120	-	-	-	-
	synthetic rutile	39	175 - 104	96	-	-	-	-

To start a run, the pressure was brought up to 1 kbar and the pre-heated oven was lowered over the pressure vessel. The stepper motor controlled the pressure during heating. The desired temperature was reached after ~ 36 minutes. At this point we closed a valve to isolate the pressure vessel and turned off the stepper motor. This was done to mitigate pressure leaks along the pressure line but led to thermally induced pressure variations of about ±10 bars throughout the run. To end the run, the sample was quenched slowly by raising the oven and allowing ambient air to cool the vessel. It took about 15 minutes for the pressure to drop to 1 bar and about 2 hours for the sample to cool to 25°C.

After an experiment, crystals were extracted from the capsules, imaged with a scanning electron microscope (SEM), mounted in epoxy, and polished to 0.25 microns using diamond grit. The polished surfaces were re-imaged prior to being analyzed on the microprobe.

2.3 SEM imaging

For most experiments, we collected SEM secondary electron (SE) and backscattered electron (BSE) images of quartz overgrowths from the inner capsule as well as the newly formed quartz crystals in the outer capsule. All crystals were imaged and analyzed at the Center for Advanced Materials Characterization in Oregon (CAMCOR) at the University of Oregon on an FEI Quanta 200 FEG Environmental SEM at 15 keV with a beam current of 400 nA.

The BSE and SE data were collected using the SEM in low-vacuum mode with variable water pressure (water pressure was increased if charging of the sample prevented adequate image collection). BSE imaging often produced a higher quality image than did SE, as it is less susceptible to charging. Once mounted and carbon-coated, SEM-cathodoluminescent (CL) images were collected under the same operating conditions but under high vacuum. Gain and offset vary from image-to-image and were optimized accordingly.

2.4 Raman spectroscopy

Phase identification was made with a Horiba Jobin-Yvon Labram 800 Raman spectrometer with a 5313-nm laser excitation and beam size of ~1 μm at Oregon State University. Spectra were analysed with the LapSpec 6.0 software suite. Each measurement was taken in the wavenumber range 50-850 cm^{-1} using a 200 μm confocal hole diameter and 1200 lines-per-mm diffraction grating. After backgrounds were subtracted, peaks were fit with Gaussian functions identifying peak positions and attributes. The fitted spectra were compared to reference spectra from the RRUFF database.

2.5 PFIB sample prep of outer capsule materials

To escape the secondary fluorescence of proximal rutile in EPMA Ti analyses, quartz crystals were separated from rutile using a plasma focused ion beam (PFIB) at the University of Oregon (Appendix A). A Helios G4 PFIB UXe DualBeam SEM with a beam current of 0.5 μA was used to mill 70 μm deep moats around polished SiO_2 crystals. For some samples in which polishing would make it difficult to isolate crystals of certain morphology, the unmounted experimental run products were adhered to a carbon tab for PFIB extraction. After the crystal(s) of interest were identified, they were welded to the micromanipulator with carbon, removed from the sample, attached to a TEM holder and ion polished to a smooth, flat surface. We were then able to analyse these crystals by EPMA. Since this technique is time-consuming, only a few experiment run products were analysed in this manner.

2.6 Microprobe measurements

After SEM-BSE/SE/CL images were collected, Ti concentrations in quartz overgrowths were measured by electron probe microanalysis (EPMA) on a Cameca SX100 electron microprobe equipped with five tunable wavelength dispersive spectrometers. Operating conditions were 40 degrees takeoff angle, and a beam energy of 20 keV. The beam current was 100 nA and the beam diameter was 10 microns. The data were reduced using ProbeForEPMA software.

The counting time was 425 seconds on-peak. Ti Kα was calibrated using a synthetic TiO_2 standard. When necessary, intensity data were corrected for Time Dependent Intensity (TDI) loss (or gain) using a self-calibrated correction for Ti Kα. Ti Kα was measured on all five spectrometers and combined for quantitative analysis using the aggregate intensity method and correction for continuum artifacts using the quantitative blank correction (Donovan et al., 2011). The MAN background intensity data were measured on synthetic SiO_2, MgO, NiO, and MnO standards and the Ti Ka background was corrected for continuum absorption (see Donovan et al., 2016). Unknown and standard intensities were corrected for dead time and standard intensities were corrected for beam and standard drift over time. The matrix correction method was the Armstrong-Brown ρ(φz) method.

To avoid secondary fluorescence, areas selected for spot analysis were imaged with BSE when digitizing on the microprobe. A small number of spots (n =15 out of 437) were identified as being contaminated by secondary fluorescence from a TiO_2 crystal beneath the surface and were therefore excluded from the final data set. The excluded data have Ti concentrations ranging from ~15000 to 35000 ppm. We also quantified the potential magnitude of secondary fluorescence contamination with Monte Carlo simulations of the geometries of our experimental run-products (Appendix A).

3. Results

3.1 Titanium in quartz at 800°C and 1 kbar

We observe variations in crystal form, TiO_2 abundance, and Ti zonation within quartz that depend on the type of TiO_2 source material and whether the quartz grows on the seed crystal (hereafter referred to as "inner quartz") or nucleates and grows in the outer capsule (hereafter referred to as "outer quartz"). When powdered rutile is used, the inner quartz Ti varies from ~200 to 600 ppm, with many values clustering at or above the 267 ppm Ti calculated from HA12 (Figure 2. 4 – black symbols). When powdered anatase is used, the inner quartz has a similar range of ~150-550 ppm Ti whereas the outer quartz has higher and more variable Ti (~450-850 ppm; Figure 2.4 – blue symbols). When a large single crystal of rutile or anatase is used, the inner quartz has low Ti (~50-150 ppm) whereas the outer quartz has higher and more variable Ti (~50 to 500 ppm;

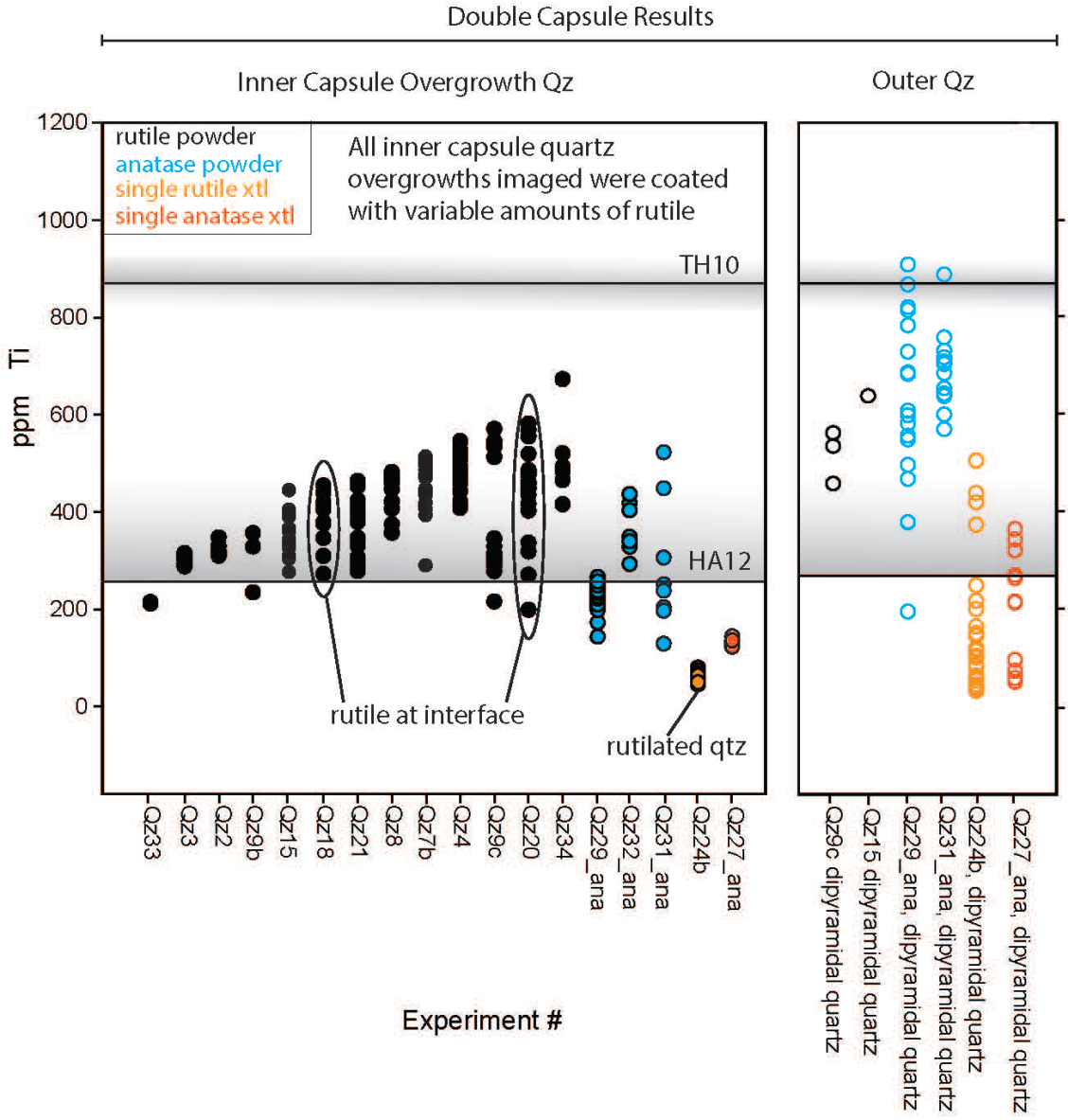

Figure 2.4 Ti concentrations in quartz from each experiment, arranged in ascending order. Quartz overgrowths on the seed crystal are variable and below the value predicted by TH10. Dipyramidal quartz that nucleated and grew in the outer capsules also has variable but generally higher Ti values than inner capsule quartz. The single-capsule experiments produced mostly tridymite with sparse dipyramidal quartz.

Figure 2.4 – orange and vermillion symbols). For single capsule experiments with no quartz seed crystal, the Ti concentrations in tridymite are higher in the anatase experiment than in the rutile experiment (Table 2.1).

3.2 Time series experiments (double capsule)

A series of short-duration experiments highlights the remarkably strong influence that powdered anatase versus powdered rutile has on the dissolution of SiO_2 glass as well as growth rates and shapes of SiO_2 polymorphs (Figure 2.5). In the zero-time rutile experiment, the run products are indistinguishable from the starting material. By contrast, the zero-time anatase experiment produced a mixture of cristobalite and source silica glass alongside anatase powder that has a larger grain size than the starting material. In both sets, outer silica appears to progress through the following Ostwald ripening sequence of metastable phases: glass-cristobalite-tridymite-quartz.

An important clue for interpreting the Ti results is that quartz and rutile crystallization in the outer capsule are considerably faster when anatase is used, suggesting high initial degrees of supersaturation in both components. A high initial degree of supersaturation with respect to rutile is supported by the direct precipitation and preservation of anatase in the 6-hour experiment, as revealed by Raman spectroscopy (Appendix A). In the 24-hour anatase experiment, the habits of outer quartz dipyramids are indistinguishable from those in the multi-day runs, suggesting that the reaction goes to near-completion sometime between 6 and 24 hours. By contrast, the 24-hour rutile experiment still contains incompletely dissolved silica glass and hexagonal platelets of tridymite in the outer capsule.

3.3 Multi-day powdered rutile experiments (double capsule)

Multi-day double capsule experiments using powdered rutile produced variable overgrowth thicknesses and Ti concentrations in quartz that overlap but extend the range produced in the HA12 experiments. Despite the variability, there are several generalizations that can be made. First, the inner quartz overgrowths always have abundant open cavities (incipient fluid inclusions) that run parallel to the c-axis of the overgrowth and are more filled-in near the intersections of crystal faces (Figure 2.6a).

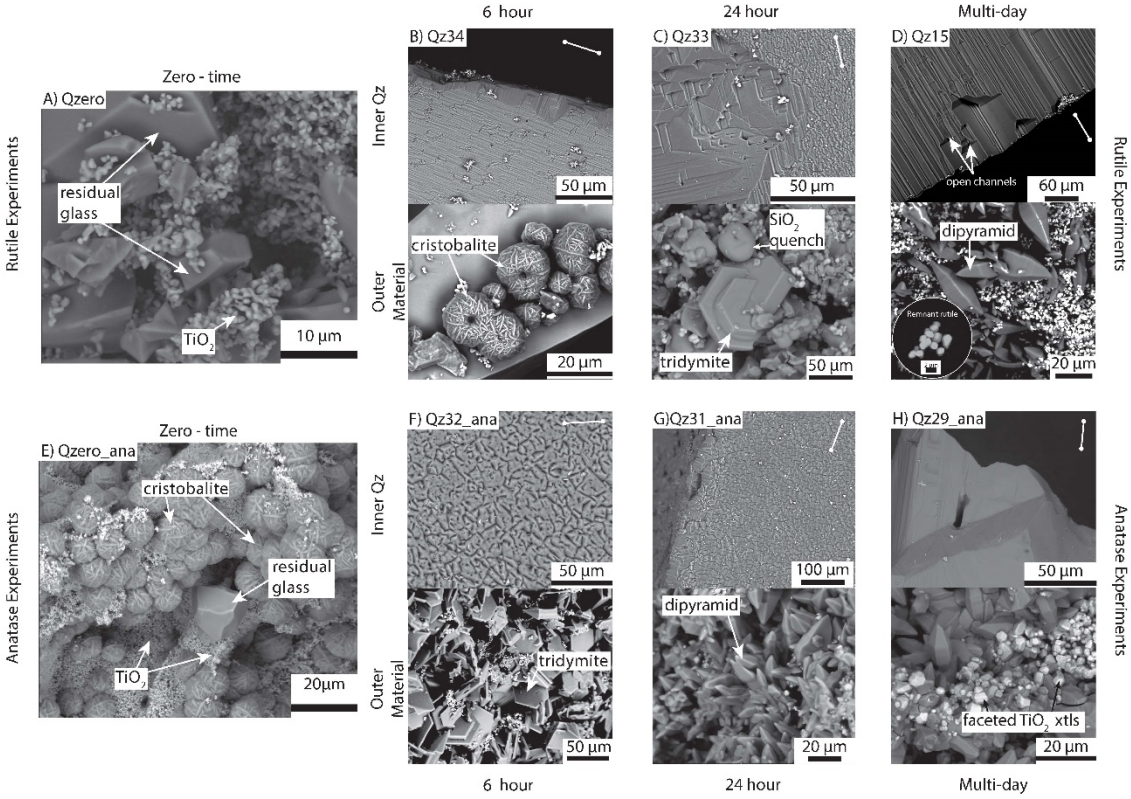

Figure 2.5 Results from time series experiments performed with rutile powder (top) and anatase powder (bottom). Barbells in this and subsequent figures indicate the direction of the c-axis. (A) In a rutile experiment with no dwell, the end products are indistinguishable from the starting materials. (B-D) The inner quartz overgrowth has open channels parallel to the c-axis whereas the outer material crystallizes through the sequence cristobalite-tridymite-quartz. (E) In an anatase experiment with no dwell, cristobalite has already formed. (F-H) The inner quartz overgrowth has a rugose texture that evolves into a smooth surface lacking the c-axis channels. The outer SiO_2 material crystallizes through the sequence cristobalite-tridymite-quartz but does so more rapidly than in the rutile experiments. The outer TiO_2 material is a mixture of anatase and rutile in the 6-hour run that evolves into relatively large euhedral rutile crystals in the multi-day runs.

Second, all the overgrowths are coated with small (~2 μm) spherical to subrounded TiO_2 particles (Figure 2.6a). When we observe TiO_2 encased within overgrowths after cutting and polishing, the TiO_2 is generally sparse, and occurs near the seed-overgrowth interface, akin to the experiments of HA12 (Figure 2.6b). Third, nearly all the quartz overgrowths exhibit complex Ti zonations, as seen in SEM-CL images (e.g., Figure 2.6c) and corroborated by EPMA analyses.

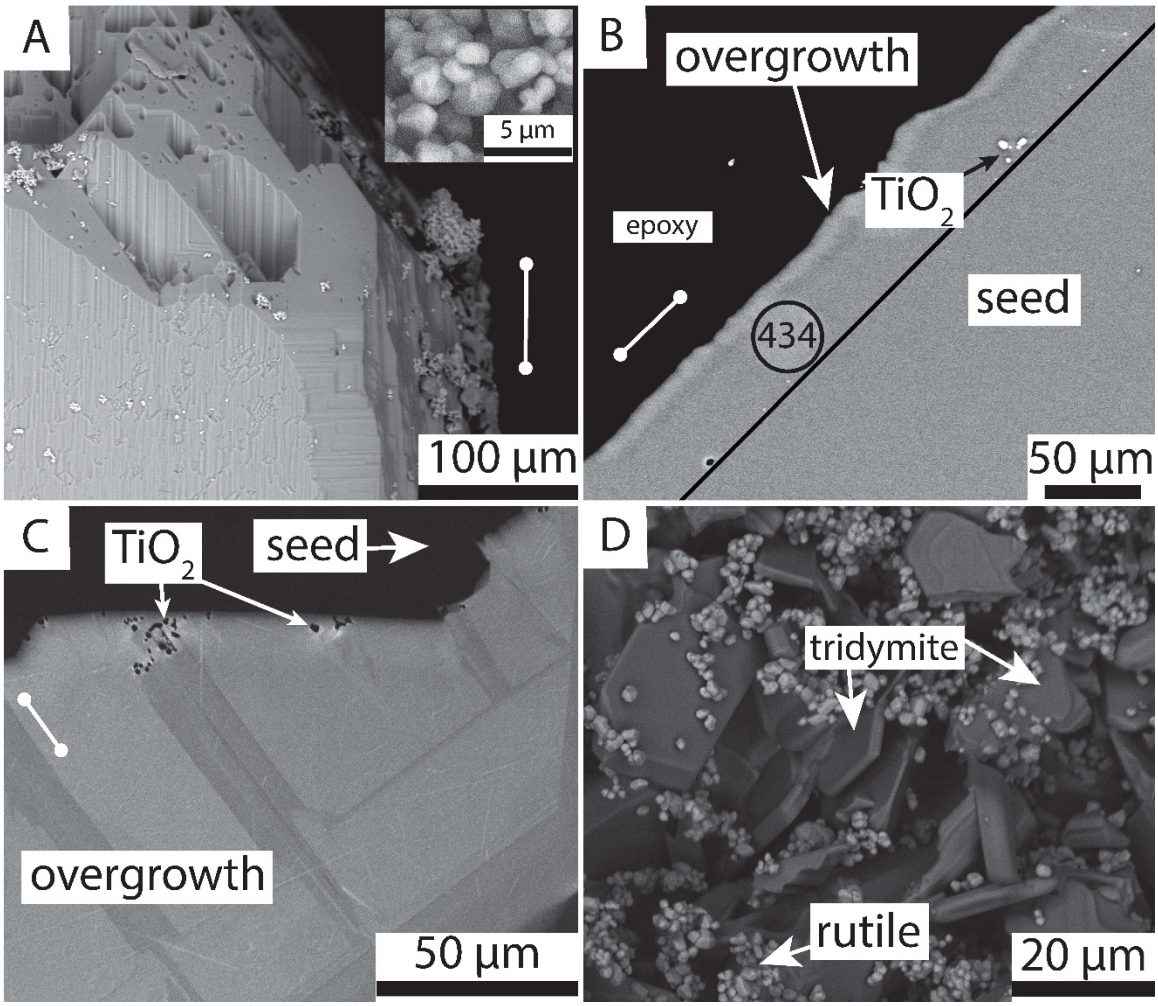

Figure 2.6 Results from multi-day double-capsule runs using powdered rutile. (A) SE image of Qz21 showing the c-axis channels and rutile coating the outer surface of the overgrowth. (B) BSE image of Qz20 showing the polished overgrowth with rutile inclusions near the seed-overgrowth interface. The circle shows where a value of 434 ppm Ti was measured. (C) SEM-CL image of the polished Qz18 overgrowth showing rutile inclusions near the seed-overgrowth interface and complex zonation. (D) BSE image of Qz20, which is representative of outer capsule material in many of the multi-day runs. Exceptions are Qz15 and Qz9c, which yielded dipyramidal quartz as opposed to tridymite.

In the outer capsules, newly formed SiO_2 crystals are small (10-20 μm) and exhibit two morphologies: euhedral quartz dipyramids and subhedral hexagonal platelets identified by Raman spectroscopy as metastable tridymite (Figure 2.6d). The relative abundance of the two polymorphs differs from experiment-to-experiment. In two of the experiments (9c and 15), the quartz dipyramids predominated, and a few of these crystals were extracted using the PFIB and then analysed by EPMA, yielding Ti-in-quartz values of ~450-650 ppm (Figure 2.4).

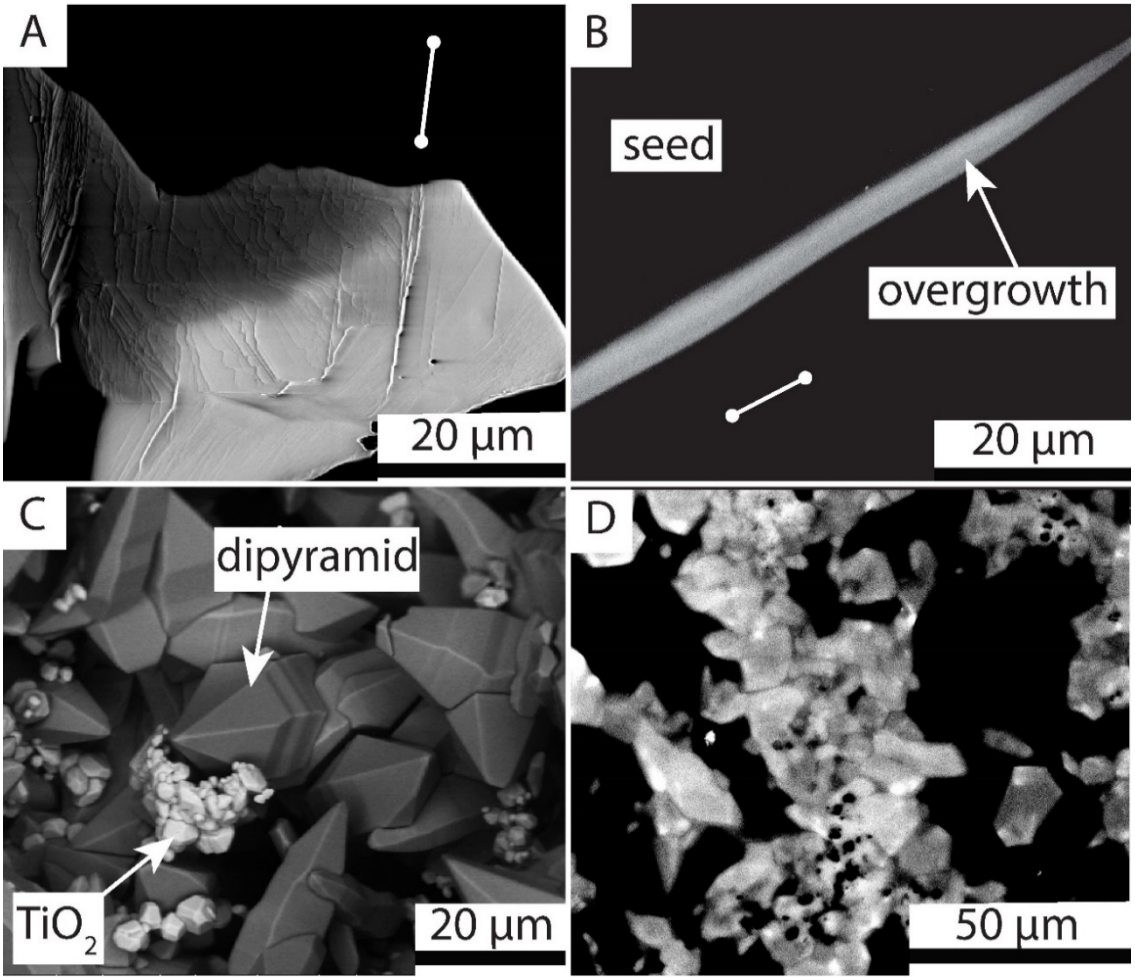

Figure 2.7 Results from a multi-day double-capsule run using powdered anatase (Qz29_ana). (A) SEM image of the overgrowth showing growth terraces. The shadow is cast by a portion of the overgrowth not in the field of view (sample was tilted with respect to the electron beam). (B) SEM-CL image showing the smooth and continuous nature of the overgrowth in cross section. (C) BSE image showing outer quartz dipyramids co-existing with faceted TiO_2 crystals. (D) SEM-CL image of outer quartz. The boundaries of the crystals are "fuzzy" because of signal loss at the edges of the microcrystals. Dark equant spots scattered in the quartz cluster are TiO_2 crystals.

3.4 Multi-day powdered anatase experiments (double capsule)

The experiments using powdered anatase produced markedly different run products. The inner quartz lacks open cavities and instead exhibits step edges, terraces, and spiral growth features (Figure 2.7a). In our first experiment using a 50:50 mixture of SiO_2 glass and anatase, the overgrowth was so riddled with equant, relatively large (2-7 μm) TiO_2 crystals that we could not analyze it with EPMA. TEM-SAED analysis confirmed that the TiO_2 crystals were rutile but also revealed that the quartz lattice in the immediate vicinity of the TiO_2 inclusion was strained (Appendix A). Subsequent experiments were carried out using a 75:25 mixture of SiO_2 glass and anatase, which led to smooth overgrowths that lack TiO_2 inclusions and are relatively uniform in CL (Figure 2.7b).

In the outer capsule, the newly precipitated quartz formed euhedral quartz dipyramids interspersed with euhedral TiO_2 crystals and some elongate rutile prisms (Figure 2.7c). The outer quartz crystals show some variability in CL brightness (Figure 2.7d) and have generally higher Ti concentration (~600-900 ppm) than the inner quartz from the same experiment (~150-500 ppm).

3.5 Large crystal experiments (double capsule)

The double capsule experiments in which we placed a single crystal of rutile or anatase in the outer capsule produced similar inner and outer quartz textures to those in the powdered rutile experiments, but a lower abundance of rutile precipitated during the run. Inner quartz exhibits open cavities (Figure 2.8a) and zonations of Ti concentration (Figure 2.8b). In the rutile crystal experiment, we found elongate TiO_2 micro-needles extending outward from the quartz overgrowth, forming a rutilated quartz overgrowth (Figure 2.8c) with only 50 ppm Ti in a non-rutilated zone about 200 μm away.

The newly formed quartz in the outer capsule coated the large rutile or anatase crystal, the surface of which had barely dissolved during the run. In the anatase experiment, the surface of the crystal as viewed by SEM was highly altered from the initially flat anatase cleavage surfaces to a hummocky, irregular surface, a change presumably caused by the polymorphic transformation of anatase to rutile.

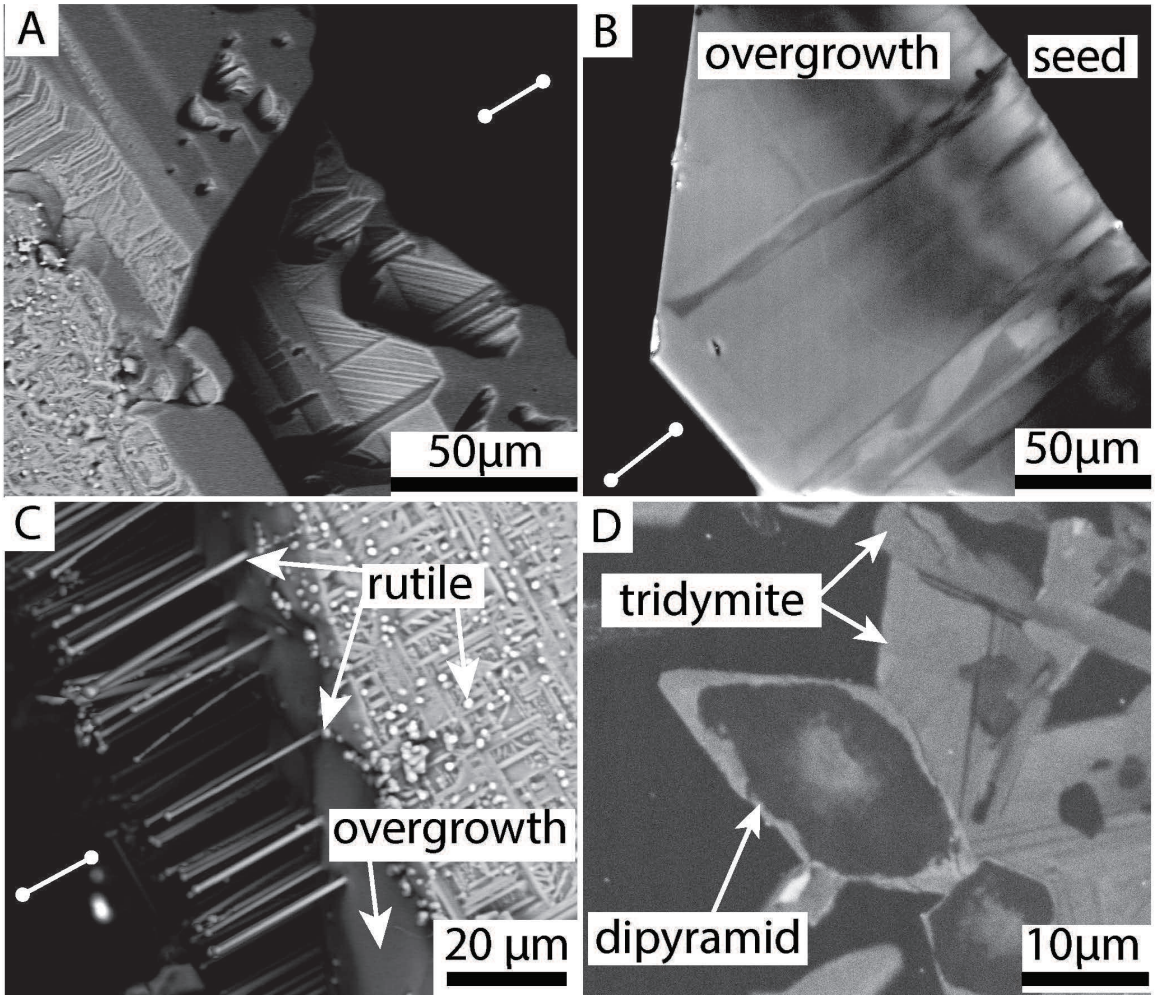

Figure 2.8 A double-capsule multi-day experiment (Qz24b), where a large crystal of natural rutile was used as the source of TiO_2 yielded a rutilated overgrowth that had only 50 ppm Ti. (A) The quartz overgrowth exhibits striations and open cavities. (B) SEM-CL image showing wavy-oscillatory zonations on part of the overgrowth. (C) BSE image showing a portion of the overgrowth that was rutilated. (D) SEM-CL image showing zoned dipyramidal outer quartz coexisting with homogeneous hexagonal tridymite crystals.

The lower abundance of rutile interspersed among the quartz crystals enabled us to measure Ti-in-quartz for both the inner and the outer crystals. In the outer capsule, the tridymite crystals are fairly homogeneous in CL and have Ti between 237-430 ppm with an average of ~320 ppm Ti. The quartz dipyramids are more complex in CL (Figure 2.8d), having a diffuse CL-bright core surrounded by a CL-dark mantle (~30-150 ppm Ti) that is truncated by a sharp, irregular boundary with a CL-bright rim (~410-430 ppm Ti).

3.6 Multi-day powdered rutile and powdered anatase experiments (single capsule)

Four experiments were carried out without an inner capsule or quartz seed crystal. The single capsule rutile experiments produced hexagonal platelets of tridymite with 437-582 ppm Ti (n = 2) (Figure 2.9a and 2.9b). There were also sparse dipyramidal quartz crystals about 5-10 µm in diameter that we were unable to relocate for PFIB extraction. The newly precipitated TiO_2 particles are subhedral and exhibit a unimodal size distribution (Figs. 2.9b and 2.9c).

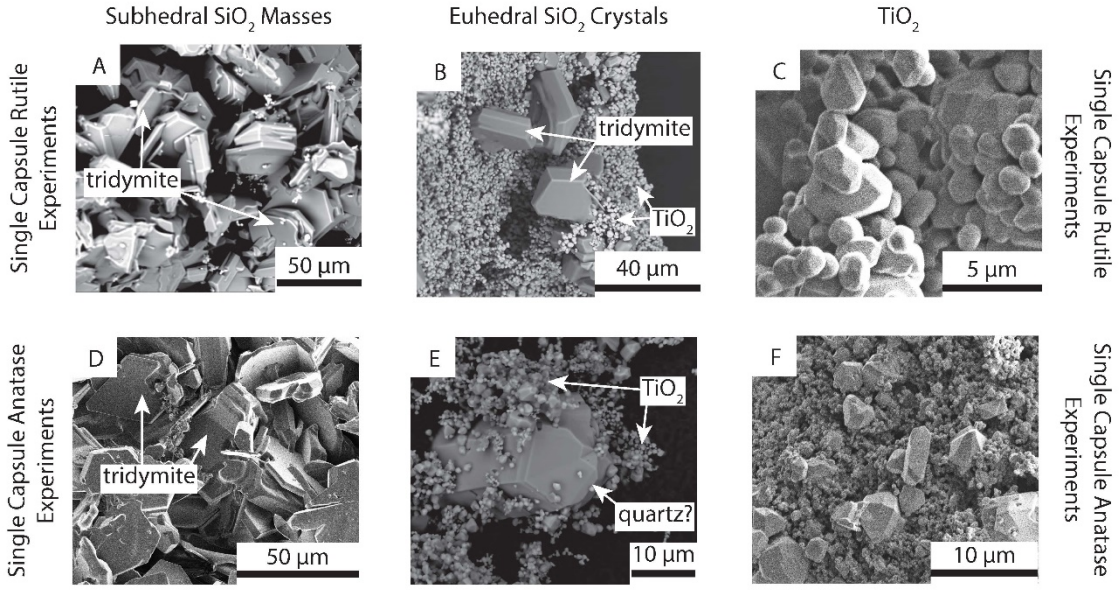

Figure 2.9 SEM-BSE and SE images showing results from multi-day single-capsule experiments. Experiments done with rutile yielded both (A) polycrystalline, intergrown masses of euhedral-to-subhedral tridymite and (B) isolated, euhedral crystals of tridymite in pockets of rutile. (C) Rutile from the single-capsule experiments developed facets with rounded edges. The single-capsule anatase experiments formed (D) polycrystalline masses of tridymite and (E) isolated euhedral crystals surrounded by TiO_2. (F) In these experiments, there was a striking bimodal size distribution of TiO_2.

The single capsule anatase experiments produced tridymite as both hexagonal columns and 10-20 μm wedges (Figs. 2.9d and 2.9e). The Ti-in-tridymite values range from 608-952 ppm (n = 9). The newly precipitated TiO_2 particles exhibit a bimodal size distribution, with large, euhedral crystals (10-20 μm) alongside smaller (0.85-1.5 μm), anhedral to subrounded TiO_2 particles (Figure 2.9f).

4. Simplified kinetic model for the TiO_2-SiO_2-H_2O system

The wide range of textures, Ti concentrations, and CL zonations in quartz overgrowths produced in our single-capsule and double-capsule experiments is a clear manifestation of kinetic effects. Consequently, we need to evaluate the reaction kinetics of the TiO_2-SiO_2-H_2O system with consideration for how different starting materials could lead to different initial conditions and various Ti concentrations in quartz. In this section, we develop a kinetic model for a starting fluid that is quartz supersaturated and is under- or supersaturated with rutile, and that can evolve in composition during the experiment, to estimate whether these effects could account for the observations of our experiments, and what parameter values are implied. The model is an attempt to represent the dynamic nature of the experiments as opposed to assuming or asserting that equilibrium is attained in a subset of them. A key postulate is that the TiO_2/SiO_2 ratio of precipitated quartz depends on the TiO_2/SiO_2 ratio of the fluid, as opposed to simply the TiO_2 concentration (or $a^{liq}_{TiO_2}$). This is to be expected where a trace ion substitutes for a lattice ion (e.g., Mg/Ca or Sr/Ca in calcite; Tesoriero and Pankow, 1996; Gabitov et al, 2006; Nielsen et al., 2013), and there is strong evidence that Ti^{4+} substitutes for Si^{4+} in the tetrahedral site in quartz (Thomas et al., 2010).

4.1 Governing equations

As quartz grows it excludes TiO_2 relative to SiO_2, so the TiO_2/SiO_2 ratio of the solution tends to increase even as quartz growth draws down the TiO_2 concentration. If quartz and rutile grow simultaneously, the fluid TiO_2/SiO_2 will differ from the value at quartz and rutile saturation, and the amount of the difference depends on the quartz and rutile precipitation rates. The faster quartz grows, and the slower rutile grows, the higher the TiO_2/SiO_2 ratio in the fluid becomes.

By taking the derivative of the fluid TiO_2/SiO_2 quotient, the rate of change of the fluid $(TiO_2/SiO_2)_f$ (= r_f) is written as:

$$\frac{dr_f}{dt} = \frac{1}{[SiO_2]}\frac{d[TiO_2]}{dt} - r_f\frac{1}{[SiO_2]}\frac{d[SiO_2]}{dt} \quad (4).$$

The rates of change of the individual concentrations are:

$$\frac{d[SiO_2]}{dt} = \frac{-R_{qtz}}{M_f} \quad (5)$$

and

$$\frac{d[TiO_2]}{dt} = \frac{-(R_{rutile}+r_f K_d R_{qtz})}{M_f}, \quad (6)$$

where R_i is precipitation rate in units of moles/s, M_f is the mass of the fluid in kg, $[TiO_2]$ and $[SiO_2]$ are concentrations in moles/kg. The partition coefficient, K_d = $(Ti/Si)_{quartz}/(Ti/Si)_{fluid}$, describes the TiO_2/SiO_2 partitioning between quartz and fluid (cf. McIntyre, 1963). Equation (6) shows that both rutile and quartz growth act to lower $[TiO_2]$. Substituting (5) and (6) into (4) yields, after some rearrangements:

$$\frac{dr_f}{dt} = \left(r_f - r_f K_d - \frac{R_{rutile}}{R_{qtz}}\right)\frac{R_{qtz}}{M_f[SiO_2]} \cong \left(r_f - \frac{R_{rutile}}{R_{qtz}}\right)\frac{R_{qtz}}{M_f[SiO_2]}. \quad (7)$$

This equation shows that what happens to r_f during the experiment depends on where it starts and the relative rates of rutile and quartz precipitation during the run. Quartz should precipitate with $r_{qtz} = K_d(TiO_2/SiO_2)_f$; that is, in proportion to the fluid phase r_f whether K_d is an equilibrium or a kinetically controlled value. If r_f starts out close to the ratio of precipitation rates, then it should remain close to constant during a run. If r_f substantially exceeds that ratio, then it will increase monotonically at a rate that depends on the removal rate of SiO_2 from the fluid (the last term in Eq. (7) has units of s^{-1} and is thus a timescale). However, if rutile is precipitating sufficiently fast, then r_f can decrease.

In the absence of diffusive transport limitations, the net precipitation rate of quartz and rutile can be written in the form (cf. DePaolo, 2011):

$$R_{\mathrm{qtz}} = k_{\mathrm{f,qtz}} A_{\mathrm{qtz}} K^{*}_{\mathrm{sp,qtz}} \left(\Omega_{\mathrm{qtz}} - 1\right) = k'_{\mathrm{f,qtz}} K^{*}_{\mathrm{sp,qtz}} \left(\Omega_{\mathrm{qtz}} - 1\right) \quad (8)$$

and

$$R_{\mathrm{rutile}} = k_{\mathrm{f,rut}} A_{\mathrm{rut}} K^{*}_{\mathrm{sp,rut}} (\Omega_{\mathrm{rut}} - 1) = k'_{\mathrm{f,rut}} K^{*}_{\mathrm{sp,rut}} (\Omega_{\mathrm{rut}} - 1), \quad (9)$$

where k_{f} is the forward rate constant for precipitation, A is the total mineral reactive surface area, K^{*}_{sp} is the stoichiometric solubility product (i.e., it is based on concentration and not activity), and Ω is the degree of supersaturation. It has been found experimentally that precipitation rates for other minerals such as calcite are not proportional to (Ω -1), but rather, vary with this quantity raised to a power n. In the absence of experimental data for quartz, rutile, and anatase, we take the simplest approach and adopt Eq. (8) and (9) for our calculations but note that other rate laws may prove more appropriate in the future. Additionally, we treat k'_{f} as constant with time even though the reactive surface area is variable and k_{f} can also vary with Ω (e.g., De Yoreo et al., 2009).

The four input parameters required to calculate r_{f} as a function of time are $\Omega_{\mathrm{qtz,initial}}$, $\Omega_{\mathrm{rut,initial}}$, $k'_{\mathrm{f,qtz}}$, $k'_{\mathrm{f,rut}}$, and M_{f}. Since we don't know the absolute values of the rate constants, we fix $k'_{\mathrm{f,qtz}}$= 1.0 and vary $k'_{\mathrm{f,rut}}$ for the purpose of illustration. The value of M_{f} determines how long it takes for the system to relax back to equilibrium from the initially oversaturated state, but since we fix $k'_{\mathrm{f,qtz}}$ at an arbitrary value of unity, it is sensible to remove M_{f} as a free parameter by normalizing the time by the total time. Finally, to convert r_{f} into a Ti in quartz value, it is necessary to specify a partition coefficient.

4.2 Estimating the partition coefficient

Previous studies on the solubility of Ti in quartz have not expressed the results in terms of partition coefficients, perhaps because it is difficult to estimate the amount of dissolved SiO_2 and TiO_2 in the liquid phase when the degree of supersaturation is unknown. A useful starting point is to estimate what the SiO_2 and TiO_2 concentrations would be if quartz and rutile were exactly at saturation and then speculate how much the

TiO_2/SiO_2 ratio of the fluid might change if the liquid were to have been highly supersaturated with respect to either or both of these phases.

The solubility of quartz in a hydrothermal solution at 800°C and 1 kbar is m_{SiO2} = 0.048 moles/kg-H_2O solvent as computed using SUPCRT92 (Johnson et al., 1992). This value is in good agreement with the value calculated using the expressions in Mysen (2019) for a TiO_2-SiO_2-H_2O fluid, which yields m_{SiO2} = 0.046 moles/kg-soln.

The solubility of rutile is sensitive to fluid composition. While there is general agreement that rutile solubility increases with dissolved salt concentration, there is some disagreement concerning the effect of dissolved SiO_2. Antignano and Manning (2008) found no measurable increase or decrease on rutile solubility with increasing SiO_2 in two experiments at 800°C and 10 kbar, whereas Mysen (2019) found a substantial (up to 3X) increase in rutile solubility in going from a TiO_2-H_2O fluid to a quartz-saturated TiO_2-SiO_2-H_2O fluid. At 800°C and 1 kbar, the expressions of Mysen (2019) yield m_{TiO2} = 0.00113 moles/kg-soln, or about 54 ppm Ti.

If quartz and rutile both precipitate exactly at saturation, the TiO_2/SiO_2 ratio of the fluid should be about 0.00113/0.048 = 0.024. For the solid TiO_2/SiO_2 ratio, a Ti in quartz of 850 ppm by mass (TH10) translates to molar TiO_2/SiO_2 = 0.00109, which is more than an order of magnitude lower than that in the liquid, meaning that quartz crystals are depleted in Ti with respect to the liquid (K_d ~ 0.045). A Ti concentration in quartz of 267 ppm (HA12) translates to an even lower K_d ~ 0.014. In what follows, we use K_d = 0.014 and assume K_d does not vary with the degree of supersaturation, i.e., there are no surface reaction-controlled kinetic effects (cf. Watson, 2004; DePaolo, 2011). Either or both assumptions may need to be relaxed in future iterations of the model.

4.3 Range of permissible supersaturation (Ω) *values*

The degree of supersaturation must be greater than unity to nucleate and grow a given phase. Upper bounds to the degree of supersaturation with respect to quartz and rutile can be estimated by considering the precursor phases and solubilities of the dissolving starting materials. Amorphous silica has a higher solubility than quartz by about a factor of 2, and the solubility of cristobalite is between that of quartz and amorphous silica (cf. Figure 2 in Walther and Helgeson, 1977). The direct precipitation

of cristobalite as a precursor to tridymite and quartz suggests an initial $\Omega_{qtz} > 1.5$ but we consider initial values of Ω_{qtz} from 1 to 2.

The solubility of anatase is not well known at temperatures above 325 ºC, but it is certainly higher than that of rutile, possibly by a factor of three or greater based on extrapolation of lower temperature data (cf. Kalyani et al., 2015). We consider initial values of Ω_{rut} in the range of 0-4 depending on whether rutile or anatase is used as starting material. A value less than unity implies that rutile or anatase dissolution is slow and that the fluid reaches quartz saturation faster than it reaches rutile saturation.

4.4 Model behavior

Model outputs for different values of $k'_{f,rut}$ (relative to $k'_{f,qtz} = 1$) are shown in Figure 2.10 to confirm the behavior of the model as described above. In all cases, the starting fluid is supersaturated in quartz. A lower initial Ω_{qtz} leads to a smaller range of Ti in quartz that is closer to the specified equilibrium value.

In Case 1-1, the fluid is initially undersaturated in rutile. According to Eqs. (5) and (6), [SiO_2] and [TiO_2] change monotonically with time at rates that depend on the respective k'_f values. The TiO_2/SiO_2 ratio of the fluid is initially low due to the high [SiO_2] and it increases monotonically because $r_f >> R_{rutile}/R_{qtz}$ for all three values of $k'_{f,rut}$. In this version of the model, if the fluid starts below rutile saturation, it stays below rutile saturation because both rutile and quartz are sinks of TiO_2.

In Cases 1-2 and 1-3, the fluid is supersaturated with respect to rutile. When $k'_{f,rut} \ll k'_{f,qtz}$, the TiO_2/SiO_2 ratio increases during the period of quartz precipitation due to TiO_2 exclusion and then decreases as the effects of rutile precipitation take over. When $k'_{f,rut} = k'_{f,qtz}$, the TiO_2/SiO_2 evolves to the equilibrium value on the timescale of SiO_2 removal. When $k'_{f,rut} \gg k'_{f,qtz}$, the TiO_2/SiO_2 decreases on the short timescale of rutile precipitation and then increases back to the equilibrium value on the longer timescale of quartz precipitation. Importantly, if the fluid starts above rutile saturation, it stays above rutile saturation because the sink of TiO_2 to quartz is insufficient to drive the fluid to rutile undersaturation.

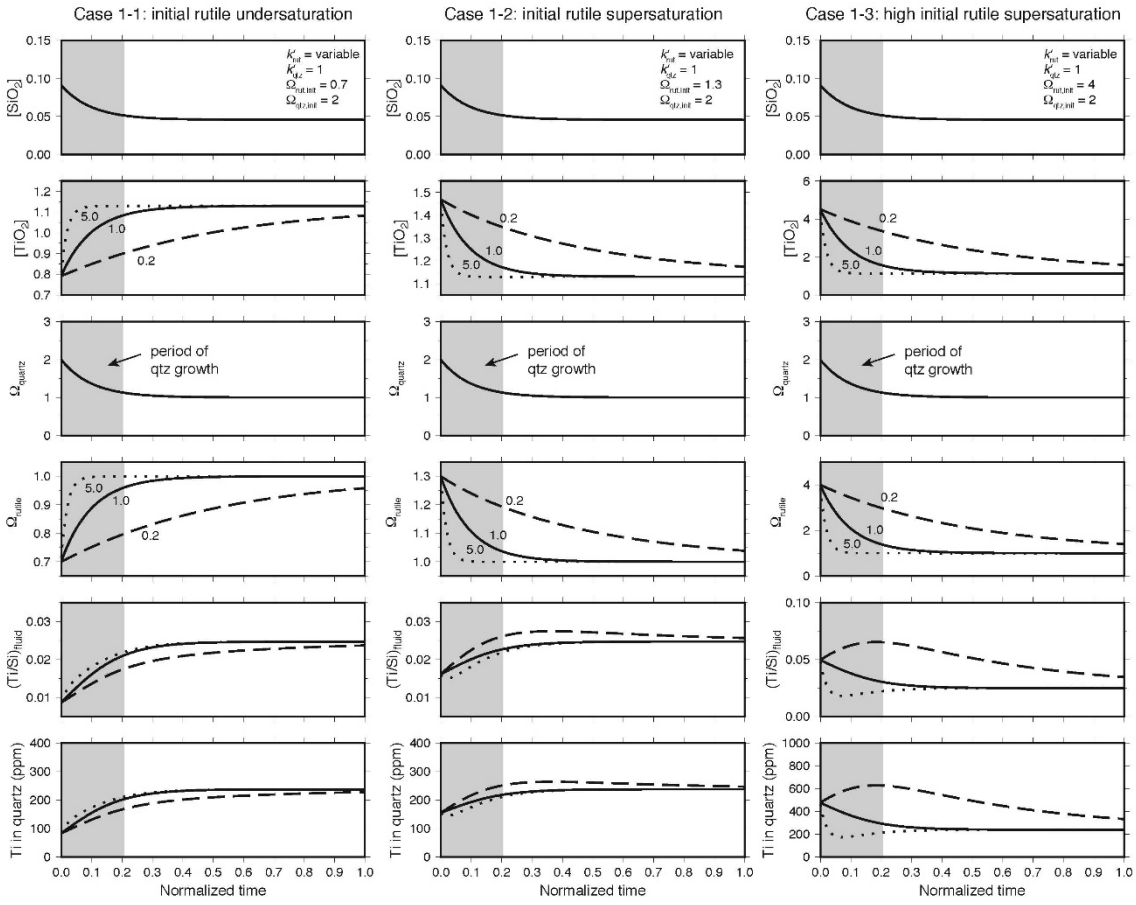

Figure 2.10 Model results showing the evolution of SiO_2 and TiO_2 components for different $k'_{f,rut}/k'_{f,qtz}$ values. Because the absolute values of $k'_{f,rut}$ and $k'_{f,qtz}$ are not known, the simulated time is arbitrary and we therefore normalize the time by the time at the end of the run. In all cases, the fluid is supersaturated with respect to quartz. In Case 1-1, the fluid is initially rutile-undersaturated, the TiO_2/SiO_2 ratio of the fluid is low but increases monotonically as quartz precipitates and rutile dissolves. In Case 1-2, the fluid is less supersaturated in rutile than in quartz, and consequently, the initial TiO_2/SiO_2 is below the equilibrium value. When rutile precipitation kinetics are slow ($k'_{f,rut}$= 0.2 $k'_{f,qtz}$), the Ti in quartz slightly overshoots the equilibrium value before rutile precipitation brings it back down. In Case 1-3, the fluid is more supersaturated in rutile than in quartz, and consequently, the initial TiO_2/SiO_2 is above the equilibrium value. The TiO_2/SiO_2 either increases or decreases before adjusting to the equilibrium value depending on which phase is precipitating faster.

4.5 Modified kinetic model (Model 2)

The initial treatment using constant $k'_{f,qtz}$, $k'_{f,rut}$, $K^{*}_{sp,rut}$, and $K^{*}_{sp,qtz}$ implies that the TiO_2 and SiO_2 components operate nearly independently from each other. Such independence, however, is belied by the extent to which use of anatase instead of rutile as a starting material influences the initial dissolution and subsequent crystallization of the SiO_2 component. There is some guidance in the recent literature for how to incorporate TiO_2-SiO_2 coupling into the model parameters. Mysen (2019) showed that the solubility of rutile increases substantially as aqueous silica concentration increases from zero to quartz saturation, and it is plausible that rutile solubility may further increase as the fluid becomes increasingly supersaturated with respect to quartz; e.g.,

$$K^{**}_{sp,rut}(\text{moles kg-soln}^{-1}) = 0.00061 \cdot \Omega_{qtz} + 0.00052, \quad (10)$$

which describes a line going from rutile solubility in a TiO_2-H_2O fluid ($\Omega_{qtz} = 0$) through rutile solubility in a quartz-saturated TiO_2-SiO_2-H_2O fluid ($\Omega_{qtz} = 1$) (Mysen, 2019).

Figure 2.12 shows Model 2 outputs for the same three initial rutile saturation states shown in Figure 2.10, given that $k'_{f,rut} \ll k'_{f,qtz}$. Case 2-1 shows that by incorporating the dependence of $K^{**}_{sp,rut}$ on Ω_{qtz}, an initial liquid that is undersaturated in rutile can become supersaturated and new rutile crystals can form. The outputs from Cases 2-2 and 2-3 show that the full range of Ti concentrations in quartz can be produced within the range of parameters we defined at the outset, provided that $k'_{f,rut} \ll k'_{f,qtz}$; i.e., that rutile is not serving as an effective buffer due to slow exchange with the fluid and/or low total reactive surface area.

5. Discussion

Complete mineral-fluid or mineral-mineral equilibrium is difficult to establish in experiments where high supersaturations are necessary to grow crystals within hours to days, as is well known from lower temperature crystal growth experiments involving almost any mineral including quartz. In the following subsections, we discuss the ways that high temperature quartz growth experiments are affected by kinetics and ultimately

conclude that, whether rutile or anatase is used as starting material, experiments with slow quartz growth rates are needed to retrieve both the equilibrium values and the values exhibited by quartz grown at low degrees of supersaturation in nature.

5.1. Interpretation of our experimental results

Our experiments and modeling show that a wide range of Ti concentrations in quartz can be produced under isobaric and isothermal conditions. Although the model doesn't account for the complex dissolution and crystallization pathways we observe and for the non-constant total reactive surface areas (folded into the k'_f terms), it is useful for evaluating which experiments may have been closer to quartz-rutile equilibrium and interpreting the sign and magnitude of departures from equilibrium.

5.1.1 The low solubility of rutile is advantageous for bringing the liquid up to rutile saturation

The low solubility of rutile implies that only a small fraction of the starting material needs to dissolve to establish saturation initially or re-establish saturation after a perturbation. The post-run rounded TiO_2 particles in outer capsules are interpreted to be incompletely dissolved and partially recrystallized rutile powder because the particle size is smaller than or roughly equal to that of the starting material. In the outer capsules where rutile powder was well-mixed with SiO_2, it is probable that quartz grew in an environment where $\Omega_{rut} \sim 1$ because the spacing between rutile particles is small and they are in close proximity to quartz.

5.1.2 Rutile is undersaturated in some parts of some of our experiments

The use of a single large crystal of rutile (Qz24b) or anatase (Qz27_ana) creates unfavorable conditions for a well-buffered liquid because the spacing between the large seed crystal and sparse, newly formed TiO_2 particles is high. Gradients in titania activity ranging from near zero to steep are likely responsible for producing Ti concentrations in outer capsule quartz that range from 14 ppm to 487 ppm. The exceedingly low Ti concentrations in the inner capsule (50 to 150 ppm), which overlap the low values of outer quartz from the same experiments, suggest quartz growth from a rutile-

undersaturated inner capsule fluid. Rutile needles protruding from the Qz24b overgrowth may have nucleated and grown towards the end of the period of quartz supersaturation and growth (Case 2-1 in Figure 2.11).

5.1.3 Once the fluid is rutile-saturated, it stays rutile saturated

The lack of rutile in quartz overgrowths does not necessarily imply quartz growth from a rutile undersaturated liquid; it only implies that the liquid was below the critical supersaturation required to nucleate rutile. In two of the experiments (Qz18 and Qz20), which agree with the results of HA12, we found newly formed rutile as inclusions near the seed-overgrowth interface. This suggests that a critical degree of rutile supersaturation was reached early in those experiments, and the next immediate question is whether the lack of rutile in later-formed overgrowth implies that the fluid became undersaturated in rutile, as suggested by TH15.

To determine whether a rutile-saturated fluid can become undersaturated, we ran the model with a low $\Omega_{rut} = 1.1$ and low $k'_{f,rut}$ to isolate the effects of quartz growth on the TiO_2 component. We find that quartz-driven rutile undersaturation requires an extremely high $\Omega_{qtz} \sim 5$ and a K_d that is an order of magnitude greater than what we estimate (Figure 2.12). Even with these parameters, the degree of undersaturation is minor (Ω~0.95) while the TiO_2/SiO_2 ratio is so high that it predicts Ti in quartz ~ 2200 ppm. The conclusion we draw is that once the fluid is saturated with respect to rutile, it should remain at or above saturation because neither quartz nor rutile growth is sufficient to drive the liquid to rutile undersaturation. We thus interpret the lack of rutile in most of the overgrowths as reflecting a liquid that is near saturation but below the critical supersaturation required to nucleate new rutile crystals.

5.1.4 Anatase promotes higher initial Ω_{rut}

When anatase is used as starting material, it should either dissolve and reprecipitate as rutile or convert directly to rutile via a solid-solid recrystallization pathway on a timescale of tens of minutes to tens of hours, depending on factors such as temperature, pressure, adsorbed impurities, particle size, the abundance of TiO_2 particles, and the amount of dissolved silica (Shannon and Pask, 1964; Zhang and Banfield, 1999;

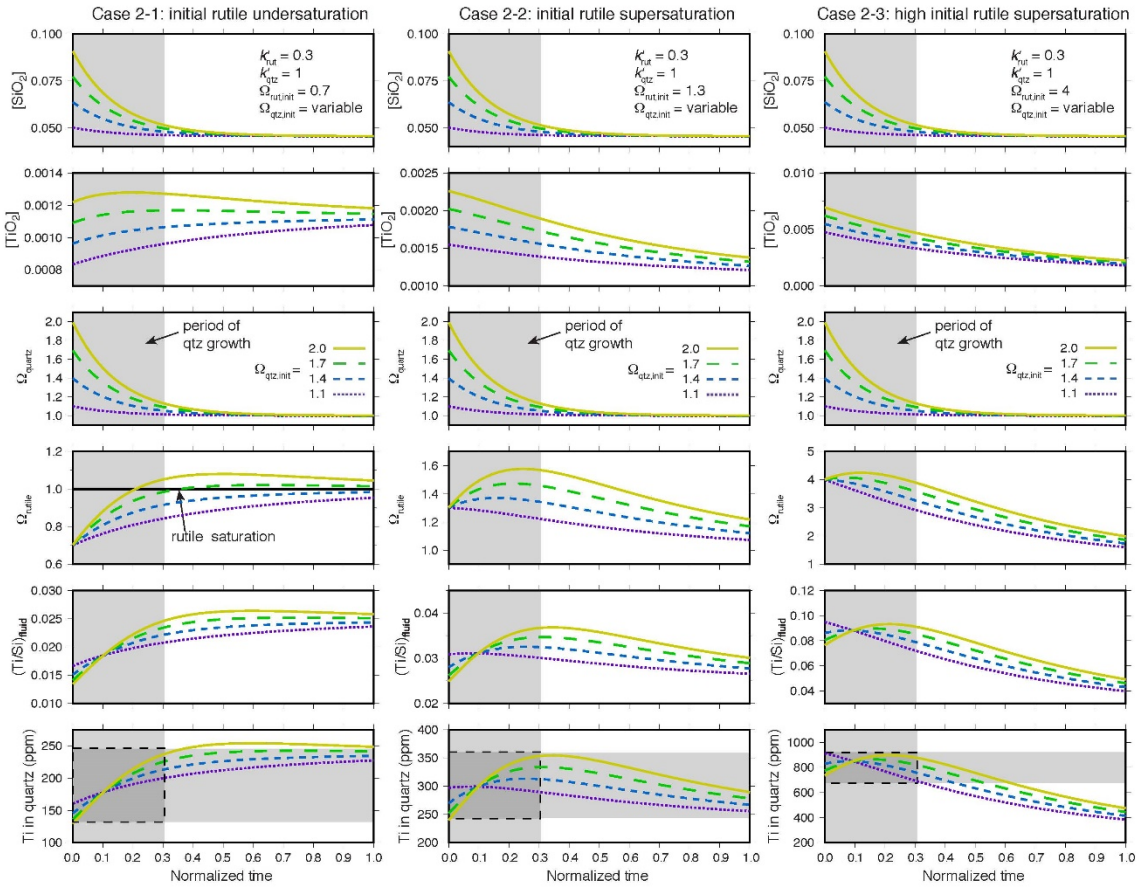

Figure 2.11 Model results that incorporate a solubility-dependence of rutile on the SiO_2 content of the fluid. In Case 2-1, the fluid is initially undersaturated in rutile, but Ω_{rut} increases as the SiO_2 concentration decreases, possibly explaining why the inner capsule overgrowths are coated in rutile but have few rutile inclusions. Case 2-2 shows that widely varying Ti concentrations in quartz can be produced when the fluid is initially supersaturated with respect to both quartz and rutile. Case 2-3 shows that when the fluid is highly supersaturated in rutile, the TiO_2/SiO_2 ratio remains high throughout the period of quartz precipitation for a wide range of Ω_{qtz} values.

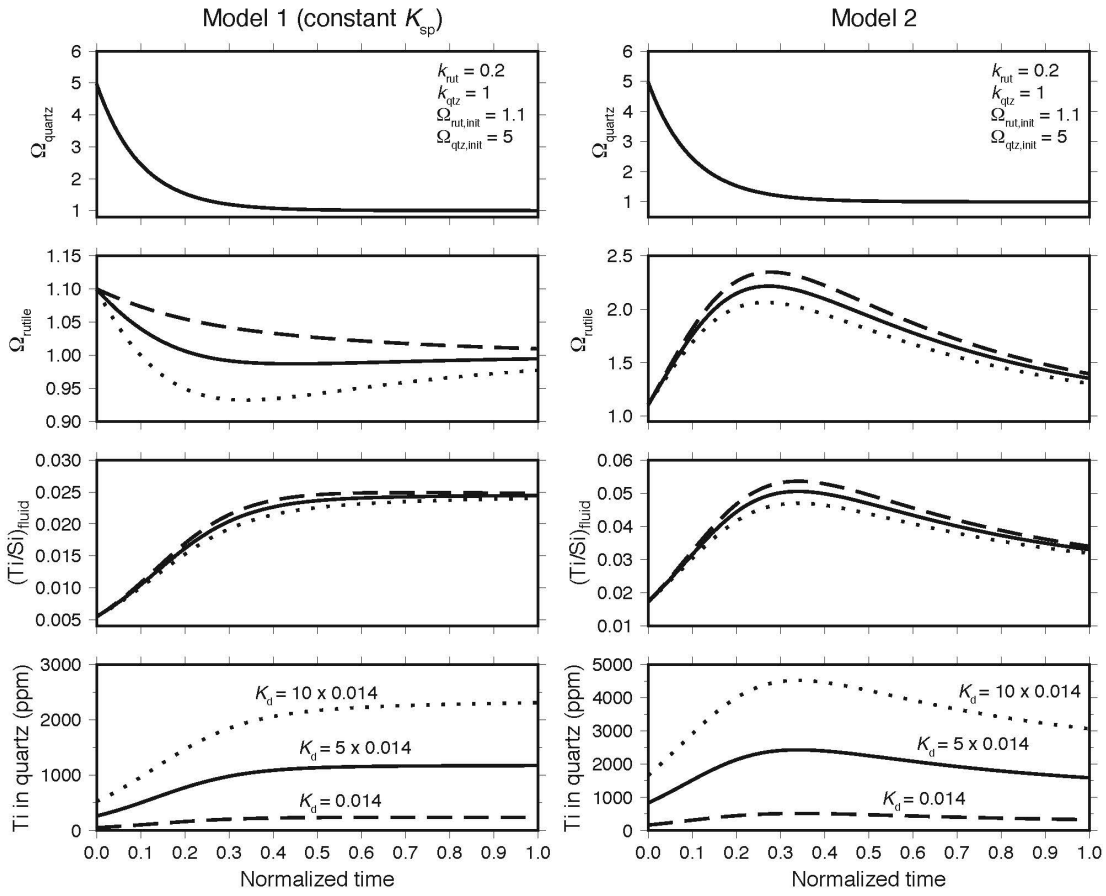

Figure 2.12 Model results testing whether TiO_2 incorporation into quartz can lead to rutile undersaturation. According to Model 1, a large degree of quartz supersaturation (Ω_{qtz} = 5) combined with high K_d (10 times the estimated value) can to lead a small degree of rutile undersaturation from a fluid that is initially slightly above saturation. According to Model 2, once rutile is supersaturated it stays supersaturated.

Okada et al, 2001; Gouma and Mills, 2001; Hanaor and Sorrell, 2011; Sabyrov et al., 2013). Anatase, a more soluble polymorph than rutile, dissolves quickly and is capable of establishing an initially very high Ω_{rut}, as evidenced by our 6-hour run where anatase precipitated directly from the liquid. A high initial aqueous TiO_2 concentration is consistent with higher Ti in outer-capsule quartz, reaching values >850 ppm, than in experiments using rutile as starting material (450-650 ppm; $n = 4$).

5.2 Kinetic effects in HA12 and TH10

The kinetic models show that there are many conditions that could promote Ti heterogeneity in the quartz crystals, but also conditions where relatively homogenous crystals can be grown far from equilibrium. The Ti in quartz variations among our run products span a broader range than those of HA12, and while our minimum Ti values in rutile-bearing overgrowths (Qz18 and Qz20) are comparable to their minimum Ti values (~267 ppm at 800ºC and 1 kbar), our results extend the high end of the range. HA12 used a single quartz crystal that dissolved at one end and precipitated at the other, thereby ensuring that quartz grows at relatively low degrees of supersaturation from a fluid that is near rutile saturation (Cases 2-1 and 2-2). Our higher values can be attributed to our use of silica glass, which promotes higher Ω_{qtz}, and the use of both rutile and anatase, which promotes a range of initial Ω_{rut} (Cases 2-1, 2-2 and 2-3).

The experiments of TH10 were conducted at higher pressures and they argued that the results can be safely extrapolated to low pressure (Thomas et al., 2015). TH10 interpreted their anatase experiments as having reached quartz-rutile equilibrium even though they grew quartz at much faster rates (tens to hundreds of microns/day) than HA12 (ones to tens of microns/day). The extreme growth rates alone argue against quartz growing from a fluid that is just above saturation, yet as Thomas et al. (2015) point out: "it is unlikely that a nonequilibrium process would have affected [our] results so consistently and systematically to produce the uniform Ti concentrations in quartz from individual experiments, and reproducible *P–T* dependencies of Ti solubility in quartz." Case 2-3 provides one way that relatively homogeneous crystals can form with excess Ti, but another possibility is that the fast growth rates alone can give rise to systematic kinetic effects that are not explicitly accounted for in the models.

5.3 Surface reaction-controlled kinetic effects

The outputs presented above assume a constant partition coefficient such that the crystal has a TiO_2/SiO_2 ratio that is offset from that of the fluid by a constant amount. This is a crude approximation because the partition coefficient itself is known to depend on the growth rate of the crystal (Watson, 2004; DePaolo, 2011; Watkins et al., 2017). A general expression for the non-equilibrium partition coefficient, K_p, is (DePaolo, 2011):

$$K_p = \left(\frac{a^{qz}_{TiO_2}/a^{qz}_{SiO_2}}{a^{liquid}_{TiO_2}/a^{liquid}_{SiO_2}}\right) \approx \frac{K_f}{1+\frac{R_b}{R_p+R_b}\left(\frac{K_f}{K_{eq}}-1\right)}, \quad (11)$$

where K_f is the forward kinetic fractionation factor for TiO_2/SiO_2 in the precipitation reaction; K_{eq} is the equilibrium TiO_2/SiO_2 partition coefficient; R_p is the net crystal growth rate (moles/s or moles/m^2/s, which can be converted to a linear growth rate in m/day using the molar density of quartz); R_b is the gross rate of ion detachment (same units as R_p). This expression describes a growth rate dependence to trace element uptake between an equilibrium limit at slow growth ($R_p << R_b$) and a kinetic limit at fast growth ($R_p >> R_b$). Such a kinetic limit has been documented for Sr/Ca in calcite without necessarily compromising its utility as a geothermometer (Gabitov and Watson, 2006). The crossover between the two limits occurs at $R_p \sim R_b$, but it is important to note that the functional forms of R_p and R_b can depend on many factors, including the degree of supersaturation, that are not well-known at this point. For Ti in quartz, there is an indication in the data of HA12 that increasing growth rate leads to higher Ti/Si in quartz, i.e., K_f is expected to be greater than K_{eq}.

A mechanistic explanation for the kinetic limit has yet to be developed, but we speculate that it may coincide with the regime where the step velocity (V_{step}) increases linearly with solution saturation (Rashkovich and Kronsky, 1997). For laboratory-grown potassium orthophosphate (KDP) crystals, for example, it is observed that at very low oversaturation, crystals are in a "dead zone" where the impurity molecules attached to growth steps inhibit the step advancement. At slightly higher oversaturation, V_{step} increases gradually with Ω, and with further increase in Ω, the $V_{step}(\Omega)$ curve increases

sharply until reaching a critical $\Omega = \Omega^*$, above which $V_{step}(\Omega)$ is linear. It has been found that crystals grown at lower supersaturation have many defects and fluid inclusions whereas crystals grown rapidly at high supersaturation have a homogeneous distribution of impurities and are defect-free – traits that could be mistaken for near-equilibrium growth (Zaitseva et al., 1999). If this behavior also applies to hydrothermal quartz, crystallization at low to moderate degrees of supersaturation could explain the abundant cavities and heterogeneous Ti concentrations in our run products as well as those from HA12 and may indicate that the high supersaturation linear regime is more accessible at high pressure.

5.4 Solubility of Ti in quartz

Based on all of the considerations discussed herein, we suspect that many of the experimentally grown quartz crystals are supersaturated with respect to rutile. A certain degree of supersaturation is always required to nucleate and grow a new phase, and the kinetic barrier to spontaneous nucleation of rutile from quartz is likely to be large because the Ti atoms, if uniformly distributed, are separated from each other by tens to hundreds of Si atoms. It thus seems plausible for the quartz lattice to be able to accommodate Ti significantly in excess of the saturation value. In the thermal annealing experiments of TH15, for example, the quartz starting material was supersaturated in TiO_2 by at least a factor of 3-4, and yet, the relict quartz cores retained their high Ti and appear to have not exsolved rutile during the four days they were held at 925 ºC and 20 kbar.

A recent study provides additional evidence that the highest experimental Ti concentrations in quartz at a given T and P overestimate the equilibrium solubility value. Nachlas and Hirth (2015) ran dynamic recrystallization experiments involving laboratory-synthesized low-Ti silica gel (110 ppm Ti) and high-Ti silica gel (2280 ppm Ti). The two aggregates were pressed together and then sheared at 10 kbar and 900ºC. Under these conditions, the gel crystallized to quartz and the quartz recrystallized continuously during shear deformation. The equilibrium Ti was expected to be either 310 ppm (TH10) or 101 ppm (HA12), depending on which calibration is used. The high-Ti half exsolved rutile, as expected, and the recrystallized quartz had Ti concentrations broadly overlapping results from HA12 and well below the predictions of TH10. It is

difficult to rationalize why the high-Ti side (2280 ppm) of these deformation couples would overshoot the 310 ppm equilibrium value of TH10 if that were the true equilibrium concentration.

5.5 Additional considerations

The TH10 calibration was carried out at high pressures (5-20 kbar) whereas the pressure range over which TitaniQ has been applied to well-constrained samples is considerably lower (1-4 kbar; Supp. table). This raises the question of whether the disagreement between HA12 and TH10 might be caused by an unusual pressure dependence (curved isopleth). A recent calibration by Zhang et al. (2020) using silicate melts instead of solutions suggests that this may in fact be the case and comes close to reconciling the experimental results, though significant discrepancies remain between this calibration and the experiments of HA12, TH10, and Nachlas and Hirth (2015) where they overlap in pressure at 10 kbar. Once the equilibrium solubility and its functional form are more firmly established, the framework we developed herein should prove useful for explaining residual kinetic effects and why different experimental configurations can yield different results.

6. Conclusions

Our Ti-in-quartz results at 800°C and 1 kbar span the range of previous calibrations. The two endmember interpretations for the wide range are: (1) the wide range reflects variable degrees of rutile undersaturation ($0 < \Omega_{rut} < 1$) in a system where extrapolation of the TH10 calibration reflects equilibrium or (2) extrapolation of TH10 overestimates the equilibrium value and the wide range reflects variable degrees of rutile under- and over-saturation ($0 < \Omega_{rut} <$?) as quartz grows from variably supersaturated liquids ($1 < \Omega_{qtz} < 2$).

We developed models to account for the complexities inherent in the experiments, but the only models that appear capable of explaining the textures we observe (incomplete dissolution of rutile starting material, complete dissolution-recrystallization of anatase starting material, rutile inclusions in quartz, and rutile coating the surfaces of quartz) involve slow rutile precipitation rates and a dependence of TiO_2 saturation state

on SiO_2 saturation state. The latter effect has been documented in a recent rutile solubility study (Mysen, 2019). Our conclusion, which is based on application of TitaniQ to natural samples along with our new results and models, is that the HA12 experiments at low pressure are a better analog to natural quartz than extrapolation of the TH10 results at high pressure, indicating that a curved isopleth describes Ti-in-quartz solubility (HA12; Zhang et al., 2020). More work is needed to reconcile remaining discrepancies among the various experimental studies and to design and interpret experiments aimed at estimating equilibrium TiO_2 concentrations in quartz.

7. Bridge

The incorporation of Ti into quartz during high temperature and pressure experiments has been shown to be dependent on many factors, such as the TiO_2/SiO_2 ratio of the fluid and quartz growth rate. However, the complexity of Ti-in-quartz does not preclude its utility as an indicator of geochemical processes. In the next chapter, growth and deformation textures present as heterogeneous Ti distributions in hydrothermal vein quartz from the Butte, MT porphyry Cu-Mo deposit are used to reconstruct the sequence of quartz vein formation at the base of the deposit.

CHAPTER III

TEXTURES OF QUARTZ-MOLYBDENITE VEINS IN THE BUTTE, MONTANA PORPHYRY COPPER DEPOSIT INDICATE VEIN STRAIN DURING DEPOSIT FORMATION

This chapter is currently unpublished and is co-authored by Mark Reed and James Watkins. Data was collected by me and interpreted by me and Mark Reed. All co-authors contributed to the ideas presented herein. The manuscript was written by me with significant edits from both Mark and Jim.

1.Introduction

Quartz vein stockworks in porphyry copper deposits form when overpressured fluid above a crystallizing magma chamber invades the country rock and precipitates minerals in the fractures. Vein minerals and adjacent alteration envelopes change mineral content through time as the fluids decompress and cool from near-magmatic temperature (~700ºC) in the early stages to 350ºC and below (Reed et al., 2013).

Cathodoluminescent (CL) intensity of quartz from Butte correlates positively with Ti concentrations (Rusk et al., 2002; Rusk et al., 2006; Rusk et al., 2008b) so CL images of quartz show relative Ti enrichment and depletion. CL textures can thus be used to reconstruct quartz crystal growth and dissolution, as well as deformation. Identifying histories that create unique CL textures, such as the CL-mottled and CL-euhedral textures described herein, is the first step to using quartz CL to recreate vein formation and deformation processes.

2. Geology of the Butte District

The Butte ore deposit has been mined since 1864, first for placer gold deposits and later for silver and copper in the vein system, and its geology has been studied for almost as long (Reed and Dilles, 2020). The 65 Ma Butte porphyry Cu-Mo deposit is hosted in the Butte granite (Figure 3.1a; Smedes 1973; Tilling, 1974) whose homogeneity eliminates complications caused by non-uniform country rock, making Butte an exceptional study area to examine fundamentals of porphyry Cu formation.

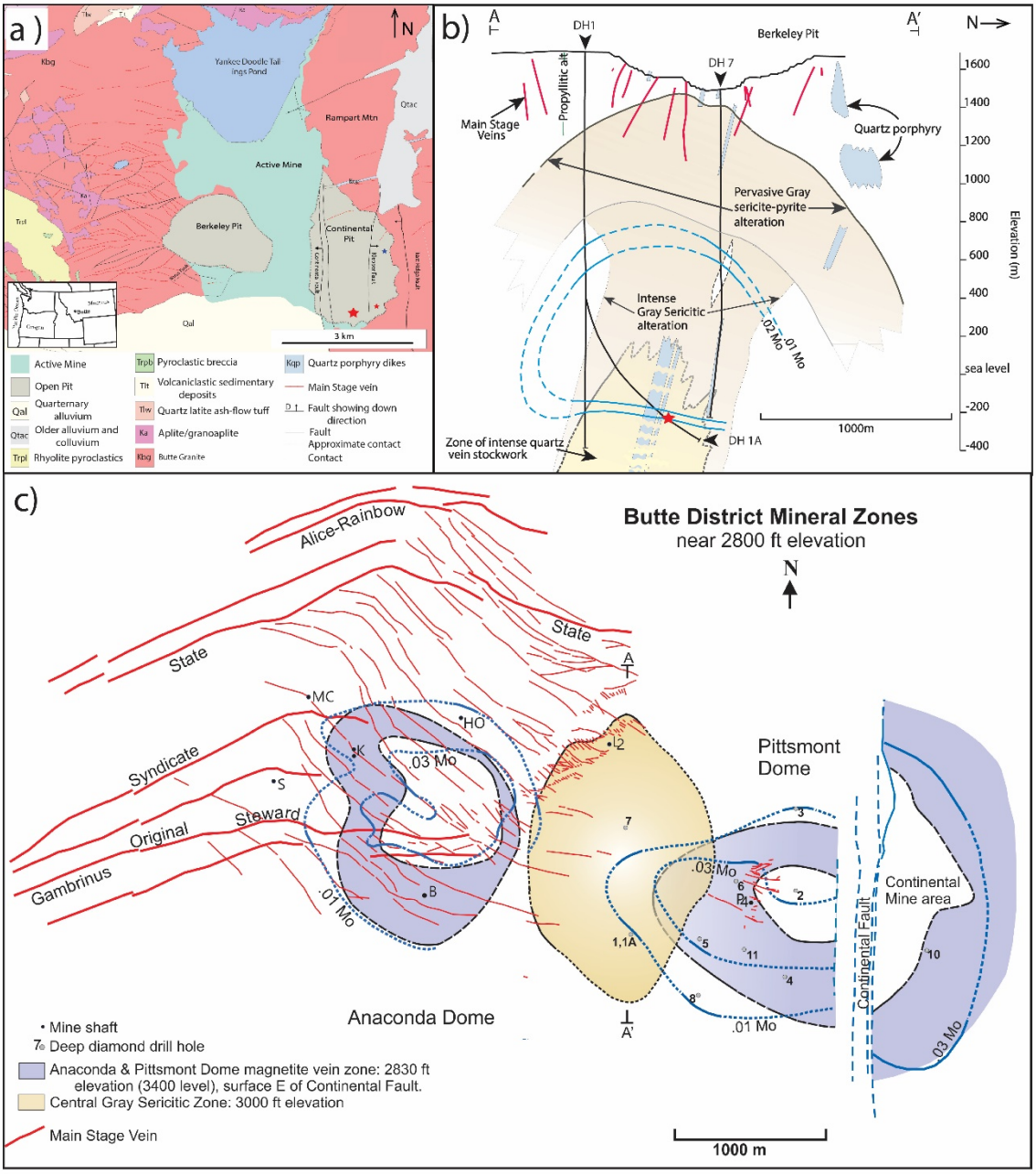

Figure 3.1 The Butte, MT porphyry Cu-Mo deposit is an actively mined in an open pit to the west of the Continental Divide. A) a simplified geologic map of the region based on a map by Houston and Dilles (2013). B) a cross section through the Anaconda dome from which deep drill core samples that intersected a basal region of intense quartz stockwork were taken. C) Map of Butte Main Stage veins and pre-Main Stage magnetite vein zones and Mo grades. Mine shafts: B, Belmont; HO, High Ore; K, Kelly; L2, Leonard #2; MC, Mountain Consolidated; P4, Pittsmont #4; S, Steward. There are two porphyry centers separated from one another by a region of Grey Sericitic alteration. The Pittsmont Dome, the eastern center, is cut by the Continental Fault. Panels B and C are modified from Reed et al. (2013).

Two different hydrothermal events created two types of vein ore in Butte. The first is the early porphyry Cu mineralization known as the pre-Main Stage, and the second is the late Cordilleran-style base metal veins of the Main Stage. The pre-Main Stage porphyry Cu-Mo ore formed at depths of ~5-9 km (Rusk et al., 2008a). The younger Main Stage polymetallic veins formed at shallower depths and occur primarily as fissure fillings in faults (Houston and Dilles, 2013). The recently-examined genetic link between porphyry deposits and epithermal deposits supports the idea that the Main Stage veins result from the late evolution of the Butte porphyry copper system, and are the roots of an epithermal deposit that has been eroded away (e.g. Sillitoe & Hedenquist, 2003; Einaudi et al., 2003; Heinrich, 2005; Pudack et al., 2009; Maydagan et al., 2015).

The Butte system has two concentrically zoned porphyry Cu-Mo centers - distinguished by separate magnetite vein zones and closure of molybdenum grade contours (Figure 3.1c). Each dome is approximately 2 km wide. The western Anaconda dome is separated from the eastern Continental-Pittsmont dome by a bulbous region of intense pyrite veins and pervasive grey sericitic alteration that is 1.2 km wide and extends 2 km deep below the Berkeley pit (Figure 3.1b).

Pre-Main Stage and Main Stage alteration and mineralization types and relationships have been extensively documented elsewhere (e.g. Meyer, 1965; Brimhall, 1973; Roberts,1975; Reed et al., 2013). The earliest veins of the potassic series are quartz-chalcopyrite-pyrite veins with biotite, K-feldspar, and sericite alteration envelopes ("EDM" veins; Meyer, 1965), which include biotite crackles connected to biotite breccias surrounding the apices of quartz porphyry dikes. Biotite crackles are microscopic quartz veinlets with haloes of wall rock altered to biotite, muscovite, and K-feldspar; biotite breccias consist of subangular/subrounded wall rock clasts in a matrix of biotite + quartz + K-feldspar + pyrite hydrothermal breccias with subangular/subrounded wall rock clasts in a matrix of biotite + quartz + K-feldspar + pyrite (Brimhall, 1973). EDM veins vertically grade through a series of alteration types that form because of a single parent fluid cooling and interacting with wall rock at various water-rock ratios (Reed et al., 2013). These sulfide-bearing quartz veins are cut by barren quartz/quartz molybdenite veins. The term "barren" here is a field term that refers to veins with only trace amounts of molybdenite. Barren quartz veins are the deepest veins and form a stockwork at the

base of the deposit. Some barren quartz veins grade upwards into quartz-molybdenite veins. The youngest pre-Main Stage veins are pyrite-quartz veins with grey sericitic (GS) alteration in which igneous plagioclase and K-feldspar are replaced by quartz, muscovite, and pyrite and igneous biotite and hornblende are altered to mixtures of muscovite, pyrite, quartz, Mg-chlorite and rutile (Reed et al., 2013).

A barren quartz vein stockwork is typical in the root zones of many porphyry Cu-Mo deposits (Sillitoe, 2010; Müller et al., 2010). The barren quartz and quartz-molybdenite veins generally lack alteration envelopes although thin envelopes containing biotite or K-feldspar occur in the deepest of samples (Reed et al., 2013). This lack of alteration can be attributed to sudden decompression that precipitates quartz, filling the fractures on a time scale short enough to prevent chemical diffusion along wetted grain boundaries in the host rock (Rusk and Reed, 2002; Rusk et al., 2008a; Reed et al., 2013). In this contribution, we focus on barren quartz from the deep central zone intersected by DH1A (Figure 3.1b) where molybdenite-bearing veins are nearly absent, and on quartz-molybdenite veins from a shallower region exposed in the Continental Pit where barren quartz veins are rare.

Earlier investigations into barren quartz/quartz-molybdenite veins revealed two cathodoluminescence (CL) textures (Rusk and Reed, 2002; Rusk et al. 2008b) hereafter referred to as ‘CL-euhedral’ and ‘CL-mottled’. CL-euhedral texture consists of alternating dark and light growth zones of euhedral crystal faces reflecting primary crystal growth from a hydrothermal fluid. CL-mottled crystals have a CL-gray background that is unevenly dappled with darker regions. While the formation of CL-euhedral textures reflects straightforward crystal growth zoning, the cause of CL-mottled texture remains enigmatic. CL-mottled quartz is contiguous with CL-euhedral quartz in banded veins that reflect multiple mineralizing pulses as well as in monogenetic veins that lack the banding indicating re-opening. In this contribution, we explain the co-existence of these textures and argue that they reflect preferential ductile deformation of crystals in vein centers shortly after vein formation.

3. Methods

Samples are drill core from deep drill hole 1A (DH-1A), an angled hole that intersected the barren quartz stockwork (Figure 3.1b), and from highwall exposures on the C-East pushback of the Continental pit (Figure 3.1a). Petrographic descriptions of thick and thin sections were made with a polarized light optical microscope and the same samples were scanned at high resolution (3200 dpi) in both cross-polarized and plane polarized light using a 4000 dpi Nikon slide scanner. Recrystallization microstructures indicative of subgrain rotation, bulging recrystallization, and grain boundary migration were documented from thin sections using a petrographic microscope (Figure 3.2). Representative samples of barren quartz stockwork, a quartz-molybdenite vein, and a monogenetic Main Stage vein were analyzed in greater detail using methods described below. All analyses were carried out in the Center for Advanced Materials Characterization in Oregon (CAMCOR) at the University of Oregon.

3.1 SEM-CL

Thick sections were cleaned with ethanol, coated with ~50 microns of carbon, then imaged in a FEI Quanta 200 FEG environmental scanning electron microscope (SEM) at 15 keV with a beam current of 40 nA. Greyscale cathodoluminescent (CL), secondary electron (SE), and backscattered electron (BSE) SEM images were collected, and major phases were identified using energy dispersive spectroscopy (EDS).

Initial comparisons among different types of microscopic images of the same sample relied on identifying distinctive features that could be correlated in the images. Three samples were correlated more precisely using PictureSnapApp (downloadable software from Probe Software, Inc.). Using this software, high resolution scans of thin sections can be uploaded and calibrated with the sample in the SEM chamber so that the scan can be used for navigation.

3.2 Electron Microprobe

A representative quartz-molybdenite vein (sample BMA-018-16fa_15) with no macroscopic evidence of rebreaks, minor amounts of molybdenite, and macroscopically massive quartz was selected for Ti measurements by EPMA. On this sample, 146 Ti

analyses on four CL-euhedral and two CL-mottled crystals were collected in CAMCOR at the University of Oregon on a Cameca SX100 electron microprobe equipped with five wavelength dispersive spectrometers. Operating conditions were: 40 degree takeoff angle, beam energy of 15 keV, beam current of 100 nA and beam diameter of 5 microns. Ti Kα was measured on all spectrometers and aggregate mode was turned on. The counting time was 425 seconds for quartz, MgO, NiO, and MnO standards and the intensity data were corrected for time dependent intensity loss (or gain) using a self-calibrated correction for Ti Kα. Mean atomic number (MAN) background intensity data were calibrated and the Bremsstrahlung continuum absorption corrected for Ti Kα (see Donovan et al., 2016 for details). Unknown and standard intensities were collected for deadtime. Standard intensities were corrected for standard drift over time. A quantitative blank correction with the quartz standard as a known unknown was applied.

In addition to the quartz-molybdenite vein, two samples of barren quartz stockwork from DH-1A, 11052-6121 and 11052-6019, were analyzed for Ti, Fe, K, and Al. For these runs, Ti was measured simultaneously on a standard and on a large pentaerythritol crystal. Operating conditions were: 40 degree takeoff angle, a beam energy of 20 keV, a beam current of 200 nA, and a beam diameter of 20 micron. Standards were synthetic TiO_2 for Ti Kα, orthoclase MAD-10 for Al Kα and K Kα, and magnetite U.C. #3380 for Fe Kα. Counting times were 450 seconds for all elements, and a MAN background was used.

3.3 Correlating CL intensity with Ti concentration

As noted above, there is a general positive correlation of CL intensity with Ti concentration, but the correlation is not exact owing in part to the presence of other CL-activators and dampeners, such as Al, which dampens the total intensity of quartz CL response. A second effect is that the CL brightness in any given image depends on the gain and offset on the CL detector set by the operator to either emphasize greyscale midtones in the image or to enhance contrast. In any given CL image, it is generally acceptable to interpret the brighter regions as having higher Ti and the darker regions as having lower Ti. It is not, however, correct to analyze only the bright and dark regions of a CL image and to interpolate Ti concentrations in regions of intermediate intensity. It is

likewise incorrect to compare the intensities in different CL images acquired at different operating conditions. So, "bright" in one image is not the same amount of "bright" as in another image but is rather bright relative to the other CL-active areas in that same image. Rusk et al. (2006) detail a method by which to quantify CL-intensity and discuss the relationships between CL-intensity and Ti in Butte quartz.

4. Results

4.1 Hand Sample and Petrographic Features

4.1.1 Barren quartz veins from DDH-1A

The quartz stockwork in drill core DDH-1A consists of 0.1-7 cm thick massive barren quartz veins. In any given ~10 m of core there are quartz veins with sharply defined planar or undulose edges (see Appendix B) that co-exist with veins that do not have an obvious margin, but rather, have diffuse gradational contacts that bleed into the country rock. Much of the country rock is intensely silicified or "quartz flooded." Altered wall rock, whether Quartz Porphyry or Butte Granite, is GS altered and has in order of decreasing abundance: quartz, sericite, disseminated pyrite and trace chalcopyrite. Where

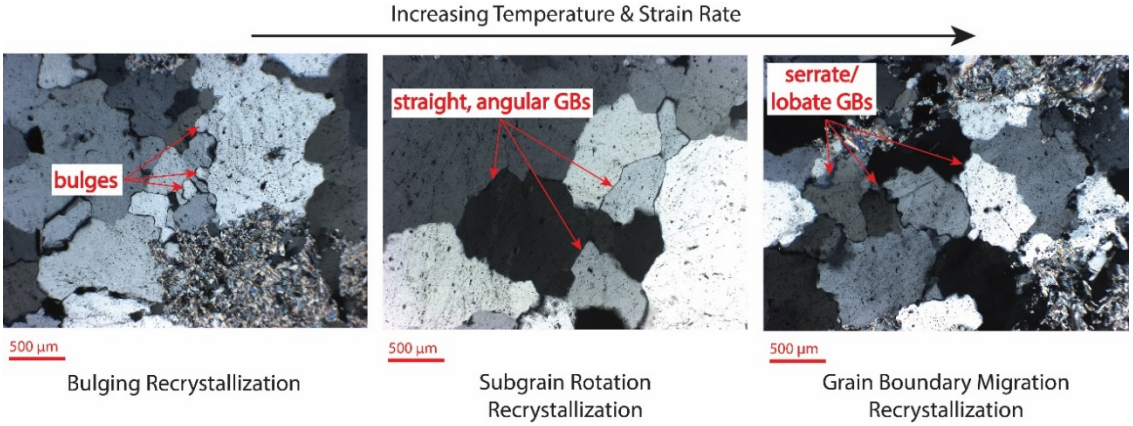

Figure 3.2 There are three quartz recrystallization regimes, each of which creates distinctive textures in thin sections. Pressure, temperature, and stress conditions dictate which regime dominates during quartz deformation. Bulging recrystallization is the lowest temperature regime (active between 250 and 400 °C) and is also favored by high strain rates. The eponymous bulges of this regime are newly crystallized subgrains whose formation is driven by variation in dislocation density. As a bulge ripens it becomes a discrete grain, and so this regime can result in a bimodal grain size distribution where larger and older crystals are mantled by younger and newer crystals that are much smaller. Subgrain rotation operates between 400 and 500 °C. Grain boundary migration, the highest temperature recrystallization regime, is active between 500 and 600 °C and is characterized by coarse crystals with lobate and serrate grain boundaries.

present, molybdenite occurs as small (<5 mm) cryptocrystalline blebs near the edges of veins or dispersed throughout the recrystallized quartz regions.

Barren quartz veins from the stockwork are completely recrystallized but show no crystal fabrics or preferred orientations (Figure 3.2). The recrystallized quartz crystals range in size from 0.05 to 0.2 mm and exhibit dominantly grain boundary migration microstructures such as lobate grain boundaries but features indicative of subgrain rotation and bulging recrystallization grain boundary forms are also present. Other deformation features include undulose extinction, slightly misoriented domains within crystals, subgrains locally decorating grain boundaries, and some grains have weak deformation lamellae. Grains with deformation lamellae are isolated; surrounding grains do not have lamellae and tend to fall into the larger end of the size range. Recrystallized grains contain anhedral fluid inclusions that are randomly distributed throughout the crystal.

4.1.2 Quartz-molybdenite veins

Quartz-molybdenite veins are planar and are ~0.1 to 13 cm thick. The larger veins are distinctly banded with quartz and streaked molybdenite. Molybdenite is microcrystalline and most commonly occurs as thin discrete layers 5-20 mm thick along the edges of veins either mixed in with fine-grained quartz crystals or as a molybdenite-only layer. In smaller veins, the molybdenite layers are predominantly planar, but in larger veins many of the molybdenite layers are arcuate and swoop through interior quartz creating a marbled effect (see Appendix B). Microscopic flecks of molybdenite are also dispersed throughout quartz-rich regions. Intra-vein layer thicknesses range from ~0.2 to 2 cm. The veins lack alteration envelopes. The wall rock has undergone pervasive Main Stage White and Green Argillic alteration, characterized by kaolinite and montmorillonite replacement of feldspar.

Quartz-molybdenite veins are lined along their edges with 0.1-1 cm CL-euhedral cockscomb quartz and filled in the center with equigranular quartz, almost all of which is CL-mottled; rare isolated CL-euhedral crystals with CL-mottled edges can be found in vein centers. The cockscomb-edge quartz crystals are all oriented with their c-axes roughly perpendicular to vein wall, as indicated by oriented negative crystal-shaped fluid

inclusions of types B35 and B60 (cf. Rusk et al., 2008a). The equigranular vein centers consist primarily of quartz crystals ranging in size from 20 to 200 μm. Crystals of 20 to 70 μm size are volumetrically dominant and most have straight grain boundaries. These smaller crystals do not display undulose extinction, although they are mottled in CL, but larger crystals (100-200 μm) do exhibit undulatory extinction and occur either as isolated crystals or as clusters surrounded by smaller grains. These small grains are classic neocrysts formed during subgrain rotation and bulging recrystallization (Figure 3.2). For larger grains in clusters, grain boundaries are lobate, and misoriented subgrains are plentiful. All recrystallized quartz types contain many small, irregularly shaped fluid inclusions as well as larger (>0.002 mm) unidentified mineral inclusions. The irregular morphologies of these secondary inclusions are characteristic of fluid inclusions that have been broken up and dispersed throughout a crystal during grain boundary migration recrystallization. Where inclusions were intersected during polishing, pitted pock marks are left behind on the otherwise polished surfaces.

4.1.3 Shallow Main Stage vein

The Main Stage vein sample (BMA-020-16fa) was taken from a highwall in the easternmost Continental pit and does not have recrystallization microstructures. The quartz vein is 2 cm wide and the Butte Granite surrounding the vein is pervasively White Argillic, not in the form of an envelope, but instead as a broad wash in this part of the pit. There is also abundant chalcopyrite and residual igneous biotite in the wall rock. This sample is representative of Main Stage veins from moderate depth that have not recrystallized. The vein is symmetrically zoned about the center, starting at the wall rock with a 2 mm layer of microcrystalline milky quartz, overlain by a <1 mm layer of clearer microcrystalline quartz, and a third <1 mm layer of milky quartz from which macroscopically euhedral 0.3 mm comb quartz crystals project into the center of the vein. Irregularly spaced pockets in the center of the vein contain chalcopyrite, pyrite, and bornite—a common Main Stage mineral assemblage. The center of the vein contains many vugs lined with euhedral 1 mm wide quartz crystals that are 0.5-2 mm long.

4.2 SEM-CL imaging

4.2.1 Barren quartz/quartz-molybdenite CL textures

Barren quartz vein samples from DDH-1A are entirely CL-mottled. Quartz-molybdenite veins from the Continental pit (the Pittsmont dome) have the following sequence of textures, from the edge of axisymmetric quartz veins to the centers: granite (or aplite, or quartz porphyry) fracture surface, a thin layer of CL-mottled crystals, a layer of cockscomb CL-euhedral quartz crystals, a central layer of CL-mottled crystals (Figure 3.3). The outermost thin (~10 microns) layer of CL-mottled crystals that line the granite-vein fracture surface is overlain by a layer of 0.5 - 2 mm long CL-euhedral quartz crystals that have oscillatory zonations. Growth zones in CL-euhedral crystals are of variable thicknesses from core to rim. The edges of some individual CL-euhedral crystals display a mottled texture. CL-mottled crystals ranging in size from 10 to 30 microns fill the centers of veins and dominate the volumetric bulk. Some crystals in the center zone have a "ghost" CL texture that is intermediate between CL-euhedral and CL-mottled, wherein what appear to be relict CL-euhedral oscillatory bands have been smoothed into one another (Figure 3.4). Individual bands in CL-euhedral crystals are as thick as 25 microns and as thin as <1 micron, and most have sharp boundaries against adjacent CL-dark bands. Most are between 10 and 15 microns thick. Oscillatory zonation patterns track from one crystal to the next in cockscomb layers.

4.2.2 Shallow Main Stage vein CL textures

The Main Stage quartz vein displays striking breccia and cockscomb quartz textures. Layers of comb quartz exhibit euhedral oscillations that are continuous from one crystal to the next (Figure 3.5). In the center of the vein are smaller, randomly oriented, euhedral quartz crystals with unique banding patterns in their cores. These unique cores of single crystals are encrusted in rims whose banding patterns track from one encrusting crystal to the next (Figure 3.5c insets). Clasts that could be rip-ups of dark CL-

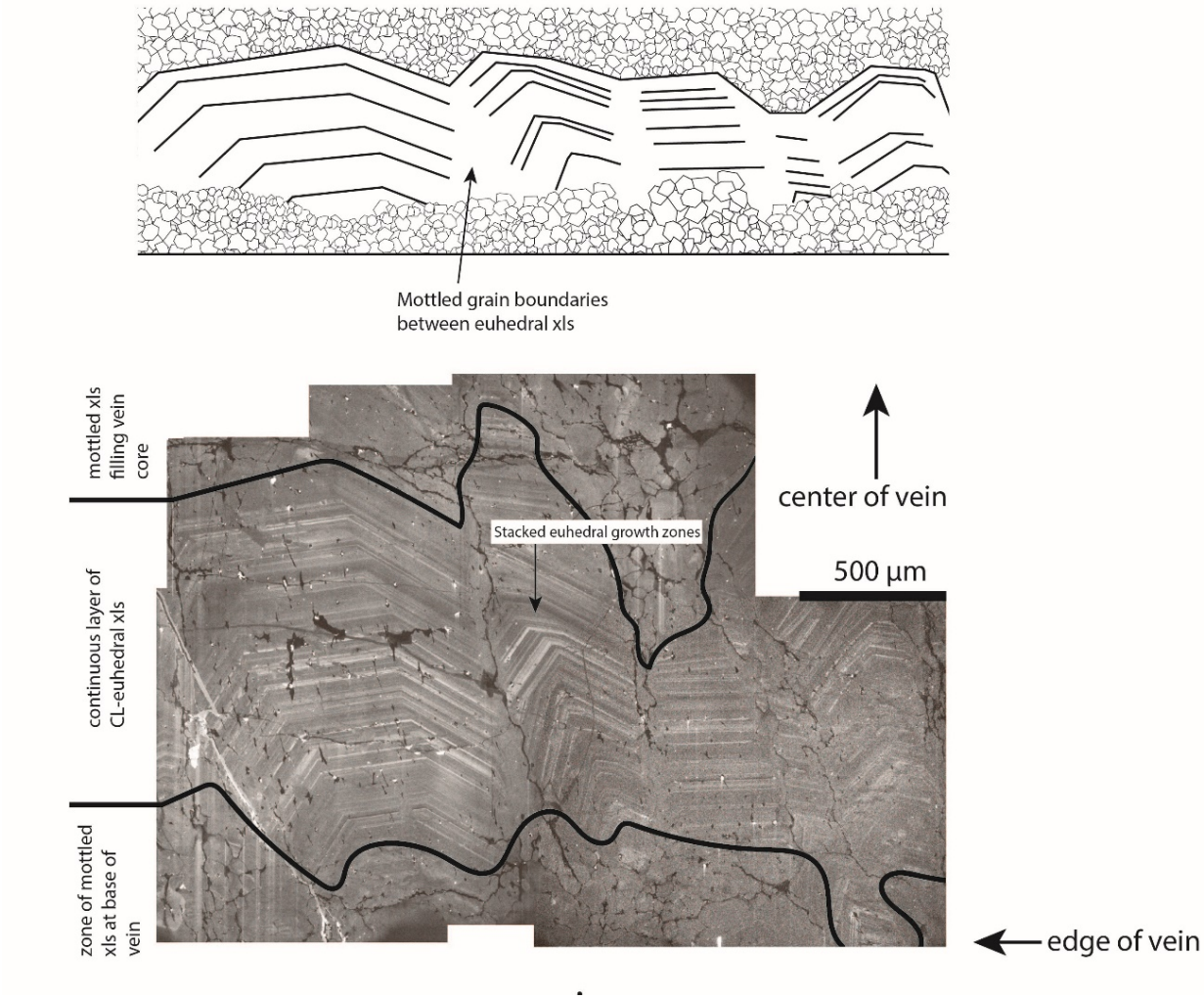

Figure 3.3 The fractured edges of quartz-molybdenite veins are overlain with a thin layer of recrystallized CL-mottled quartz that are in turn the substrate for a continuous layer of CL-euhedral coxcomb quartz. Centers of veins are CL-mottled. In the simplest case of a monogenetic, axisymmetric vein, the initial layers of randomly oriented quartz crystals and coxcomb quartz form as a consequence of geometric selection during growth and a vein-filling cores of randomly oriented crystals form as the vein solidifies. During or shortly after vein closure, recrystallization of randomly oriented crystals occurs. The bright linear feature in the lower left corner is a fracture, and the vertical streaks below it are a scanning artifact. Mottled boundaries of adjacent CL-euhedral cockscomb quartz are due to localized recrystallization of grain boundaries due to thermally activated grain boundary movement driven by surface free energy minimization due to lattice mismatch between the two crystals (the original boundary is imperfect but reorganizes to a stable geometrical configuration when annealed).

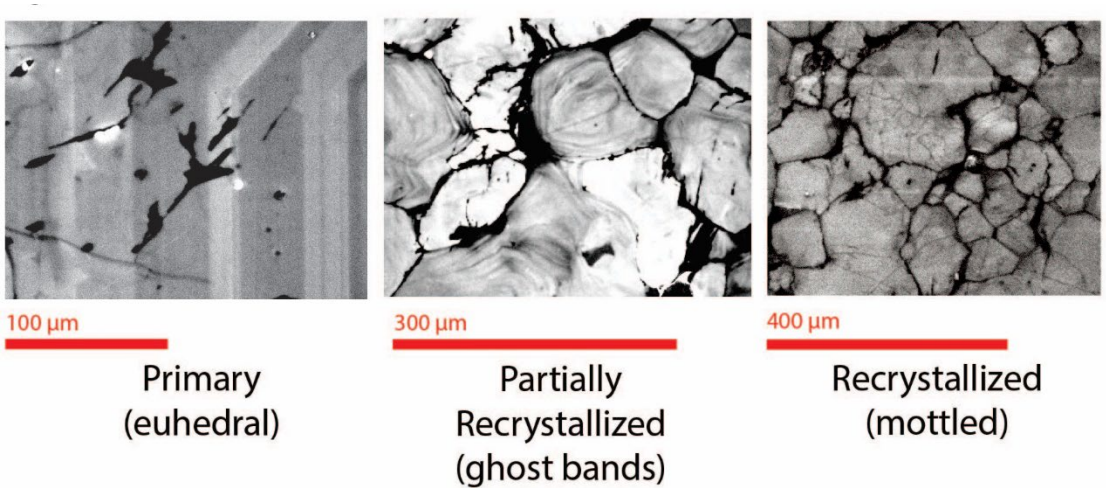

Figure 3.4 Most CL-euhedral zones from Butte have sharp boundaries. Partially recrystallized quartz crystals preserve wavy remnants of CL-euhedral growth bands that have been blurred into one another, while more thoroughly recrystallized quartz is CL-mottled.

homogeneous quartz occur in the center of the vein and crustiform CL-euhedral quartz mantles these clasts (see Appendix B).

Other textures include heterogeneous and chaotic (Figure 3.5c) sharply defined, angular domains of CL-bright quartz truncated by CL-dark quartz. This texture is hereafter referred to as CL-chaotic. Additional images of CL-chaotic texture are in Appendix B. CL-chaotic texture consists of domains of angular or rounded homogeneous or heterogeneous CL-bright juxtaposed against a CL-dark backdrop. Heterogeneity in the CL-bright domains occurs as CL-grey feathers or wavy regions with slightly less CL intensity. In some regions of the texture, CL-bright domains are plumose or flame-like. Regions of CL-euhedral quartz occur sporadically within chaotic regions. It is notable that, despite the complexity and small scale of the CL-chaotic texture, it is not formed of clusters of microcrystals. In other words, in thin section (Figure 3.5a), CL-chaotic crystals are optically continuous and relatively large (100 – 500 microns) while CL-bright and dark domains in that same optically-continuous crystal are much smaller (20-80 microns).

4.3 Ti concentrations in quartz

Titanium in quartz in the barren quartz vein stockwork, all of which is CL-mottled, ranges from below the detection limit of 10 ppm up to a maximum of 99 ppm

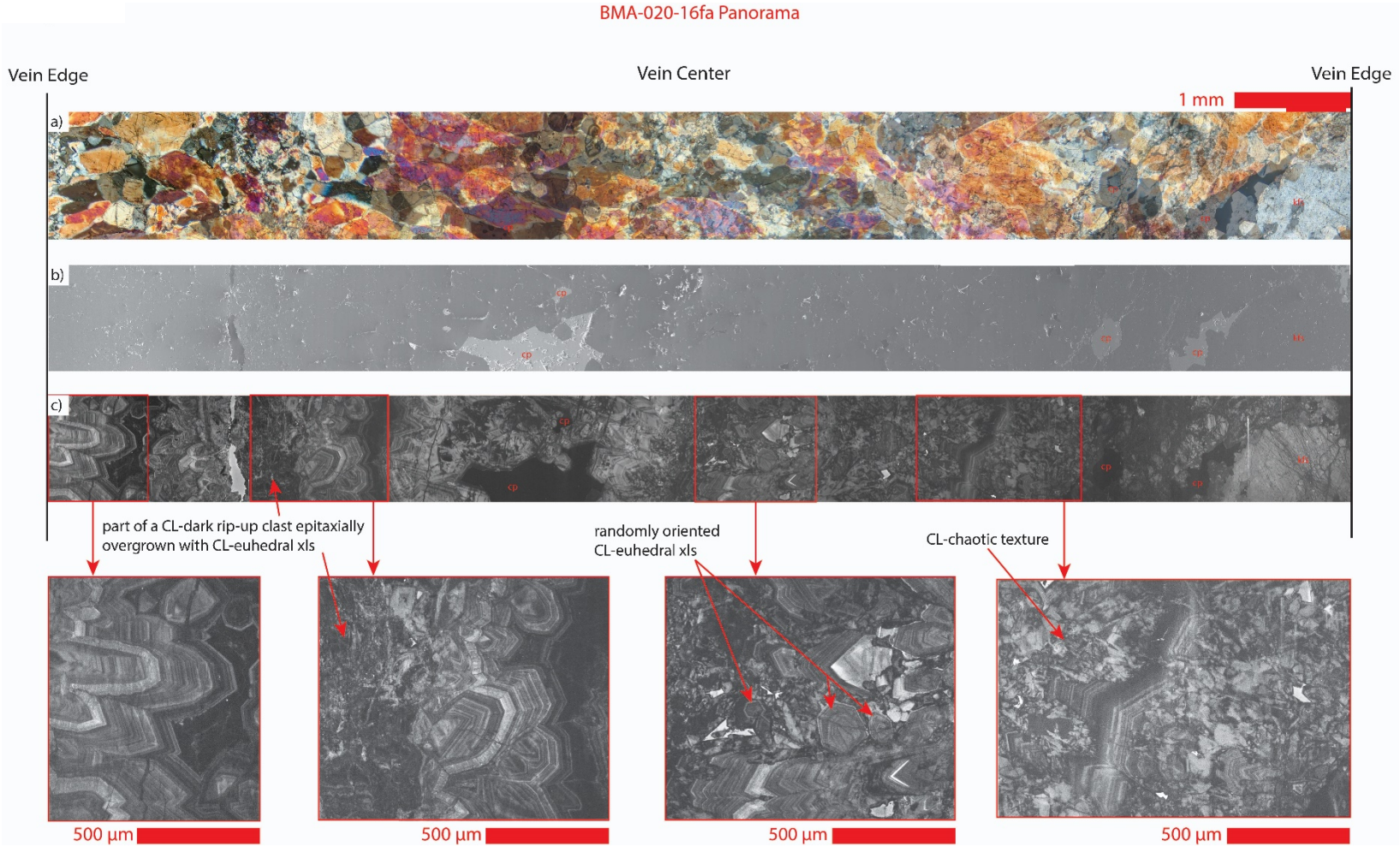

Figure 3.5 Low temperature Main Stage quartz is much more complex in CL than higher temperature pre-Main Stage quartz. A) a thick section transect of Main Stage quartz; all crystals are quartz unless labelled otherwise. That same transect was also imaged with SEM-SE (B) and SEM-CL (C).

with an average of 32 ppm Ti (n=79) and a standard deviation from the mean of 19 ppm. Analytical uncertainty on individual data points is a maximum of ±4 ppm Ti, and variation due to measurement error is dwarfed in comparison to the spread in observed Ti concentrations. Ti concentrations, errors, and sampling statistics are shown in Figure 3.6 (data available in Appendix B). All Ti measurements from the Main Stage sample BMA-020-16fa are below the detection limit of 10 ppm (n=43), which confirms the results of Rusk et al. (2008b).

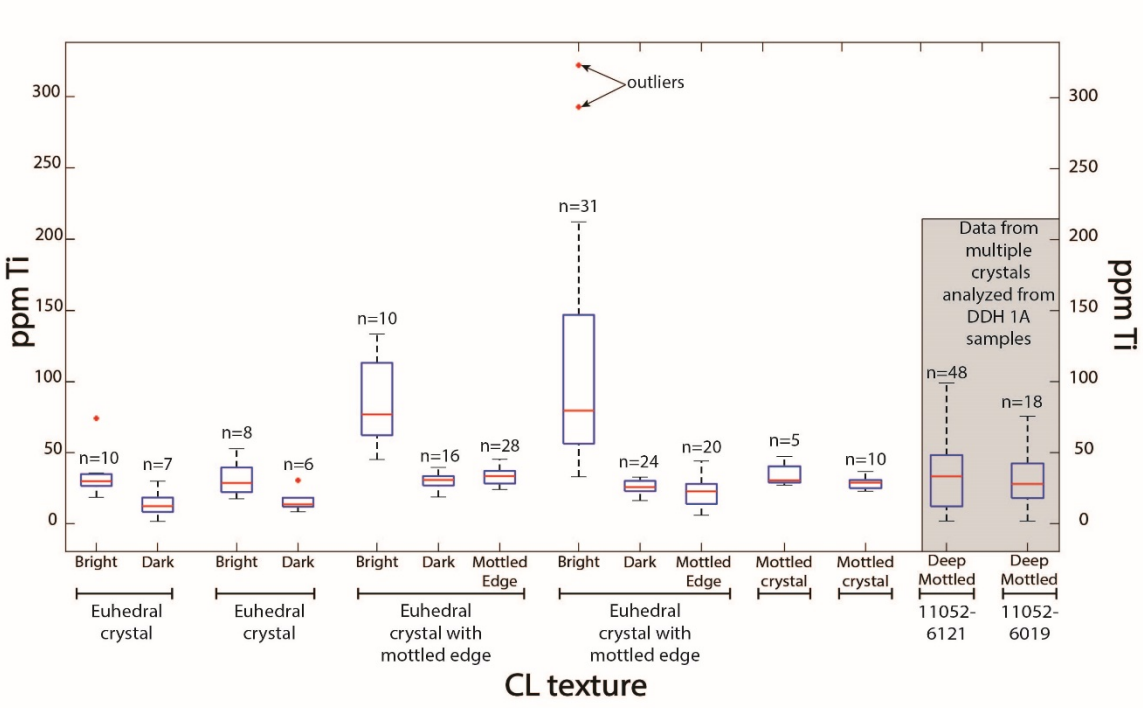

Figure 3.6 Ti measurements from a single quartz-molybdenite vein of bright and dark growth bands of CL-euhedral crystals, euhedral crystals with mottled edges, and mottled crystals. Individual crystals are demarcated by horizontal lines below the x-axis. Data within the grey box is of barren quartz from drill core that is entirely CL-mottled. Note that "bright" and "dark" are relative terms and depend on user-specified operating conditions at the time of CL image acquisition. The maximum error on individual analysis points is ±4 ppm Ti, which is insignificant compared to the range of values.

The largest range in Ti concentration was analyzed in CL-euhedral crystals of a quartz-molybdenite vein from the Continental pit (BMA-018-16fa). The Ti concentrations in the four CL-euhedral crystals (n= 132) range from 17 to 323 ppm in the bright domains with a standard deviation from the mean of 63 ppm Ti, and 16 to 40 ppm in the dark domains with a standard deviation from the mean of 8 ppm Ti. Two analyzed crystals have CL-euhedral cores that grade into CL-mottled edges that have slightly

elevated Ti concentrations compared to contiguous, entirely CL-mottled crystals. These CL-mottled crystals contain 23 to 47 ppm Ti and have an average of 31 ppm Ti with a standard deviation from the mean of 6 ppm Ti. Mottled edges of crystals with CL-euhedral cores have between 7 and 45 ppm Ti with an average of 29 ppm Ti and a standard deviation from the mean of 9 ppm Ti.

5. Interpretations

5.1 Origin of CL-mottled texture and coexistence of CL-mottled & CL-euhedral textures

The CL-euhedral quartz grains are unambiguously primary crystals precipitated from a hydrothermal solution. The origin of co-existing CL-mottled crystals is less obvious. However, the fact that many CL-mottled crystals display undulose extinction in thin section and have grain boundary forms indicative of dynamic recrystallization requires that CL-mottled quartz forms by the deformation of CL-euhedral primary textures with consequent partial to full obliteration of growth zonations. But if CL-mottled crystals are deformed CL-euhedral crystals, *how can CL-mottled crystals occur alongside undeformed CL-euhedral crystals?*

Initial quartz growth during vein formation in porphyry Cu systems follows the principle of geometrical selection (Grigor'ev, 1965; Nollet et al., 2006; Wendler et al., 2016). Because the granite fracture surface is lined by randomly oriented crystals that are not all quartz, epitaxial quartz growth is limited, and numerous randomly oriented quartz crystals grow along the host rock substrate. The majority are oriented with their c-axes, the primary growth direction, at a non-normal angle to the fracture surface, so the crystals impinge on one another, which inhibits growth. Crystals oriented with c-axes perpendicular to the fracture surface outgrow those of other orientations because their tips protrude into the fluid in the center of the fracture where the supply of silica from the fluid is fastest and growth is optimized. Only crystals growing perpendicular to the substrate continue to grow, resulting in a layer of parallel crystals. This creates cockscomb quartz textures and is typically formed from fluids that are only slightly supersaturated with quartz and undergoing either slow or mild fluctuations in growth conditions such as pressure or temperature (Fournier, 1985; Shimizu, 2014; Wendler et al. 2016).

Quartz-molybdenite and barren quartz veins are not simple monogenetic cockscomb veins, however; although vein edges are lined with cockscomb quartz, the centers of veins contain randomly oriented crystals, the great majority of which are CL-mottled. There are several ways the vein center may form randomly oriented crystals: 1) the crystals nucleated and grew *in situ*, 2) the crystals nucleated higher in the fluid column and rained downwards, or 3) the crystals were transported upwards from farther down in the fluid column. Since all the cores of veins have been recrystallized, we cannot distinguish among the three scenarios.

Shortly after veins filled, high temperature dynamic recrystallization preferentially changed the CL-euhedral quartz in vein centers to CL-mottled texture for reasons explained below. That the Ti concentration in CL-mottled crystals is the same as that in the dark bands in the adjacent CL-euhedral crystals indicates that the temperature of the strain that accompanied grain boundary migration was roughly the same as the temperature of the primary crystallization of the euhedral crystals, because recrystallization anneals quartz to its equilibrium Ti concentration. Ti diffusion through quartz is very slow (Jollands et al., 2020) but grain boundary migration induces Ti homogenization in quartz and allows it to reset to the equilibrium value at a rate that is much faster (Van der Kerkhof et al., 2004; Nachlas and Hirth, 2016).

Comb quartz lining the edges of veins does not deform because strain is more readily accommodated by quartz in the centers of veins where random grain orientations present many crystals for which there is no activation energy for basal glide, which is the most easily activated slip system. Crystals in vein centers that are not initially oriented such that basal glide readily occurs rotate in their deforming matrix until they too begin to deform plastically. Thus, strain is accommodated in the vein centers. Mottled edges of some cockscomb CL-euhedral crystals form because the lattices of adjacent crystals do not align perfectly and the grain boundary does not form in the most energetically stable orientation, so limited grain boundary migration occurs driven by free energy minimization of grain boundary geometries. Because most of the strain occurs in the centers of veins and the driving force of the lattice mismatch/grain boundary geometry between cockscomb crystals is small, recrystallization is localized, and crystal cores are unaffected.

In contrast to vein centers, the strong preferred orientation of comb quartz along the edges results in a population wherein the resolved shear stress on a given cockscomb crystal is less than the critical resolved shear stress needed to activate slip along glide planes. Grain boundaries between adjacent cockscomb crystals are not initially in an energetically stable configuration due to mismatch between adjacent crystals caused by variation in relative growth rates of individual faces as the crystals impinged on one another. Because of this, limited grain boundary migration occurs between cockscomb crystals and creates mottled edges of otherwise CL-euhedral crystals. Thus, veins have blocks of CL-euhedral crystals that are bounded along the vein edges and centers by CL-mottled recrystallized quartz.

Fracture formation is the wall rock response to stresses inflicted by fluids accumulating in the cupola. When a cupola is primed for a fluid expulsion event, there will be a localized zone around the cupola where the stress field is almost entirely dominated by cupola-imposed stresses. This cupola-adjacent zone is also the hottest and most ductile due to its proximity to the magma chamber. Far away from the bloated cupola, stress is regional, and in Butte compressive with a horizontal σ_1. Between the zone dominated by cupola-caused stresses and the zone dominated by tectonic forces is a zone where the stress is a combination of regional and cupola-caused. Stress in this zone is highly dynamic and will fluctuate as the cupola below inflates, deflates, and reinflates. Hydrofractures are initially vertical and horizontal. Fractures formed in the roof of the cupola due to the buoyant rise of the fluids therein are normal to the cupola surface. As fluid is expelled from the cupola and moves out and away into the country rock through fracture networks, the cupola forces become minimal compared to regional stresses, i.e. the directional stresses acting on the vein rotate as local stresses dissipate and regional stresses become the dominant stress regime (Figure 3.7). Thus, veins would undergo shear if they were emplaced in the zone of combined regional and local stresses as the local cupola-stresses change. This may be accompanied by collapse of the deflated cupola or subsequent rotation of the vein as a block during later fluid expulsion events.

To summarize, quartz-molybdenite veins in Butte formed by:

1. Hydrofracturing rock around the magma chamber cupola.

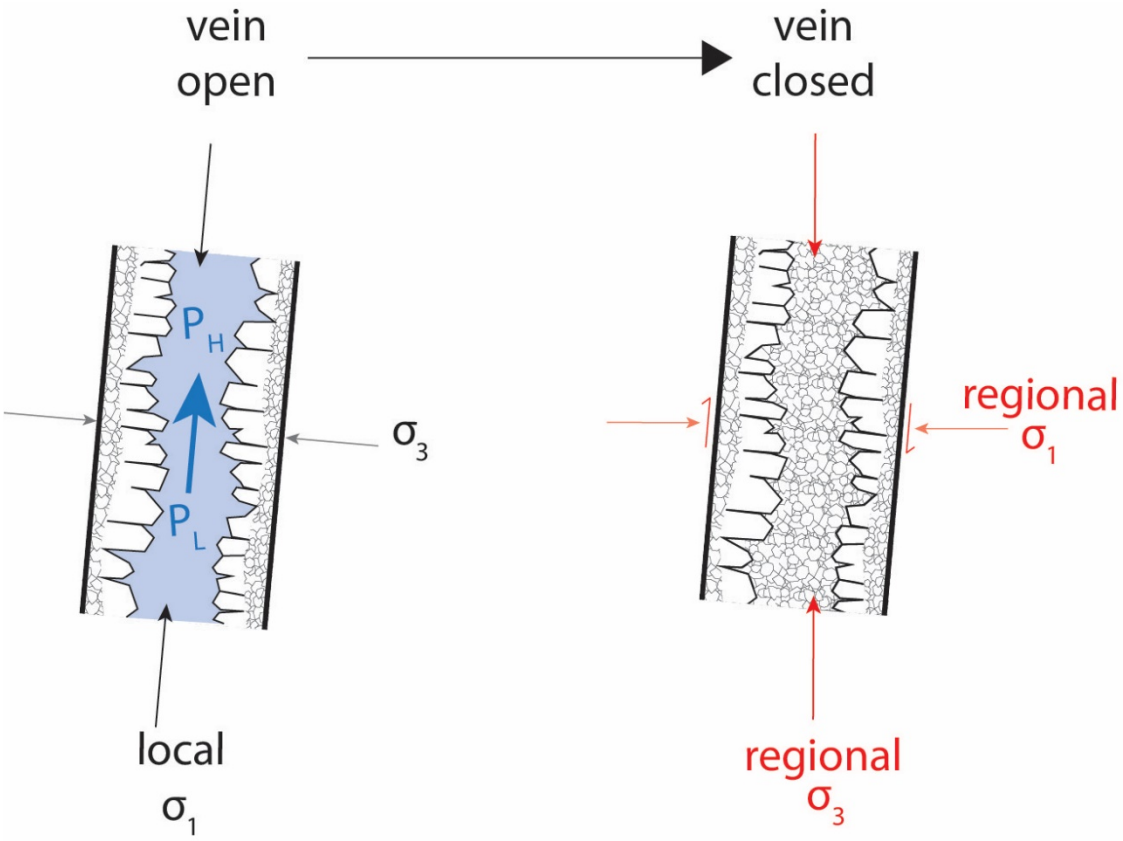

Figure 3.7 Initially when a hydrofracture forms it is in response to a non-vertical local stress regime imposed by the cupola/magma chamber and so the strikes of hydrofractures are perpendicular to the outermost edge of the cupola. As local stresses dissipate, non-vertical veins shear as regional stresses take over. Any non-normal stress results in shear strain as stress rotates. All stresses shown in this 2D diagram are for solids only; i.e. the cartoon does not include stresses in the fluid related to flow.

2. Nucleating and growing euhedral comb quartz on the fracture surfaces.
3. Euhedral crystals homogeneously nucleated, suspended, and grown in the fluid are randomly jammed or settled in the centers of veins.
4. Veins deform partially or wholly depending on proximity to cupola
    a. Barren quartz veins are deeper than quartz-molybdenite veins and so likely to spend significant amounts of time in the ductile zone around the cupola dominated by local stresses. All quartz in these veins recrystallizes to CL-mottled.
    b. Quartz-molybdenite veins are at least partially in the zone where stresses are a dynamic combination of regional and cupola-caused. This zone is not as ductile as the region immediately around the cupola and transient shear is common as the cupola-caused stresses fluctuate relative to regional stresses. After the vein has mostly solidified, randomly oriented centers of veins accommodate stress by deforming plastically, which converts CL-euhedral textures to CL-mottled textures. Strain preferentially afflicts crystals in the centers of veins, sparing layers of comb quartz at the vein edges. Randomly oriented crystals lining the fracture surface also recrystallize, leaving only the cockscomb layers intact.

Complete grain boundary migration recrystallization of barren quartz is likely due to repeated cycles of cupola collapse and compression. Because there are no constraints on the number of individual fluid expulsion events that form a given vein type, it is possible that successive expulsion events result in as many recrystallization events. Barren quartz veins, being deeper and closer to the cupola, are also more likely to brecciate during expulsion events that happen after they have formed – and so rotate as planar fragments and experience cupola-dominated stresses and regional-stresses in a variety of orientations. Such reworking would allow for the recrystallization of CL-euhedral quartz if it had been originally present. An alternative hypothesis is that barren quartz veins never formed cockscomb quartz layers and recrystallization of a vein initially comprised completely of randomly oriented crystals creates completely CL-mottled quartz veins.

5.2 CL-dark bands preserve equilibrium Ti concentration

Dark bands record roughly the same amount of Ti from one dark band to the next for a given CL-euhedral crystal, whereas Ti in bright growth bands has a much wider range of concentrations (Figure 3.6). Furthermore, Ti concentrations in dark bands are similar to Ti concentrations in nearby recrystallized CL-mottled crystals. In crystals with CL-euhedral cores and CL-mottled edges both relationships are observed, i.e. mottled edges have similar Ti to the dark bands in euhedral cores and to nearby completely mottled crystals. This suggests that the dark bands record near equilibrium growth and that the high Ti-bright bands are excursions away from equilibrium, and that recrystallization occurred near the pressure and temperature of crystal growth. Cernuschi et al. (2018) came to the same conclusion based on thermal modeling considerations of diffusion profiles between CL-bright and CL-dark growth bands. Grain boundary migration recrystallization reset Ti to its equilibrium value by way of annealing, and loss of excess Ti from the crystals during deformation, as has been shown experimentally (Nachlas and Hirth, 2015; Ashley et al., 2015; Nachlas et al., 2018) and by field investigations (Grujic et al., 2011; Haertel et al., 2013; Bestmann and Pennacchioni, 2015).

5.3 Quartz precipitation temperatures

Ti concentrations in quartz can be used to estimate temperatures using the experimentally calibrated TitaniQ geothermobarometer (Huang and Audetat, 2012). All temperature estimates reported are calculated using the Huang and Audetat (2012) calibration of the TitaniQ geothermobarometer at a lithostatic pressure of 250 MPa based on the fluid inclusion analyses of Rusk et al. (2008) and Roberts (1975). CL-mottled crystals must have deformed under lithostatic pressure. When the calculations are done at a hydrostatic pressure of 70 MPa, temperature estimates are ~ 70 °C lower. We assume the fluid is near rutile saturation because rutile is abundant in barren quartz and quartz-molybdenite veins.

Mercer and Reed (2013) analyzed Ti in quartz from Butte barren quartz and quartz-molybdenite veins. They reported that barren quartz had an average of 61 ppm Ti (n=49, standard deviation of 32 ppm Ti) and that quartz-molybdenite veins had an

average of 38 ppm Ti (n=99, standard deviation of 19 ppm Ti). We note that they did not differentiate between CL-euhedral and CL-mottled textures. These correspond to TitaniQ temperatures of 688 ℃ for 61 ppm Ti and 638 ℃ for 31 ppm Ti. Mercer and Reed (2013) also used Zr-in-rutile thermometry to estimate the temperatures of formation of barren quartz and quartz-molybdenite veins which yielded averages of 591 ℃ and 567 ℃, respectively.

Combining the Mercer and Reed (2013) dataset with ours for barren quartz veins gives an average of 48 ppm Ti and a TitaniQ temperature of 660 ℃. We note that the Mercer and Reed (2013) dataset is made up of seven barren quartz samples taken from four different drill holes, and so the heterogeneity in their data likely encompasses spatial temperature variation in a way that ours does not.

Rusk et al. (2008a) found that barren quartz/quartz-molybdenite veins contain B35 and B60 fluid inclusions and concluded, based on detailed microthermometry of fluid inclusion assemblages, that they formed between 550-650 ℃. We note that many of the inclusions analyzed in Rusk et al. (2008a) and Roberts (1975) must have been recrystallized, but because they measured assemblages and did rigorous statistical analysis their findings remain valid and must record conditions of deformation. Likewise, Field et al. (2005) used S isotopes of co-existing sulfide mineral pairs to estimate quartz-molybdenite temperatures of 500-630 ℃.

TitaniQ gives temperatures ranging from 499-907 ℃ for the quartz-molybdenite vein from the Continental Pit. The highest temperatures are estimated from CL-euhedral bright bands and are unreasonably high, indicating that the CL-bright bands must be recording Ti in excess of the equilibrium concentration. In contrast, an average Ti of 25 ppm in CL-euhedral dark bands corresponds to 600 ℃. Averages of 29 ppm Ti for mottled edges and 31 ppm Ti for mottled crystals yield respective temperatures of 612 ℃ and 619 ℃. An average of 36 ppm Ti from mottled quartz in barren quartz veins from DH1A corresponds to a temperature of 622 ℃. These temperature estimates indicate that quartz-molybdenite veins precipitated from fluids between 600 and 619 ℃. It seems unlikely that deformation would happen at a temperature higher than that of quartz precipitation, and so either the CL-dark bands of euhedral quartz are recording less Ti than the equilibrium concentration or the CL-mottled crystals are recording slightly more.

The difference is slight enough to be overshadowed by the uncertainties of the TitaniQ experimental calibration, growth rate, and analytical error. Overall, temperature estimates made using TitaniQ are in excellent agreement with other available thermometers and barren quartz/quartz molybdenite veins formed and deformed at temperatures between 600 ℃ and 622 ℃.

The maximum Ti concentration of 99 ppm in barren quartz corresponds to a near-magmatic temperature of 741 ℃ at 250 MPa, which is a reasonable upper limit temperature estimate given that some barren quartz veins have aplitic centers and contain a mixture of fluid and melt inclusions (Roberts, 1975; Rusk et al., 2008a). Some CL-mottled quartz from the same barren vein is below the detection limits of 10 ppm. This very low-Ti quartz could have formed from a fluid that was depleted in Ti, could have formed much later at lower temperature, or could have undergone more recrystallization at a lower temperature.

5.4 Main Stage vein

CL-mottled textures are conspicuously absent from Main Stage veins imaged in this contribution and by Rusk et al. (2008b). This fits with the interpretation that the CL-mottled texture forms during high temperature recrystallization of what was originally CL-euhedral quartz. The abundance of CL-chaotic texture in Main Stage veins and its conspicuous absence in pre-Main Stage veins suggests that the mechanism of its formation is a lower temperature process; the maximum temperature of formation of Main Stage veins is ~350 ℃ (Rusk et al., 2008a). It is plausible CL-chaotic texture is formed by way of extremely fast growth as sucrosic quartz crystals ripened and impinged on one another. Another possibility is that they are chalcedonic. The domains of CL-chaotic texture bear a striking resemblance to plumose quartz. Plumose quartz is found in epithermal deposits, often alongside colloform quartz. Both plumose quartz and colloform quartz are thought to form as chalcedony ripens to quartz (Sander and Black 1988; Vearncombe, 1993; Shimizu, 2014). Further work is required to understand the formation of CL-chaotic texture.

6. Implications

Preferential recrystallization of randomly oriented quartz crystals shortly after vein formation has not previously been reported in a porphyry copper setting. Porphyry copper formation entails multiple episodes of magmatic fluids hydrofracturing the cupola and moving outward to form vein systems, and ductile deformation at lithostatic pressures must dominate rock rheology at the base of the deposit. Barren quartz and quartz-molybdenite veins record those deformation events, and so quartz vein deformation is an essential process in ore genesis. Our findings show that, despite an abundance of complicating factors, Ti-in-quartz concentrations are meaningful for interpreting quartz growth and deformation histories. That the dark bands in CL-euhedral quartz record near-equilibrium growth is important for showing how to apply TitaniQ to hydrothermal quartz. Furthermore, that recrystallization occurs during vein closures at temperatures that are roughly the same as that of quartz precipitation from aqueous fluids suggests that quartz deformation may play an important role in determining duration of time intervals in between fluid expulsion events.

This contribution shows how vein quartz strain and recrystallization modify primary growth textures, including those in quartz stockworks, that are characteristic of the bottoms of porphyry Cu deposits, explains the preservation of primary growth textures, and helps define questions for further work. Many questions remain, such as: what are the time scales of deformation? What is the total magnitude of strain recorded? To what extent does low temperature recrystallization overprint and destroy high temperature recrystallization textures? How many deformation events are recorded in each vein population?

7. Bridge

Natural crystals are commonly zoned. The quartz crystals in hydrothermal veins from Butte are no exception, exhibiting numerous types of zonations that can be described as CL-cobweb, CL-splatter, CL-dark fractures, CL-sectoral, CL-euhedral (oscillatory), and CL-mottled. In the previous chapter, we showed images of CL-euhedral and CL-mottled crystals but mainly focused our attention on the origin and significance of the CL-mottled texture. In this chapter, we return to the CL-euhedral crystals and

explore whether the CL-bright and CL-dark oscillations reflect changes in temperature, pressure, fluid composition, or other factors. An important clue comes from our experimental work in Chapter II, which shows that different types of zonations can arise even at fixed temperature and pressure.

CHAPTER IV
OSCILLATORY GROWTH ZONES OF HYDROTHERMAL QUARTZ FROM THE BUTTE PORPHYRY COPPER DEPOSIT MAY FORM AT LOW SUPERSATURATIONS

This chapter contains unpublished material. The ideas presented herein were garnered from my reading of the relevant literature. Mark Reed and Jim Watkins contributed to this chapter by questioning the validity of the suggested hypotheses and by significantly editing the manuscript and figures.

1. Introduction

Quartz in veins from porphyry Cu deposits commonly have well-developed growth bands revealed by the cathodoluminescent (CL) response to Ti incorporated into the quartz lattice (Penniston-Dorland, 2001; Rusk et al., 2008a; Müller et al., 2010; Monecke et al., 2018; Cernuschi et al., 2018). Such oscillatory zonations in quartz can be either intrinsic or extrinsic. Extrinsic oscillations are caused by changes in temperature, pressure, or fluid composition. Intrinsic oscillations arise even at nearly fixed temperature, pressure, and fluid composition due to feedbacks operating at or near the mineral surface.

In this contribution, we assess whether Ti concentrations in CL-dark and CL-bright bands can reasonably be ascribed to changes in external forcings (temperature, pressure, or fluid composition), and if not, whether such banding might be characteristic of crystal growth at low supersaturations, near the so-called “dead zone,” as described in the recent crystal growth literature.

2. Extrinsic growth

2.1 Dark bands record near-equilibrium Ti concentrations

Quartz-molybdenite veins from the Butte porphyry Cu-Mo deposit contain quartz with two CL textures: CL-euhedral and CL-mottled (Figure 4.1a and 4.1b). Primary CL-euhedral quartz vein crystals (Figure 4.1a) grow inwards from randomly oriented crystals that line the vein walls. During or shortly after vein closure, randomly oriented CL-

euhedral crystals in the centers of veins recrystallize to CL-mottled quartz (Figure 4.1b) with Ti concentrations close to the equilibrium value for the pressure and temperature of deformation, as shown in Chapter III of this dissertation.. A key point is that the recrystallized quartz contains roughly the same amount of Ti as the dark growth bands of neighboring CL-euhedral quartz, suggesting that the dark bands also record the

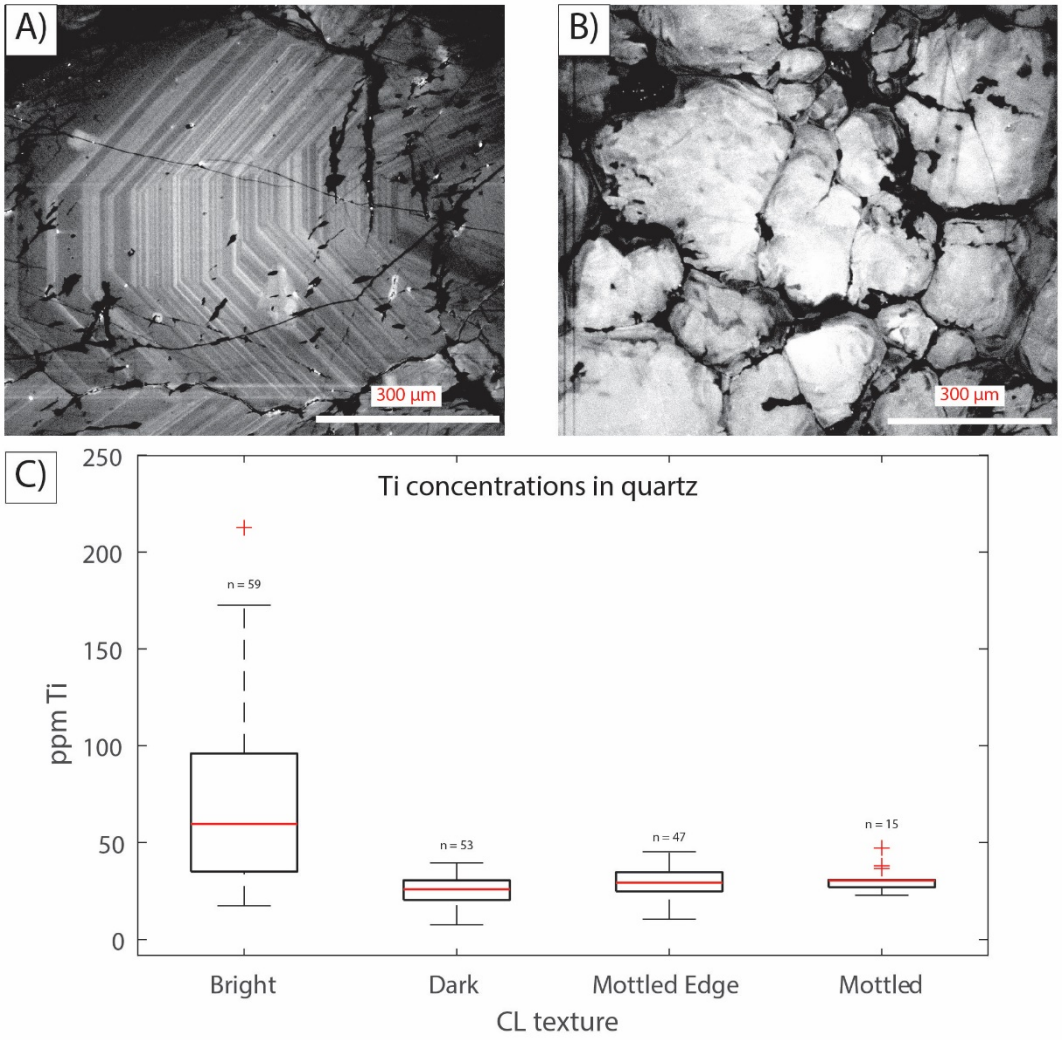

Figure 4.1 Butte vein quartz displays distinct SEM-CL textures that are caused by differences in Ti concentrations. A) CL-euhedral textures record growth from an aqueous phase. B) CL-mottled crystals form during grain boundary migration deformation of what was initially CL-euhedral quartz. C) Recrystallized mottled crystals preserve Ti concentrations that are roughly equivalent to the mottled edges of crystals with CL-euhedral cores as well as the Ti concentrations of CL-dark growth bands. Note that the data shown for each CL texture contains measurements from multiple crystals, e.g. the data plotted as CL-bright are the Ti concentrations from bright bands of multiple crystals.

temperature and pressure of quartz growth and that these conditions are similar to the conditions of deformation (Figure 4.1c).

The temperatures estimated from the Ti in dark bands agree with independent estimates. Using the Huang and Audetat (2012) calibration of the TitaniQ geothermobarometer, and assuming lithostatic pressure, 24 ppm Ti in CL-dark bands corresponds to 595 ℃ and 30 ppm in CL-mottled corresponds to 615 ℃. Note that temperatures calculated at hydrostatic pressure are only 23-30 °C less than those estimated for lithostatic pressure. For comparison, Rusk et al. (2008b) estimated that quartz-molybdenite veins formed at temperatures between 550-650 ℃ based on fluid inclusion thermometry, and Mercer and Reed (2013) used Zr-in-rutile thermometry to arrive at temperatures between 466 ℃ and 643 ℃. Mercer and Reed (2013) also estimated quartz-molybdenite vein formation with TitaniQ and reported an average concentration of 38 ppm Ti, corresponding to 637 ℃ but they did not distinguish between CL-mottled and CL-euhedral crystals in their analysis. The general agreement between different approaches, in conjunction with previous work suggesting that layers of cockscomb quartz form from fluids that are only slightly supersaturated (Fournier, 1985; Wendler et al., 2016), suggests that the dark regions of CL-euhedral crystals record near-equilibrium Ti.

2.2 Bright bands are not extrinsic

The CL-bright bands have higher and more variable Ti concentrations than do CL-dark bands (Figure 4.1c). The average value of 80 ppm Ti in bright bands corresponds to 717 ℃, which is unrealistically high for quartz precipitating from a hydrothermal fluid, suggesting that oscillations in temperature are not responsible for the oscillations in Ti concentrations in Butte pre-Main Stage quartz. Furthermore, if the growth bands were the result of temperature changes, we would expect to see evidence of cooling after each thermal rejuvenation event in the form of progressively lower Ti within each bright band, but we do not. These considerations argue against the hypothesis that growth bands in CL-euhedral crystals form primarily in response to temperature fluctuations.

The oscillations cannot be attributed to a thermodynamic response to fluctuations in pressure either, because a lithostatic-to-hydrostatic pressure difference (250 MPa – 70 MPa) yields a relatively small change of Ti solubility in quartz (e.g. 25 ppm Ti at 250 MPa to 60 ppm Ti at 70 MPa).

If the oscillations reflect extrinsic control and are not caused by pressure or temperature fluctuations, then could they be caused by fluctuations in the activity of titania in the fluid? At a constant pressure of 1.8 kbar and temperature of 600°C, the equilibrium Ti concentration in the quartz lattice could range from 34 ppm Ti at a_{TiO2} = 0.1 to 332 ppm at a_{TiO2} =1 (Huang and Audetat, 2012), which spans the observed range in the data. However, the veins contain abundant rutile suggesting quartz growth from a fluid with a_{TiO2} equal to or greater than 1. Nevertheless, it is conceivable that the fluid may have undergone oscillations in the degree of rutile undersaturation. Departures from rutile saturation could be driven by growth and dissolution of other minerals such as wall rock biotite, hornblende and rutile that contain Ti, or dilution by fluid mixing. However, if cycles of Ti enrichment and depletion in the fluid were caused by mineral growth or dissolution at greater depths, then the expected quartz CL pattern would be smooth gradations between CL-dark and CL-bright, not the sharp transitions that we observe.

3. Intrinsic growth

3.1 Growth rate kinetic effects at the macroscale

Fast growth can lead to higher-than-equilibrium impurity concentrations in the growing crystal (Huang and Audetat, 2012). The experimental results of Huang and Audetat (2012) suggest that Ti concentrations in quartz can increase by more than a factor of two across an order of magnitude increase in growth rate. Hydrothermal quartz growth experiments of Acosta et al. (2020; Chapter II of this dissertation) yielded a wide range of Ti concentrations which are at least partly caused by variations in quartz growth rate and/or supersaturation (Ω_{quartz} >1). The link between the degree of quartz supersaturation, $\Omega_{quartz,}$ and growth rate is not well established but experiments may have spanned a Ω_{quartz} range of 1-2.

Isothermal decompression can lead to quartz nucleation and growth. If an initially quartz-saturated fluid at 600 °C and lithostatic pressure of 250 MPa were to undergo

decompression to hydrostatic pressure of 70 MPa, the degree of supersaturation would increase from unity to 3.6, as estimated with SOLVEQ (Reed et al., 2016). This is a relatively high degree of supersaturation that would likely result in rapid nucleation and growth of many quartz crystals, creating sucrosic textures that are not observed. Smaller pressure oscillations, however, could lead to smaller oscillations in supersaturation and growth rate, which in turn, could give rise to the banding that is observed. The positive

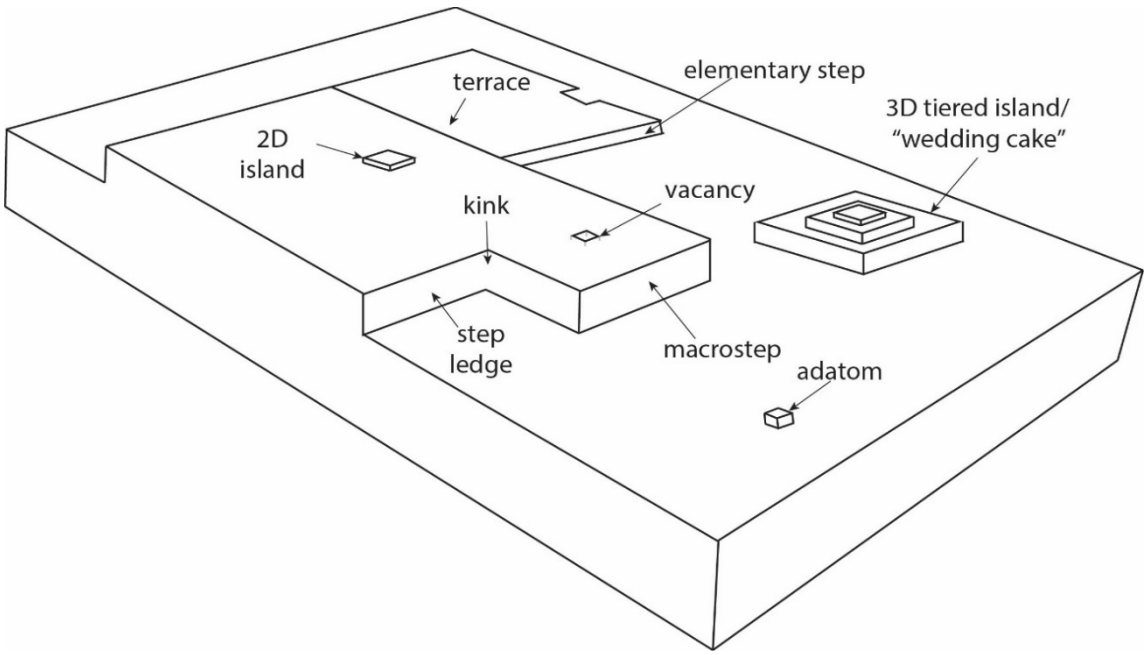

Figure 4.2 Types of structures found on crystal growth surfaces according to conventional Terrace Step Kink theory. The energy of an atom's position on a crystal face is described by its immediate bonding to neighboring atoms. For a simplified cubic lattice, atoms are approximated as cubes and bonding can occur on any face of the cube. Sites and structures are therefore categorized by the coordination number of the six "nearest neighbors". Neighboring atoms may coordinate with a central atom by sharing faces (nearest neighbors), edges (2^{nd} nearest neighbors) or corners (3^{rd} nearest neighbors). The less bound an atom is to the surface, the more readily it can desorb and diffuse around; the more bound an atom is the more static it will be. Likewise, the probability of atoms sorbing to the surface or being incorporated into the bulk crystal structure is a direct function of the topography of the surface as defined by the abundance and distribution of features shown in this diagram.

correlation between growth rate and Ti uptake is empirical, and in the discussion that follows, we explore some of the possible underlying mechanisms for this correlation.

3.2 Growth rate kinetic effects at the microscale

Processes that control surface growth of minerals and the effects of impurities on growth kinetics are thoroughly addressed in the literature (Volmer, 1922; Kossel, 1927;

Stranski, 1928; Frank, 1949; Burton et al., 1951). Here we review a few concepts and terms needed for examination of Ti zoning in quartz. Fundamentally, structures on a growth surface are defined by how readily new atoms are attached to them (Figure 4.2). A surface is categorized as rough or smooth depending on the density of attachment sites; rough surfaces consist of many kink sites and smooth surfaces consist mostly of atomically flat terraces. Terraces grow laterally as atoms attach to their edges, which are called steps.

Newly nucleated growth layers form islands on the pre-existing growth substrates; these islands then advance either laterally to form terraces or, if lateral advance is blocked by the adsorption of impurity ions to attachment sites defining the edges of islands, then they grow vertically as smaller islands nucleate on top, forming tiered wedding cake structures. Layer-by-layer crystal growth happens as steps advance across a growth surface. Microsteps are equal in height to the unit cell of the crystal in question. Macrosteps form as microsteps coalesce. Macrosteps have heights that are an integer multiple of the unit cell. Impurity ions can collect at steps and inhibit or prohibit their movement – a phenomenon known as step pinning.

Striations form on crystal growth surfaces even when pressure, temperature and fluid composition are constant owing to atomic-scale processes at the crystal growth

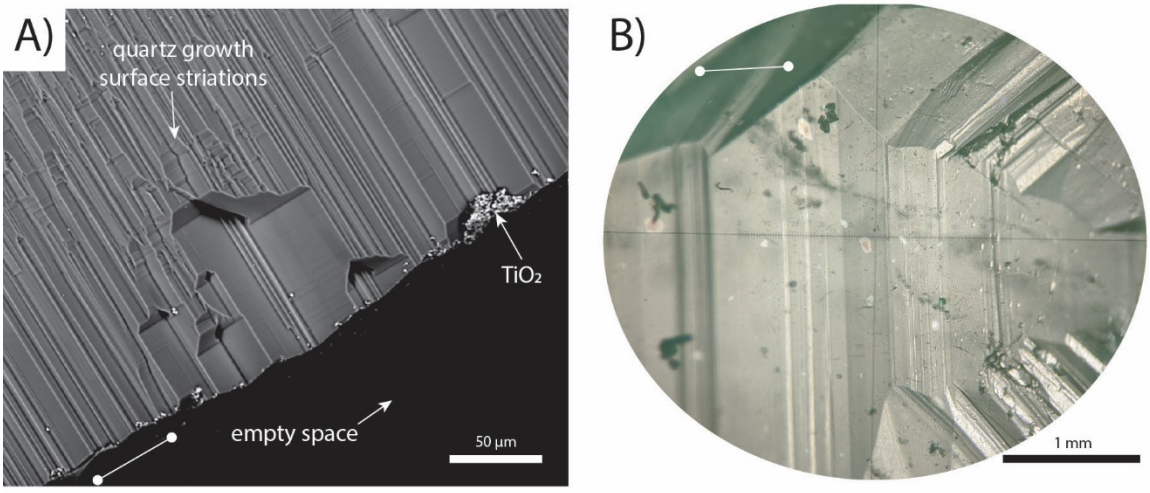

Figure 4.3 Quartz macrosteps are a common feature of hydrothermal quartz and can be seen at many scales. A) an SEM-BSE image showing well-developed parallel striations on the m-face of an experimentally synthesized quartz crystal from Chapter II of this dissertation. Brighter microparticles are TiO_2 crystals resting on the surface of the crystal. B) a reflected light image of growth striations on a natural hydrothermal quartz crystal. Ball and chain symbols show the direction of the c-axis.

surface and are common in quartz - so much so that they can commonly be seen at low magnification on the prism faces (Figure 4.3). Joshi et al. (1968) used optical images of synthetically grown quartz surfaces and showed that macroscopic striations are the edges, or steps, of growth layers/terraces that form via two-dimensional nucleation and growth.

As the crystal grows, rejected impurities concentrate at the interface until they diffuse away. Those impurities may affect the crystal growth process by changing the structure of the liquid near the interface, adsorbing and blocking attachment of stoichiometric constituents, and altering the roughness and net charge of the interface.

Changes in fluid structure at the solid-liquid interface occur as a result of ion sorption to surfaces (Björneholm et al., 2016; DelloStritto et al., 2016; Pfeiffer-Laplaud and Gaigeot, 2016; Quezada et al., 2017; Lyu et al., 2019; Tuladhar et al., 2020) and influence crystal growth (Davey, 1976; van Rosmalen and Bennema, 1990; Sangwal, 1993; Kubota and Mullin, 1995; Darmali et al., 2019; Lopez Ortiz et al., 2019). Ions that are rejected from the crystal structure sorb and desorb to the surface and their solvation spheres change near the surface relative to the ambient fluid, where the bonding environment is more homogeneous. Fluid structure and solvation energy influence diffusion not only of impurity elements, but also the major elements in the mineral.

Crystal growth at low supersaturation may be quickened by the catalytic effect of certain impurities at low impurity concentration that apparently lower the activation energy required for desolvation (Piana et al., 2007; Aquilano and Abbona, 2010). Although the catalytic effect is a well-known phenomenon in crystal growth, it has not yet been documented for quartz.

Quartz growth can be slowed where impurities bond to attachment sites, preventing the attachment of Si-O-Si units, thereby causing growth to slow and continue in spurts (Miura and Tsukamoto, 2013; Miura, 2020). Impurity induced growth rate retardation is especially pronounced in the ‘dead zone’ of crystal growth – a region of low supersaturation where impurities ‘poison’ a growth surface as originally described by Cabrera et al. (1958). Poisoning occurs where elementary steps of unit step height slowly advance across a face causing excluded impurities to collect at step edges, eventually forming barricades and ‘pinning’ step movement. This results in step meandering and bunching; wherein individual steps coalesce and form macrosteps. As the concentration

of impurities at macrostep and elementary step edges increase, step movement is halted altogether, creating the dead zone. While a crystal is in the dead zone, supersaturation can increase and eventually cause macrosteps to become mobile again and overtake the pinned edges.

The mechanism by which macrosteps overtake microsteps is currently unknown (Sleutel et al., 2018), as is the reason that macrosteps are mobile while microsteps remain paralyzed (Lutsko et al., 2016). In any case, the pinning of microsteps and the development of macrosteps increases the roughness of a surface because it decreases the nucleation barrier of 2D islands and allows islands to grow vertically as lateral growth is inhibited. As macrosteps advance, they incorporate the impurities that had poisoned the growth surface at concentrations that can be tens of times larger than the bulk equilibrium partitioning value (van der Eerden and Müller-Krumbhaar, 1986), and so a quartz growth layer formed by macrostep movement in the presence of Ti impurities will be CL-brighter than the equilibrium growth layer beneath it. The surface of a completed macrostep advancement is thus smooth and relatively free of impurities, a phenomenon known as surface cleansing.

4. Formation of CL-bright bands

4.1 A working hypothesis for Ti enrichment in CL-bright bands

The surface phenomena summarized above could underlie the non-equilibrium uptake of Ti in CL-euhedral bright bands. If, as we have argued, CL-dark bands preserve near-equilibrium growth and CL-bright bands are intrinsic growth zones with excess Ti, then there must be a mechanism for the incorporation of Ti in excess of the equilibrium values. Adopting several ideas from the recent crystal growth literature (cf. Kubota and Mullin, 1995; Miura and Tsukamoto, 2013; Sleutel et al., 2018), we speculate that cycles of crystal poisoning in dead zones and accompanying changes in interfacial structure could be responsible for the formation of CL-bright bands as the following sequence of events repeats itself (Figure 4.4):

1. Near-saturation quartz growth at a smooth interface forms CL-dark bands of arbitrary thickness depending on the duration over which the microsteps are in a regime of slow advancement across the growth surface. Equilibrium growth

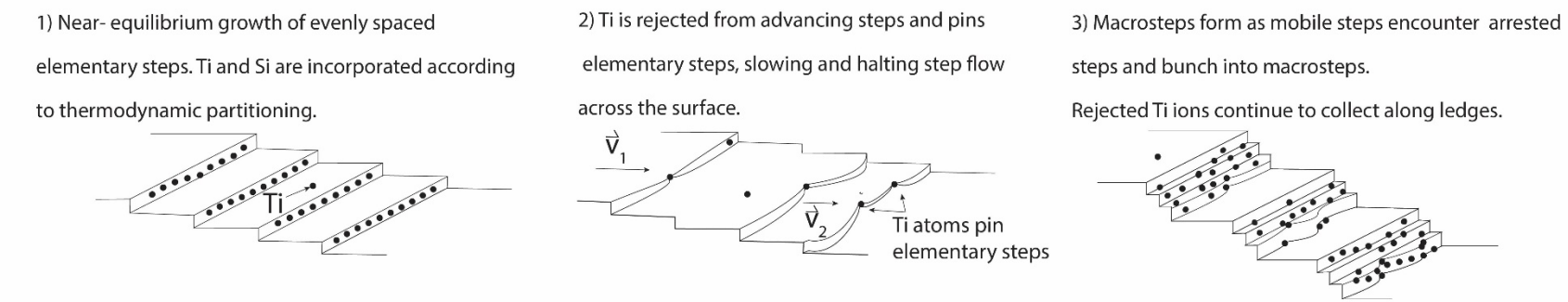

Figure 4.4 Proposed sequence of events for CL-bright band formation. The interplay between macro- and micro-step formation and movement and impurity poisoning is the likely physical mechanism for the incorporation of Ti greater than the equilibrium value into quartz growth surfaces. Although the black spheres are simply labeled 'Ti', they are in reality partially solvated complexes of Ti. The exact complex present is a function of the structure of water at the interface.

layers will reject Ti from the crystal according to thermodynamic partitioning and the rejected atoms sorb to the edges of the growth steps.

2. Rejected Ti collects at step edges, eventually forming a barrier to microstep movement; the Ti ions adsorbed to microsteps that prevent microstep movement are referred to as 'pinning Ti'. Microsteps bunch and coalesce into macrosteps. Macrosteps are more mobile than microsteps and can penetrate impurity barricades to some extent but are also ultimately arrested; rejected Ti poisons quartz growth.
    a. If macrosteps reject pinning Ti as microsteps are overtaken and incorporated into the macrostep, then they will be CL-dark, and the growth layer will consist of nanoscopic domains of CL-dark and CL-bright regions.
    b. However, if the macrosteps incorporate pinning Ti as they advance over arrested microsteps, then the layer formed by the macrostep will not be CL-dark but of intermediate or bright CL intensity. The latter scenario of macrosteps incorporating microstep-pinning-impurities has been modelled for Kossel crystals (idealized simple cubic crystals) by Sleutel et al. (2018), where they also showed that impurity-rich growth bands can form by a similar process to the one outlined here.
3. Because growth is inhibited by the accumulated Ti, a kinetic roughening transition ensues as island growth preferentially occurs vertically because nucleation of islands on top of islands is more energetically favorable than the lateral spread and coalescence of preexisting islands. This serves to increase the number of kink sites and edges and enhance adhesive attachment of Si and Ti atoms.
4. CL-bright growth zones form when a critical local supersaturation is reached and the macrosteps overtake microsteps and islands, as well as the impurity barricades fringing the microsteps. Macrosteps incorporate the smaller structures and impurities into the crystal lattice. The mechanism whereby arrested macrosteps begin to advance is currently unknown but likely related to surface roughening and increased supersaturation. Another possibility is that very small pressure

perturbations —much smaller than the lithostatic-to-hydrostatic range—caused by microcrack formation, compaction of minerals in the vein, or small spurts of vertical movement, oscillate the supersaturation and occasionally cause macrosteps to become mobile.

5. Macrosteps leave behind them a smooth surface devoid of Ti allowing near-equilibrium growth to resume and creating a CL-dark growth layer of arbitrary thickness.
6. Repeat until the system is perturbed away from a near-equilibrium growth regime.

An important question is: what is the critical height of macrosteps before they advance? Based on outputs from recent kinetic Monte Carlo simulations of growth of an idealized cubic crystal (a Kossel crystal) with impurity poisoning (Lutsko et al., 2016; Sleutel et al., 2018), the macrosteps can be on the order of tens to hundreds of elementary "building blocks" in height before advancing. In terms of absolute height, this corresponds to tens to perhaps up to 100 nm, which is more than an order of magnitude thinner than the thinnest resolvable CL-bright band. This is consistent with the lack of lateral variations in CL within the CL-bright and CL-dark bands. If the mechanism outlined above is correct and the macrosteps are CL-dark, the CL-bright bands with thickness on the order of 1-10 μm could be produced in one of three ways (Figure 4.5). The first possibility is that as the macrosteps advance laterally, new macrosteps can form on the existing ones fast enough for the CL-bright bands to continue to grow beyond the thickness of the critical macrostep height (Figure 4.5a). Alternatively, the critical macrostep height constitutes the maximum thickness of an episode of CL-bright growth and the CL-bright bands that we observe are actually a composite of numerous cycles of CL-bright to CL-dark that are not resolvable by SEM-CL methods (Figure 4.5b). That is to say that a given 1-10 μm CL bright band is actually a composite of CL-dark and CL-bright domains on the order of 10's to 100's of nanometers in size and the imaged CL-bright band has an intermediate intensity that is the composite of dark and bright domains. If, however, macrosteps incorporate pinning Ti as they advance (Sleutel et al., 2018), then they would themselves be CL-bright and the growth layers would lack nano-domains of CL-dark growth.

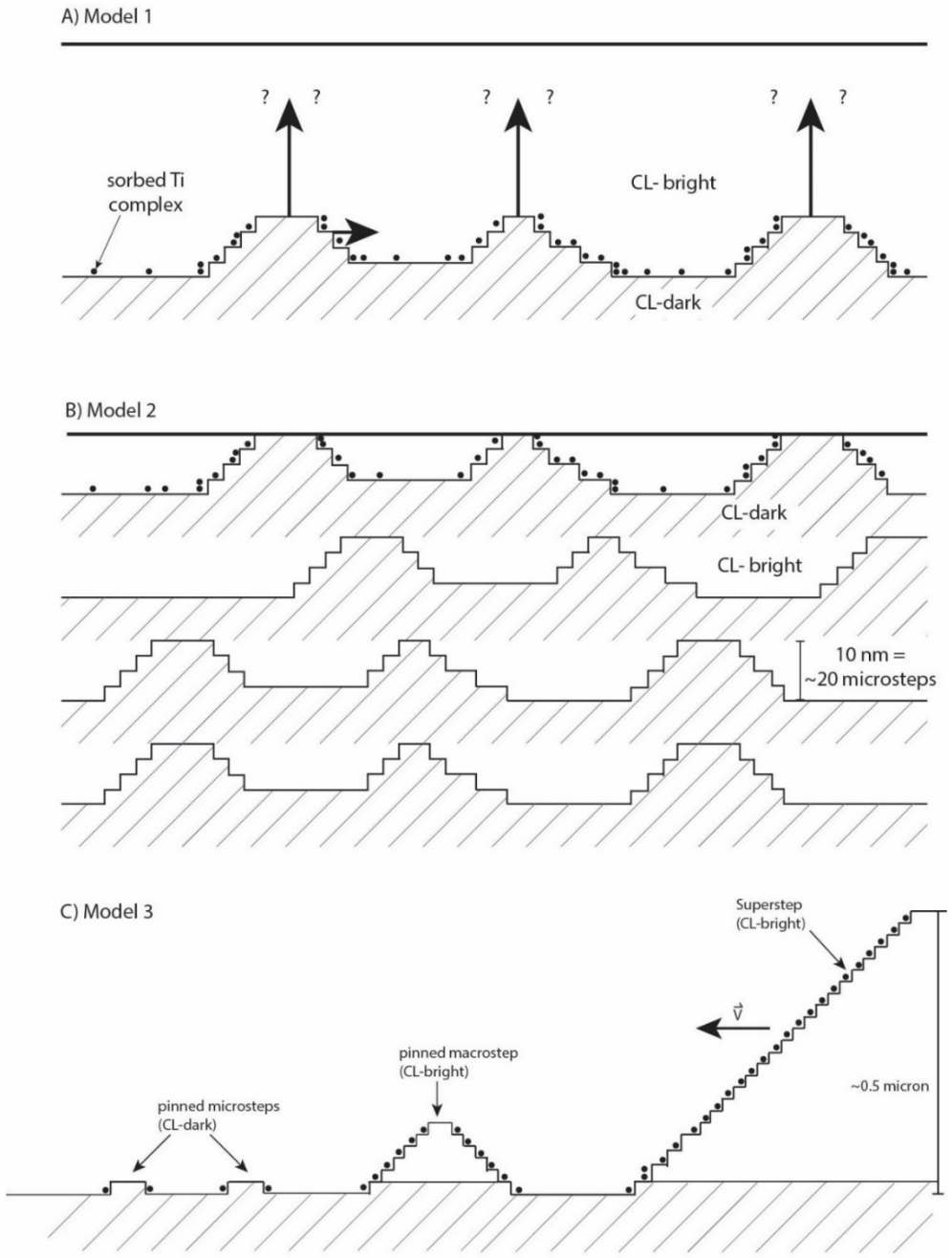

Figure 4.5 Hypothesized scenarios for the formation of large (10's of microns thick) CL-bright bands. A) after arrested macrosteps rapidly become mobile, vertical growth continues either as new steps nucleate on top of existing ones or as a rough surface grows outward via rapid ion attachment (adhesive growth regime). B) alternatively, it is possible that what appears to be a homogeneous CL-bright band is actually comprised of nano-domains of CL-dark and CL-bright zones, and the spatial resolution of CL detectors is too coarse to resolve such small heterogeneities. C) arrested CL-bright supersteps with heights that are comparable to CL-bright band thickness form by way of stacked CL-bright macrosteps and create a single CL-bright layer when they become rapidly mobile and recover.

If quartz macrosteps or supersteps (i.e. if the large striations observed on quartz growth surfaces are supersteps, as implied by the findings of Joshi et al., 1968) incorporate pinning Ti ion as they overtake them (as implied by the Monte Carlo simulations of Sleutel et al. (2018) and experimental observations of Thomas et al. (2004)), then they would not be CL-dark, but rather, would have Ti greater than the equilibrium concentration and be CL-brighter. If this is the case, formation of CL-bright growth zones that are 10's of microns tall and homogeneously CL-bright without changing pressure, temperature, or fluid composition could occur via the sequence outlined above but with supersteps forming after macrosteps and rapid superstep movement forming coherent Ti-enriched growth layers (Figure 4.5c).

4.2 Superstep heights can be commensurate with CL-bright band thicknesses

Macrostep heights are thought to be on the order of dozens or hundreds of unit step heights (Sleutel et al., 2018). Although there is a theoretical minimum to the height of a microstep, there is no theoretical cap on the maximum height of a macrostep; Joshi et al. (1968) observed quartz steps that were readily seen with an optical microscopic at low magnification and many other crystal systems are experimentally observed to have macrosteps much larger than 10's of nanometers (J. Lutsko, pers. comm.). Thomas et al. (2004) documented "supersteps" on growing potassium dihydrate phosphate (KDP) crystals, which behaved in the manner described for macrosteps above, but which are hundreds to thousands of times the height of elementary steps and were observed to be as tall as 500 nm. They found that once these supersteps formed there was an increase in growth rate that was independent of any change in supersaturation. Thomas et al. (2004) also noted a positive correlation between the height of supersteps and the rate at which they advanced: the larger the superstep, the faster it moved across the surface.

4.3 Species present and the nature of fluids

In this discussion we have thus far neglected fluid composition and the species that must be involved in crystal growth, poisoning, and recovery. As explained by Covert and Hore (2016); Besford et al., (2020), and references therein, the structure of the "boundary layer" at the quartz-water interface is poorly constrained but very different

from the bulk solution. Interfaces differ from bulk solution in that water and other molecules are oriented (Khatib et al., 2016; Ishikawa and Tsuchiya, 2017). At the interface viscosity, hydrogen bonding/pH, dielectricity, and electric double layers contribute to a unique solvation environment (e.g. Zhu and Granick, 2001; Parashar et al., 2018; Li et al., 2020) that is challenging to study due to the length and time scales over which it changes. Species present in the bulk solution may not be active at the interface, and vice versa. Silicon complexes with the quartz surface as silanols and titanium is likely adsorbed as a partially solvated molecule.

Regardless of the specifics, the universality of dead zone systematics with respect to crystals precipitated from aqueous solutions at low supersaturations suggests that the particular nature of molecules at the crystal surface is secondary to their existence. That is to say that the molecular form of Ti that pins steps in the dead zone is unknown and is likely irrelevant to whether impurity poisoning occurs. However, it is likely to be important for understanding the details of step pinning and recovery. For example, the nature of sorbed molecules will likely have an effect on the following : 1) step meandering, bunching, and coalescence, 2) step pinning (i.e. how much sorbed Ti is required to pin a step), and 3) step recovery dynamics. But knowing these details does not affect the larger scale assessment of how Ti poisoning may affect growth of CL-euhedral crystals.

5. Implications

The suggestion that CL-bright bands can form at low supersaturations without major pressure or temperature fluctuations does not mean that growth bands due to pressure or temperature fluctuations do not occur. On the contrary, such fluctuations are likely common. CL-bright growth bands that form via impurity poisoning and step recovery are likely superimposed on and mixed in with growth bands that are caused by pressure or temperature changes. Each process could be described as a disequilibrium "growth rate" effect. For example, a rapid increase in growth rate due to a pressure decrease could create a high-Ti growth zone. However, since the magnitude of Ti incorporated into quartz because of a pressure or temperature change is comparable, it is not obviously clear how to differentiate them from disequilibrium growth bands formed

by Ti poisoning. We have argued above that the CL-bright growth bands do not record near-equilibrium growth at variable pressure and temperature conditions, but we acknowledge that a change in pressure, fluid composition, or temperature could create disequilibrium growth conditions responsible for the observed CL-bright growth bands. It is, however, difficult to reconcile such large changes in growth conditions with the observations that successive CL-dark bands in a given crystal record the same amount of Ti and that the majority of CL-bright bands have sharp boundaries. It is likely that the commonly observed, but far less abundant, CL-bright bands with gradational boundaries in hydrothermal quartz may reflect changes in pressure or temperature.

6. Summary

In CL-euhedral quartz, dark bands record near-equilibrium Ti concentrations and bright bands have Ti concentrations exceeding those at equilibrium. Previous work has linked excess Ti in quartz to higher growth rates, but no mechanism has been proposed to explain this relationship (Huang and Audetat, 2012). We reviewed the recent crystal growth literature and speculate that variations in growth rate can occur at low supersaturation due to macrostep recovery after impurity poisoning or by many repeated cycles of step formation, impurity pinning, and step recovery. The process outlined above of near-equilibrium growth interrupted by Ti-induced step pinning, step bunching and the formation of macrosteps, and macrostep movement incorporating high concentrations of Ti, is our attempt to link growth rate kinetic effects to molecular mechanisms and should be regarded as a working hypothesis.

CHAPTER V
CONCLUSION

In this dissertation, I used a combination of experiments, analysis of natural samples, and numerical modeling to investigate how Ti uptake into hydrothermal quartz can be used as a tracer of geologic processes.

The experimental study of Chapter II is unusual in that we conducted many quartz growth experiments at a single pressure and temperature while varying the capsule design. This contrasts with the more conventional approach of choosing a capsule design and varying temperature and pressure. This detailed analysis of the influence of initial conditions in experiments led to the discovery that a trace component (TiO_2) in the fluid phase can have a strong impact on the crystallization kinetics of the major component (SiO_2). Furthermore, since trace element uptake into crystals can depend on crystallization kinetics, the experiments yielded a wide range of Ti-in-quartz values. The wide range was a clear indication that equilibrium was not established, and we were confronted with the challenge of developing a quantitative explanation for such variable Ti concentrations in quartz. Within the framework we developed, we revisited previous experimental data and put forward a set of possible explanations for why different experimental studies using different capsule designs have gotten different results. Our explanation requires that the fastest-grown quartz crystals have dissolved TiO_2 in excess of the rutile saturation value without having exsolved rutile. Additionally, we suggested that our crystals, which are zoned in Ti, are closer to equilibrium than crystals that were reported to have homogeneous trace element concentrations. It has been argued that homogeneity is an indicator of equilibrium but our model outputs along with experimental results in other systems show that homogeneous trace element concentrations can arise in fast-grown crystals under far-from-equilibrium conditions. Future work can build on Chapter II by: (1) mimicking natural systems such as a magma chamber by growing quartz more slowly at high pressure (>10 kbar) perhaps using another component in the capsule to buffer SiO_2 activity at a lower value, (2) growing quartz from silicate liquids using anatase and rutile in the starting materials, and (3)

following the developments in the molecular-scale simulation literature on crystal growth and impurity uptake.

Chapter III involved a detailed analysis of a small set of judiciously selected natural samples from an otherwise well-characterized locality. This is one of the first studies to undertake micron-scale direct correlation of petrographic textures and microstructures with CL imaging and microprobe analysis. Petrography is one of the oldest and most useful tools for a geologist, but the advent of CL revealed that what appears to be a simple quartz crystal under the optical microscope can have intricate and complex CL textures recording growth conditions, dissolution events, fracturing and annealing by later fluids, and deformation histories. A technical challenge of Chapter III was to correlate CL images with petrographic images and detailed microprobe work that distinguished between individual, 5-10 μm thick bands of CL-euhedral crystals. The recognition of high temperature quartz recrystallization microstructures in the centers of veins combined with the observation that almost all preserved CL-euhedral crystals are vestigial cockscomb quartz layers allowed for me to not only develop an explanation for CL-mottled textures, but also their coexistence with CL-euhedral crystals. By identifying the preferential high temperature deformation of randomly oriented crystals, I was able to establish that the change in stresses caused by the transition from local, cupola-dominant regime to regional regime can result in enough strain to modify the textures and chemistry of the rock. The interpretation that CL-dark bands of CL-euhedral crystals record near-equilibrium growth, while CL-bright bands do not, set the stage for the content of Chapter IV. In completing this project, I developed an invaluable understanding of porphyry Cu deposits in general and Butte in particular. Further work based on Chapter III could take many shapes: if plastic deformation of quartz happens shortly after vein closure, how does it interplay with the multitude of fluid buildup and expulsion events that form porphyry Cu deposits? What are the time scales of deformation? What are the magnitudes of stresses recorded in the strained rocks and why don't strong foliations develop?

Chapter IV was motivated by the results from Chapters II and III and constitutes a synthesis of pre-existing and widely accepted crystal growth theory applied to hydrothermal quartz. In Chapter II, we showed that we could grow quartz with complex

zonations at a single temperature and pressure. We also speculated that hydrothermal quartz might obey the same empirical relationships that have been documented for trace-element-doped KDP crystals, whereby at low degrees of supersaturation the crystals are zoned and have many fluid inclusions but at high supersaturation are homogeneous and relatively defect-free. In Chapter III, we showed images of oscillatory-zoned natural quartz and established that the bright-CL bands have Ti in excess of the equilibrium value. This raised the question of what process(es) could be responsible for the oscillatory behavior? Although the field of crystal growth is obviously relevant to geology, some of the developments in crystallography, especially as it pertains to industrial applications, seem to have been overlooked by earth scientists. For Chapter IV, I surveyed the crystal growth literature for ideas and results that might be relevant to the findings within Chapters II and III. I familiarized myself with the descriptors of crystal surfaces at the atomic scale and learned that there are known feedbacks between impurity uptake and crystal growth kinetics that can lead to: (1) oscillatory impurity uptake at fixed temperature and pressure, and (2) homogeneous crystals with high impurity content through the advancement of macrosteps or supersteps. It remains an open question, however, whether the systems that have been studied are good analogs for hydrothermal quartz. Future work could consist of an atomic force microscope (AFM) investigation of quartz step behavior in the presence of impurities. Any experimental study involving crystals grown at known supersaturations and growth rates with element mapping would also be informative.

APPENDIX A
CHAPTER II SUPPORTING MATERIALS

Table A1. Overview of data from literature used in Figure 2.1 of main text

Type	Description	Pressure (kbar)	notes	T (°C) (non-TitaniQ)	notes	a_{TiO2}	notes	T(°C) TH10	T(°C) HA12	
Volcanic	Oruanui	1-2 (**1.5**)	Qtz melt inclusions and Al-in-hb[10]	770 ± 30	Fe-Ti-oxides and hbl rim thermometry[10]	0.44-0.75	Fe-Ti oxide and glass comps	573-626[10]	717-785[10]	Uncertainty bars based on range in a_{TiO2} at fixed ppm Ti and P
	Early Bishop Tuff	1-3 (**2**)	Qtz melt inclusions[10]	725 ± 30	Fe-Ti-oxides[10]	0.5-0.66	Fe-Ti-oxide comps	548-572[10]	692-724[10]	
	Late Bishop Tuff	1-3 (**2**)	Qtz melt inclusions[10]	800 ± 30	Fe-Ti-oxides[10]	0.5-0.66	Fe-Ti-oxide comps	613-642[10]	766-814[10]	
Plutonic	Tuolomne Granodiorite	1.6-2.4 (**2.0**)	Al-in-hbl[1]	>650	Accepted solidus	0.5-0.6	Presence of titanite	488-544[1]	617-688[1]	Uncertainty bars based on range in ppm Ti at fixed P and a_{TiO2}
	Butte Granite	2-**2.5**	Al-in hbl[4]	700-800	fluid inclusions[8]	0.5	Subsolidus exsolution of rutile in qtz	596-669[5]	760-842[5]	
				740-760	X_{Mg}-Ti-in-bio thermometry[5]					
	Porphyry dikes in Butte Granite	0.7-**2.5**	hydrostatic to lithostatic[5]	-	only Ti in qtz	0.5	Subsolidus exsolution of rutile in qtz	562-578[5]	716-747[5]	
Magmatic-Hydrothermal Transition	EDM veins and biotite crackles	1.7-2.7 (**2.5**)	fluid inclusions[9]	459-659	Zr-in-rutile[5]	1	Presence of rutile	401-467[5]	512-594[5]	
				550-700	Na-K partitioning between kfs and msc[2]					
				520-700	X Mg-Ti-in-bio thermometry[5]					
				550-700	Fe-Ti oxides[7]					
	Barren Quartz/Quartz-molybdenite veins	1.7-2.7 (**2.5**)	fluid inclusions[9]	550-650	S isotope thermometry on adjacent molybdenite-anhydrite grains[3]	1	Presence of rutile	443-543[5]	564-697[5]	
				550-650	fluid inclusions[9]					
				508-634	Zr-in-rutile[5]					
Hydrothermal	Pyrite-quartz veins (GS)	0.4-**0.7**	fluid inclusions and Zr-in-rutile[9]	370-450*	fluid inclusions[9]	1	Presence of rutile	381-425[5]	458-510[5]	
				498 (n=1)	Zr-in-rutile[5]					
				450-550	Thermodynamic modeling[6]	1	Presence of rutie			
	Main stage veins	0.2-0.6 (**0.4**)	Hydrostatic, fluid inclusions[9]	230-400	Fluid inclusions[9]	1	Presence of rutile	<373[5]	<431[5]	

* Bold indicates value used in calculation

1. Ackerson M.R., Mysen B.O., Tailby N.D. and Watson E.B., Low-temperature crystallization of granites and the implications for crustal magmatism, Nature 559, 2018, 94–97.
2. Brimhall G.H., Early Fracture-Controlled Disseminated Mineralization at Butte, Montana. Econ. Geol. 72, 1977, 37–59.
3. Field C.W., Zhang L., Dilles J.H., Rye R.O. and Reed M.H., Sulfur and oxygen isotopic record in sulfate and sulfide minerals of early, deep, pre-Main Stage porphyry Cu-Mo and late Main Stage base-metal mineral deposits, Butte district Montana, Chem. Geol. 215, 2005, 61–93.
4. Houston R.A. and Dilles J.H., Structural geologic evolution of the Butte district, Montana, Econ. Geol. 108, 2013, 1397–1424.
5. Mercer C.N. and Reed M.H., Porphyry Cu-Mo stockwork formation by dynamic, transient hydrothermal pulses: Mineralogic insights from the deposit at Butte, Montana, Econ. Geol. 108, 2013, 1347–1377.
6. Reed M., Rusk B. and Palandri J., The Butte magmatic-hydrothermal system: One fluid yields all alteration and veins, Econ. Geol. 108, 2013, 1379–1396.
7. Roberts S.A., Early hydrothermal alteration and mineralization in the Butte district, Montana: Ph.D. dissertation, 1975, Harvard University, 157 p.
8. Rusk B.G., Reed M.H., Dilles J.H. and Kent A.J.R., Intensity of quartz cathodoluminescence and trace-element content in quartz from the porphyry copper deposit at Butte, Montana, Am. Mineral. 91, 2006, 1300–1312.
9. Rusk B.G., Reed M.H. and Dilles J.H., Fluid inclusion Evidence for Magmatic-hydrothermal Fluid Evolution in the Porphyry Copper-Molybdenum Deposit st Butte, Montana, Econ. Geol. 103, 2008, 307–334.

A.2 PFIB extraction for EPMA analysis

To empirically quantify the amount of secondary fluorescence in our data set, and to assess the accuracy of the PENEPMA modeling, we devised a novel sample preparation method that allowed us to isolate outer quartz crystals from Qz29_ana and analyze them on the microprobe with no SF at all.

After an initial EPMA analysis, we put the polished mount into the Helios G4 PFIB (plasma focused ion beam) UXe DualBeam scanning electron microscope. This machine is unique from other FIB-SEMs in that it can use Xe as an ion source. Beam current was set to 0.5 µA. We milled a 70 µm deep moat around two rectangular areas 40 µm x 30 µm in dimension. For one region, we then milled away any Ti particles within 200 microns of the target (Fig. S2a). For the second region, after we had milled the vertical moat we tilted the sample and began to create a wedge shape. Once a wedge geometry had been established, we tilted the sample 72° from the ion beam and line-cut to bisect the wedge ~8.5 µm below the surface. We milled most of the way through the wedge, then attached the omniprobe micromanipulator to one edge of the rectangular area with carbon at 12 kV. After the omniprobe was adhered to the region, we finished milling all the way through the bottom of the wedge and removed the region from the rest of the sample (Fig. S2d). The ion hewn surface was relatively flat (Fig. S2c).

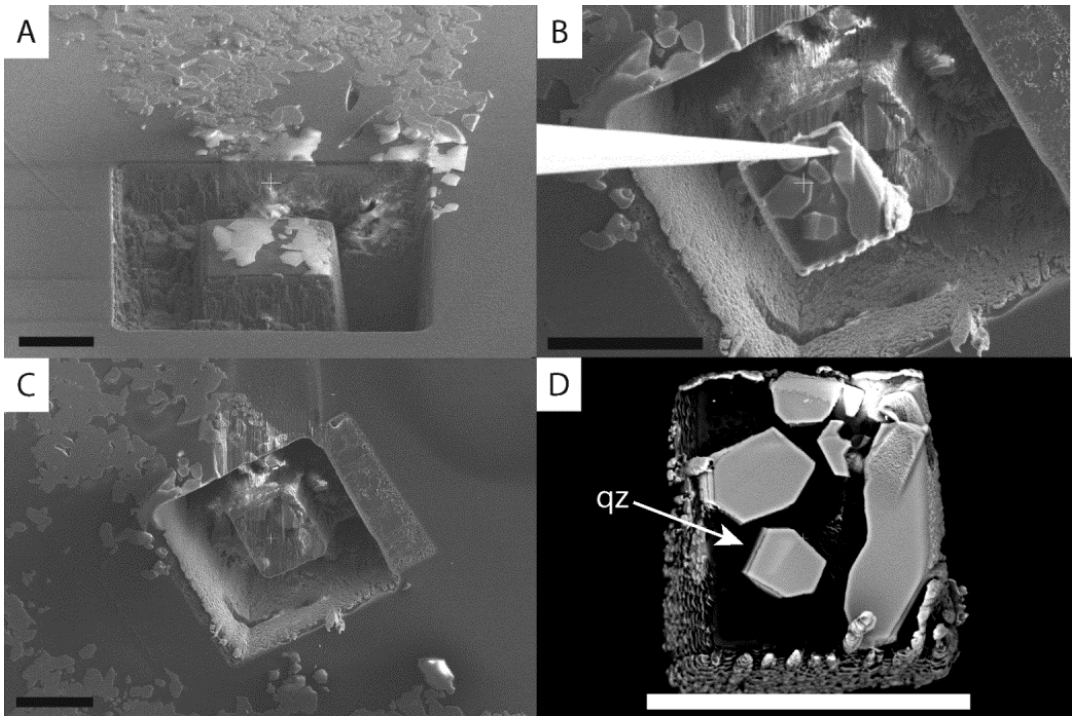

Figure A1. The steps taken on the PFIB to prepare the sample for microprobe analysis sans secondary fluorescence. A) the moat dug around the crystals of interest B) the region of interest being removed from the mount with the omniprobe. C) the region that was cut using the ion milling process, showing how flat it is. D) the region of interest after being adhered to a carbon tab.

Having successfully removed a small region of interest from the larger sample, we retracted the omniprobe, vented the chamber, and inserted a carbon tab adhered to an SEM mount. When the chamber was at pressure and the beams were back on, we inserted the omniprobe along with the region that had been lifted out and adhered it to the carbon tab. We then milled away the tip of the needle that was attached to the sample, leaving behind the flat, polished region (Fig. S2d). Next, we analyzed the two regions prepared on the PFIB-SEM on the microprobe using the procedures outlined in the main text. Two crystals were analyzed and came back at 508 ppm Ti and 594 ppm Ti.

It is important to note that this technique precluded the analysis of many crystals and is quite time intensive. The method is limited to preparing only a few grains at once because often, after one has moated out a region of interest (or even having gone so far as to remove a region of interest), it will become evident that there are TiO2 crystals immediately beneath what was a seemingly TiO_2 free zone. Due to the small size of the crystals, it is rarely possible to mill away the TiO_2 crystals while preserving enough material to analyze with the microprobe.

A.3 PENEPMA modeling of secondary fluorescence

Secondary fluorescence (SF) is the phenomenon whereby primary characteristic and bremsstrahlung (continuum) x-rays generated in the interaction volume (the region of the sample in which the incident electron beam comes to rest within) penetrate any surrounding phases. That is, if another phase is present in the sample, near to the beam incident location, and that surrounding phase contains non-trace amounts of the element of interest, x-rays of interest will be generated within the adjacent phase. This will result in erroneously high concentrations measured for these trace elements.

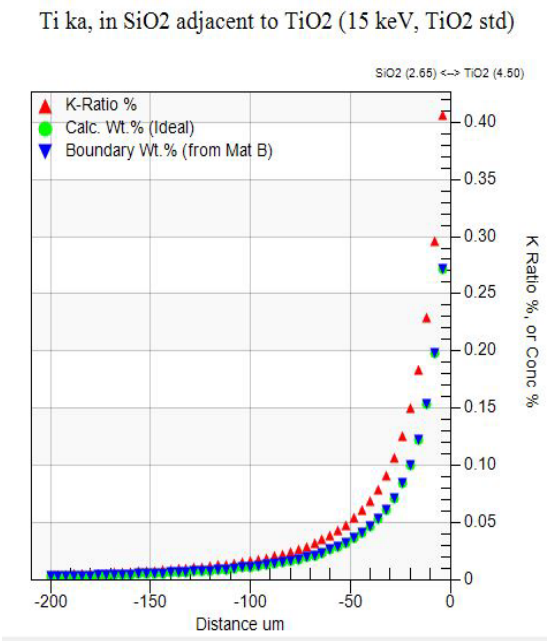

Figure A2. The magnitude of the erroneously high Ti concentration measured in quartz as a function of distance from an infinitely long planar boundary of TiO_2 (the Concentration % units are wt%). The effect is no longer seen by the time the beam is ~150 microns away from the boundary. This is the absolute worst-case scenario for SF contamination of Ti in quartz.

Thus, SF is a serious problem for measuring Ti in quartz when one imposes the criterion for thermodynamic equilibrium that a pure rutile phase co-precipitated with the quartz of interest, as this usually entails finding a rutile crystal close to or as an inclusion in the quartz being measured. In the worst case scenario where one is measuring Ti in quartz near an infinite planar boundary of pure TiO_2, the beam must be ~150 µm away from the boundary to minimize any SF effects, as modeled by the Penfluor GUI in

CalcZAF/Standard (Fig. S3). Fortunately, the electron microprobe is a “mature” technique and, the magnitude of the SF effect has been quantified by modeling and confirmed for many materials by measurements performed near synthetic boundaries in several geometries. Beyond measuring the SF effect, which is tedious and time-consuming, it has been shown that Monte Carlo simulations can accurately and precisely predict the magnitude of these SF effects on trace element measurements even for non-planar geometries. Therefore, one can first model for possible SF effects, and recognize whether SF is a problem at the expected level of EPMA sensitivity, next one can then measure the trace element of interest, model the geometry of the phases present in the sample, and subtract the modeled SF value from the measured value to get the true concentration (for example, using the program CalcZAF/Standard which provides a GUI for the Penepma 2012 Monte Carlo modeling software).

To perform corrections for SF effects of TiO_2 grains near to quartz grains, we used PENEPMA (Llovet and Salvat, 2017) to model how secondary x-rays generated in a 5 µm TiO_2phase are transmitted through epoxy and silica. We chose 5 µm because it was the maximum size of the TiO_2 particles in our outer capsule run products, and epoxy and silica were chosen as transmitting mediums because the crystals we measured were small (10-20 µm) quartz crystals separated from each other and the TiO_2 phase by epoxy. All measurements were taken ~40 microns or more away from any TiO_2 particles. The geometry used for the PENEPMA runs was that of a 5 µm TiO_2 sphere separated from a 20 µm SiO2 sphere by 40 µm of epoxy where the electron beam was centered on the 20 µm quartz grain. The results of the Penepma modeling are presented in Table S1. For analyses where multiple particles of TiO_2 are present, the total amount of SF in the acquired data set can be estimated by multiplying the modeled value for a single particle by the number of particles at the same distance from the beam incident location.

Distance of beam from inclusion	S.F. effect	matrix
10.00	19 ± 2 ppm Ti	SiO_2
20.00	10 ± 1 ppm Ti	SiO_2
40.00	3 ± 1 ppm Ti	SiO_2
10.00	21 ± 2 ppm Ti	epoxy
20.00	11 ± 1 ppm Ti	epoxy
40.00	5 ± 1 ppm Ti	epoxy

Table A2. Model results of the magnitude of secondary fluorescence caused by a 5 micron particle of TiO_2 surrounded in either quartz or

For details on how to do these calculations, please see https://probesoftware.com/smf/index.php?topic=58.0 .

Llovet, Xavier, and Francesc Salvat. "PENEPMA: A Monte Carlo program for the simulation of X-ray emission in electron probe microanalysis." *Microscopy and Microanalysis* 23.3 (2017): 634-646.

A.4 Identification of Polymorphs

Polymorphs of crystalline titania and silica were variably identified with Raman spectroscopy and transmission electron microscope- single area electron diffraction patterns (TEM-SAED). Raman was used because it is fast, but the method is unsuited for differentiating between different crystal morphologies because the data is acquired on polished samples. TEM, in contrast, requires laborious and time-consuming sample prep but allows for each crystal morphology to be separately identified. Below are representative examples of Raman spectra of tridymite, rutile, and anatase (Fig. S4), TEM- SAED patterns used to identify phases of (Fig. S5), and rutile inclusion in quartz overgrowth and it's SAED pattern (Fig. S6).

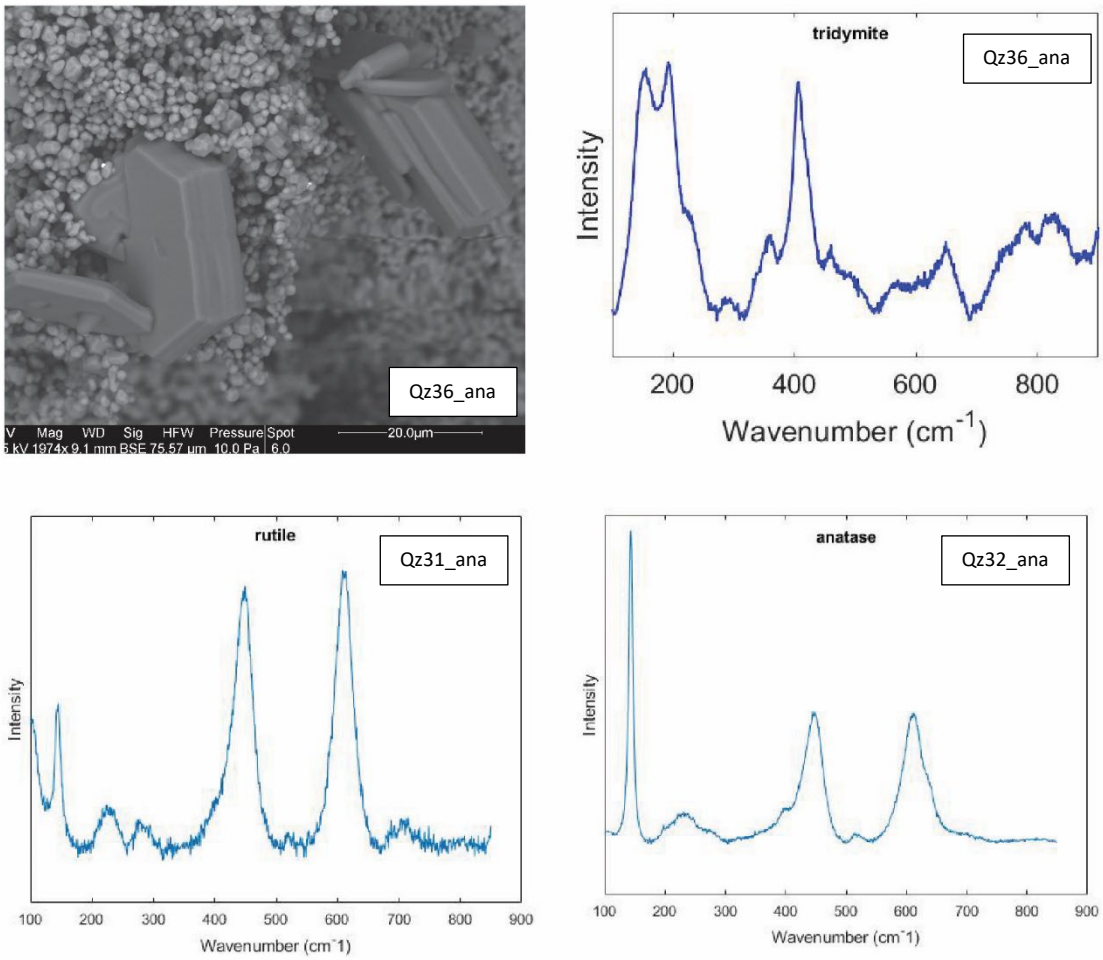

Figure A3. Hexagonal platelets and columns (SEM-BSE image in upper right panel) were imaged in many experiments and some were identified via Raman spectroscopy. Spectra of relevant phases were identified by comparison against reference spectra in the Rruff mineral database online.

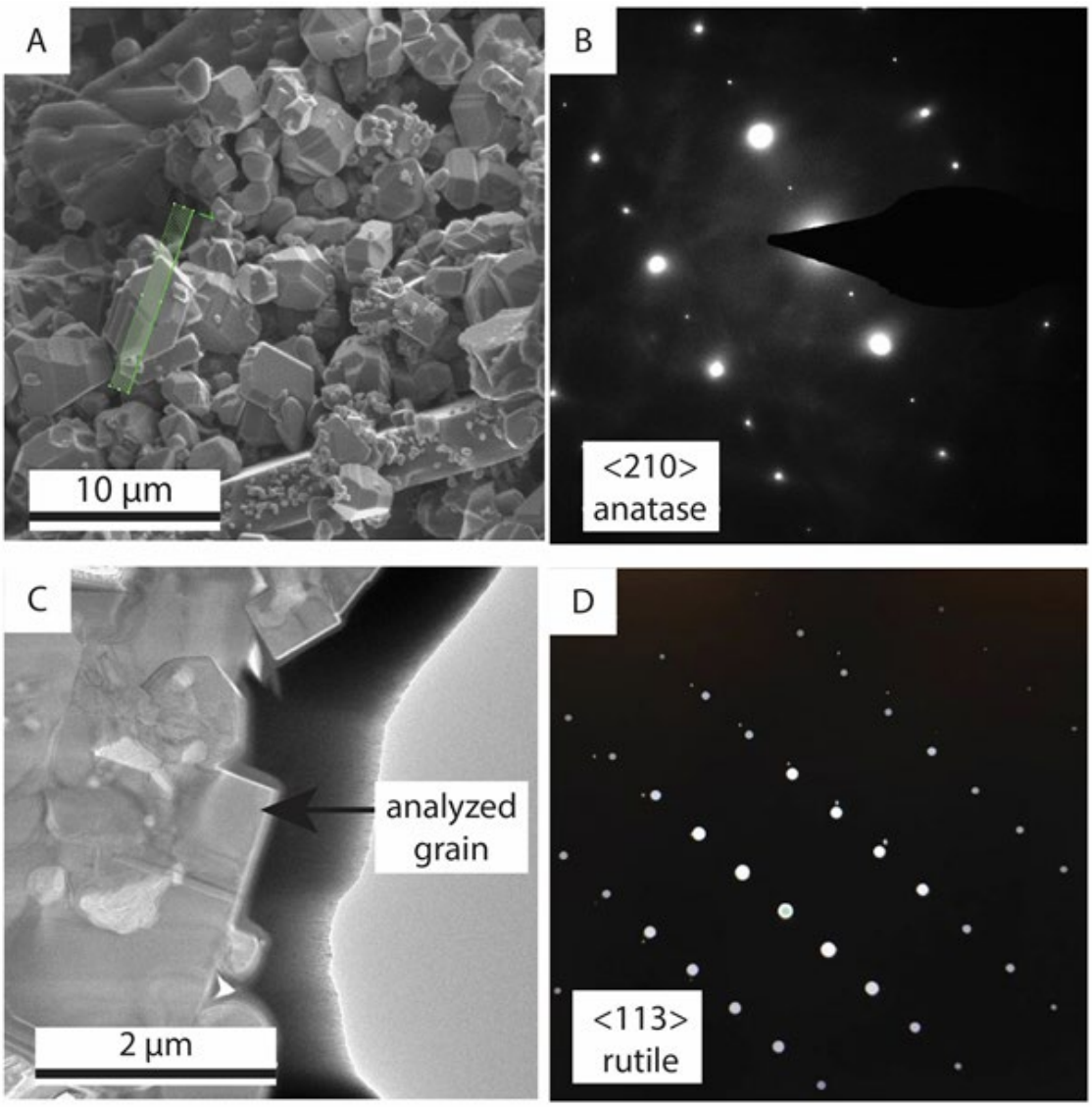

Figure A4. Anatase and rutile crystals identified with TEM-SAED from Qz32_ana. A) Loose crystals of TiO_2 displaying a variety of habits. The green rectangular region bisects the crystal that was made into the TEM sample that yielded B) the <210> zone of anatase collected from the crystal shown in panel A. C) A TEM brightfield image of a rectangular TiO_2 grain that yielded D) the SAED pattern of the <113> zone of rutile.

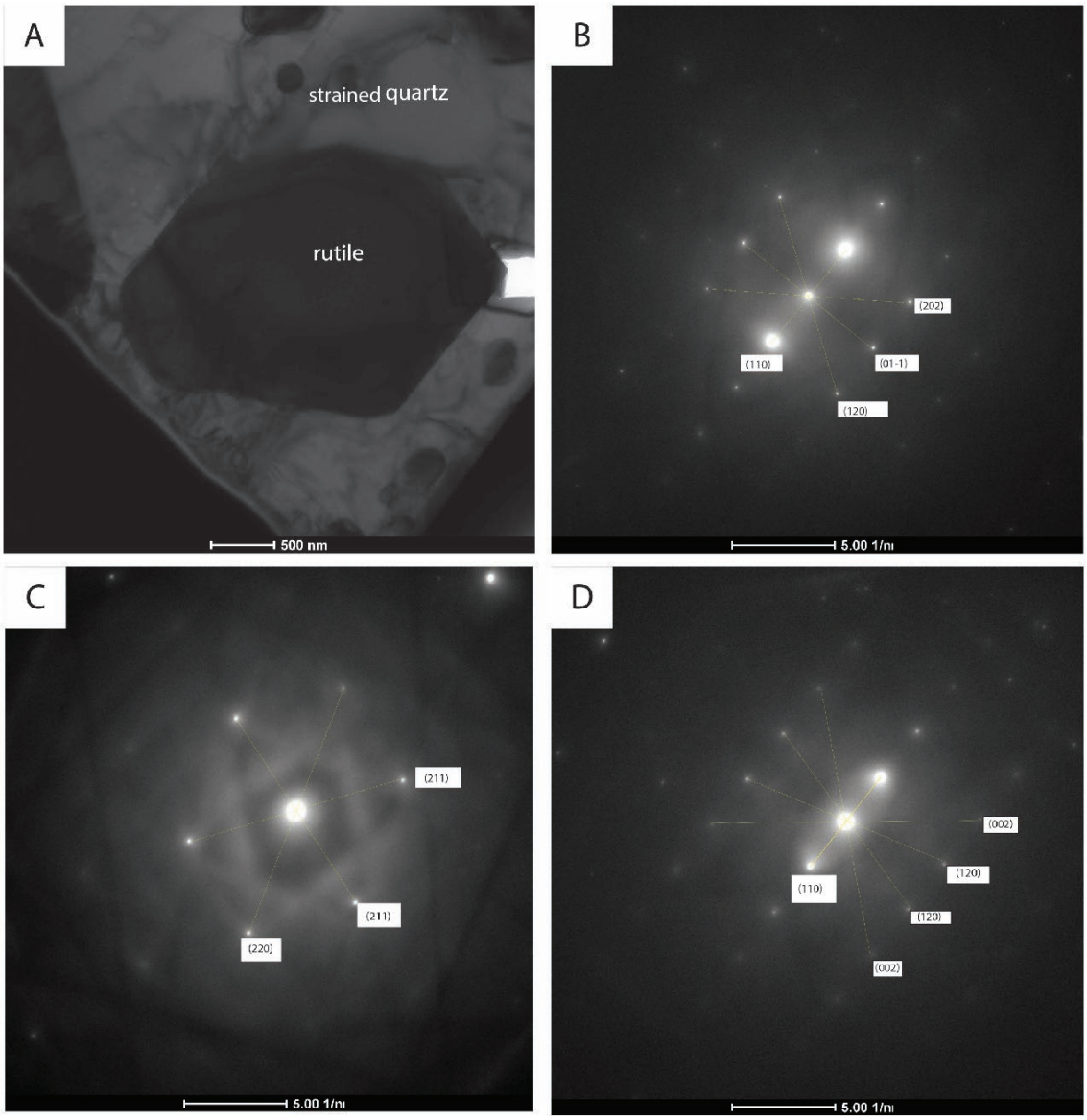

Figure A5. Rutile inclusions surrounded by strained quartz overgrowth from Qz19_ana, an experiment done with a 50:50 mix by weight of SiO_2 to TiO_2 that yielded an overgrowth with abundant TiO_2 inclusions. A) a CCD (charge coupled device) image taken with the TEM showing the euhedral rutile inclusion surrounded by a strained quartz lattice. B-D) SAED reflectors annotated with the Miller indices of the crystal planes that made them.

A.5 SEM-CL and SE Images of Analyzed Overgrowths

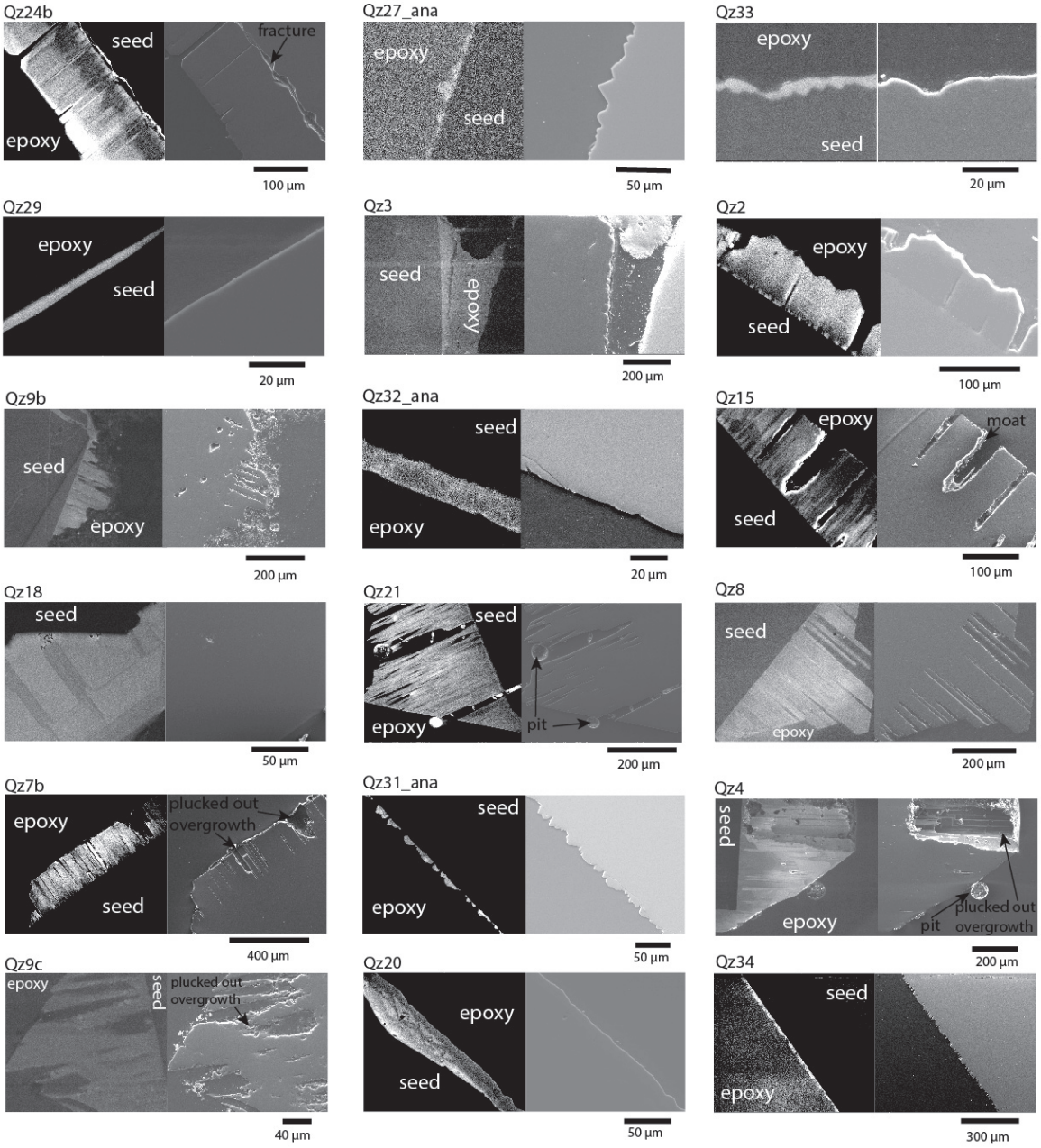

A.6 EPMA Ti concentrations of experimental products

Table A.3

Experiment	Overgrowth Ti (ppm)	Outer quartz Ti (ppm)	Other run products description	Other run products Ti (ppm)
4	443	—	—	—
4	494	—	—	—
4	520	—	—	—
4	546	—	—	—
4	521	—	—	—
4	543	—	—	—
4	519	—	—	—
4	466	—	—	—
4	525	—	—	—
4	509	—	—	—
4	460	—	—	—
4	474	—	—	—
4	485	—	—	—
4	413	—	—	—
4	421	—	—	—
4	442	—	—	—
4	408	—	—	—
4	470	—	—	—
4	527	—	—	—
4	467	—	—	—
2	310	—	—	—
2	313	—	—	—
2	319	—	—	—
2	330	—	—	—
2	347	—	—	—
3	315	—	—	—
3	308	—	—	—
3	301	—	—	—
3	288	—	—	—
3	293	—	—	—
7B	476	—	—	—
7B	513	—	—	—
7B	497	—	—	—
7B	504	—	—	—

Table A3, continued

Experiment	Overgrowth Ti (ppm)	Outer quartz Ti (ppm)	Other run products description	Other run products Ti (ppm)
7B	485	—	—	—
7B	447	—	—	—
7B	392	—	—	—
7B	468	—	—	—
7B	477	—	—	—
7B	493	—	—	—
7B	404	—	—	—
7B	288	—	—	—
7B	432	—	—	—
7B	444	—	—	—
7B	441	—	—	—
7B	418	—	—	—
7B	437	—	—	—
8	406	—	—	—
8	421	—	—	—
8	375	—	—	—
8	447	—	—	—
8	462	—	—	—
8	460	—	—	—
8	478	—	—	—
8	422	—	—	—
8	482	—	—	—
8	357	—	—	—
8	468	—	—	—
9c	534	458	—	—
9c	534	562	—	—
9c	541	533	—	—
9c	570	—	—	—
9c	545	—	—	—
9c	513	—	—	—
9c	216	—	—	—
9c	289	—	—	—
9c	315	—	—	—
9c	294	—	—	—
9c	278	—	—	—

Table A3, continued

Experiment	Overgrowth Ti (ppm)	Outer quartz Ti (ppm)	Other run products description	Other run products Ti (ppm)
9c	290	—	—	—
9c	345	—	—	—
9c	301	—	—	—
9c	329	—	—	—
9c	303	—	—	—
9c	312	—	—	—
9b	329	—	—	—
9b	356	—	—	—
9b	235	—	—	—
15	358	629	—	—
15	340	—	—	—
15	388	—	—	—
15	306	—	—	—
15	400	—	—	—
15	308	—	—	—
15	303	—	—	—
15	275	—	—	—
15	364	—	—	—
15	324	—	—	—
15	393	—	—	—
15	339	—	—	—
15	365	—	—	—
15	362	—	—	—
15	342	—	—	—
15	335	—	—	—
15	443	—	—	—
15	403	—	—	—
15	338	—	—	—
18	405	—	—	—
18	454	—	—	—
18	416	—	—	—
18	419	—	—	—
18	378	—	—	—
18	346	—	—	—
18	376	—	—	—

Table A3, continued

Experiment	Overgrowth Ti (ppm)	Outer quartz Ti (ppm)	Other run products description	Other run products Ti (ppm)
18	272	—	—	—
18	309	—	—	—
18	440	—	—	—
20	555	—	—	—
20	568	—	—	—
20	582	—	—	—
20	486	—	—	—
20	457	—	—	—
20	475	—	—	—
20	449	—	—	—
20	478	—	—	—
20	416	—	—	—
20	435	—	—	—
20	483	—	—	—
20	199	—	—	—
20	337	—	—	—
20	403	—	—	—
20	271	—	—	—
20	318	—	—	—
20	519	—	—	—
20	446	—	—	—
20	461	—	—	—
21	288	—	—	—
21	303	—	—	—
21	279	—	—	—
21	278	—	—	—
21	296	—	—	—
21	301	—	—	—
21	305	—	—	—
21	293	—	—	—
21	297	—	—	—
21	281	—	—	—
21	306	—	—	—
21	453	—	—	—
21	394	—	—	—

Table A3, continued

Experiment	Overgrowth Ti (ppm)	Outer quartz Ti (ppm)	Other run products description	Other run products Ti (ppm)
21	455	—	—	—
21	464	—	—	—
21	422	—	—	—
21	424	—	—	—
21	400	—	—	—
21	401	—	—	—
21	398	—	—	—
21	387	—	—	—
21	397	—	—	—
21	411	—	—	—
21	382	—	—	—
21	399	—	—	—
21	347	—	—	—
21	379	—	—	—
21	335	—	—	—
21	331	—	—	—
24b	36	129	tridymite	314
24b	36	27	tridymite	339
24b	39	20	tridymite	268
24b	37	43	tridymite	315
24b	42	421	tridymite	321
24b	50	402	tridymite	348
24b	44	63	tridymite	298
24b	42	67	tridymite	404
24b	42	200	tridymite	428
24b	33	18	tridymite	404
24b	39	14	tridymite	368
24b	35	101	tridymite	335
24b	41	102	tridymite	431
24b	34	128	tridymite	163
24b	33	36	tridymite	296
24b	38	133	tridymite	306
24b	35	83	tridymite	324
24b	33	182	tridymite	390
24b	46	86	tridymite	310

Table A3, continued

Experiment	Overgrowth Ti (ppm)	Outer quartz Ti (ppm)	Other run products description	Other run products Ti (ppm)
24b	32	487	tridymite	324
24b	29	356	tridymite	415
24b	39	146	tridymite	356
24b	37	17	tridymite	406
24b	38	97	tridymite	383
24b	37	68	tridymite	321
24b	32	45	tridymite	381
24b	38	231	tridymite	312
24b	30	26	tridymite	238
24b	35	—	—	—
24b	29	—	—	—
24b	33	—	—	—
24b	31	—	—	—
24b	31	—	—	—
24b	34	—	—	—
24b	34	—	—	—
24b	35	—	—	—
24b	35	—	—	—
24b	34	—	—	—
24b	41	—	—	—
24b	42	—	—	—
24b	34	—	—	—
24b	32	—	—	—
24b	40	—	—	—
24b	42	—	—	—
24b	39	—	—	—
24b	40	—	—	—
24b	41	—	—	—
24b	39	—	—	—
24b	44	—	—	—
24b	43	—	—	—
24b	38	—	—	—
24b	46	—	—	—
24b	46	—	—	—
24b	46	—	—	—

Table A3, continued

Experiment	Overgrowth Ti (ppm)	Outer quartz Ti (ppm)	Other run products description	Other run products Ti (ppm)
24b	40	—	—	—
24b	42	—	—	—
24b	34	—	—	—
24b	38	—	—	—
24b	39	—	—	—
24b	37	—	—	—
24b	41	—	—	—
24b	28	—	—	—
24b	37	—	—	—
24b	33	—	—	—
24b	36	—	—	—
24b	36	—	—	—
24b	40	—	—	—
24b	38	—	—	—
24b	38	—	—	—
24b	42	—	—	—
24b	52	—	—	—
24b	44	—	—	—
24b	45	—	—	—
24b	51	—	—	—
24b	48	—	—	—
24b	49	—	—	—
24b	36	—	—	—
24b	33	—	—	—
24b	37	—	—	—
24b	39	—	—	—
24b	38	—	—	—
24b	31	—	—	—
24b	41	—	—	—
24b	44	—	—	—
24b	41	—	—	—
24b	40	—	—	—
24b	37	—	—	—
24b	41	—	—	—
24b	42	—	—	—

Table A3, continued

Experiment	Overgrowth Ti (ppm)	Outer quartz Ti (ppm)	Other run products description	Other run products Ti (ppm)
24b	43	—	—	—
24b	43	—	—	—
24b	45	—	—	—
24b	45	—	—	—
24b	49	—	—	—
24b	49	—	—	—
24b	53	—	—	—
24b	50	—	—	—
24b	53	—	—	—
24b	62	—	—	—
24b	55	—	—	—
24b	56	—	—	—
29_ana	188	581		
29_ana	196	479	—	—
29_ana	126	765		
29_ana	155	564	—	—
29_ana	203	850		
29_ana	223	539	—	—
29_ana	180	361		
29_ana	212	803	—	—
29_ana	230	531		
29_ana	227	177	—	—
29_ana	192	361		
29_ana	229	890	—	—
29_ana	237	797		
29_ana	204	669	—	—
29_ana	204	666		
29_ana	209	590	—	—
29_ana	216	450		
29_ana	234	711	—	—
29_ana	220	—	—	—
29_ana	239	—	—	—
29_ana	248	—	—	—
29_ana	231	—	—	—
29_ana	239	—	—	—

Table A3, continued

Experiment	Overgrowth Ti (ppm)	Outer quartz Ti (ppm)	Other run products description	Other run products Ti (ppm)
31_ana	233	686	—	—
31_ana	505	691	—	—
31_ana	186	870	—	—
31_ana	431	582	—	—
31_ana	288	667	—	—
31_ana	111	700	—	—
31_ana	220	637	—	—
31_ana	179	552	—	—
31_ana	—	620	—	—
31_ana	—	714	—	—
31_ana	—	625	—	—
31_ana	—	741	—	—
27_ana	113	43	tridymite	185
27_ana	118	59	tridymite	248
27_ana	117	36	tridymite	184
27_ana	126	81	tridymite	182
27_ana	109	249	tridymite	194
27_ana	105	350	tridymite	218
27_ana	118	201	tridymite	346
27_ana	—	255	tridymite	148
27_ana	—	328	tridymite	167
27_ana	—	306	tridymite	259
27_ana	—	199	tridymite	228
27_ana	—	306	tridymite	241
27_ana	—	—	tridymite	293
27_ana	—	—	tridymite	290
27_ana	—	—	tridymite	209
32_ana	400	—	tridymite	644
32_ana	275	—	tridymite	689
32_ana	331	—	tridymite	638
32_ana	310	—	tridymite	726
32_ana	386	—	tridymite	738
32_ana	322	—	tridymite	658
32_ana	321	—	tridymite	783
32_ana	419	—	tridymite	756

Table A3, continued

Experiment	Overgrowth Ti (ppm)	Outer quartz Ti (ppm)	Other run products description	Other run products Ti (ppm)
32_ana		—	tridymite	725
33	215	—	tridymite	489
33	211	—	tridymite	559
34	—	—	tridymite	546
35	—	—	tridymite	433
36	—	—	tridymite	553
37	—	—	quench sphere	764
38	—	—	quench sphere	514
39	—	—	quench sphere	559
40	—	—	quench sphere	579
41	—	—	quench sphere	546
42	—	—	quench sphere	711
43	—	—	anhedral mass	452
44	—	—	anhedral mass	638
45	—	—	anhedral mass	691
46	—	—	anhedral mass	779
47	—	—	anhedral mass	675
48	—	—	anhedral mass	628
49	—	—	anhedral mass	563
50	—	—	anhedral mass	507
51	—	—	anhedral mass	485

Table A3, continued

Experiment	Overgrowth Ti (ppm)	Outer quartz Ti (ppm)	Other run products description	Other run products Ti (ppm)
52	—	—	anhedral mass	526
34	520	—	cristobalite	924
34	489	—	cristobalite	920
34	489	—	cristobalite	1140
34	673	—	cristobalite	950
34	483	—	cristobalite	992
34	491	—	cristobalite	889
34	493	—	—	—
34	416	—	—	—
34	465	—	—	—
35_ana	758	—	—	—
35_ana	767	—	—	—
35_ana	866	—	—	—
35_ana	807	—	—	—
35_ana	684	—	—	—
35_ana	608	—	—	—
35_ana	756	—	—	—
35_ana	916	—	—	—
35_ana	952	—	—	—
36	437	—	anhedral mass	22500
36	582	—	anhedral mass	18168
37		—	anhedral mass	16475
15	1396	—	—	—

APPENDIX B
CHAPTER III SUPPORTING
MATERIALS

B.1 Hand Samples

Barren quartz hand samples from DDH1-A (all scale bars are 4.7 cm)

11052-6450

11052-6453

11052-6882

11052-6567

Quartz-molybdenite hand samples from Continental Pit

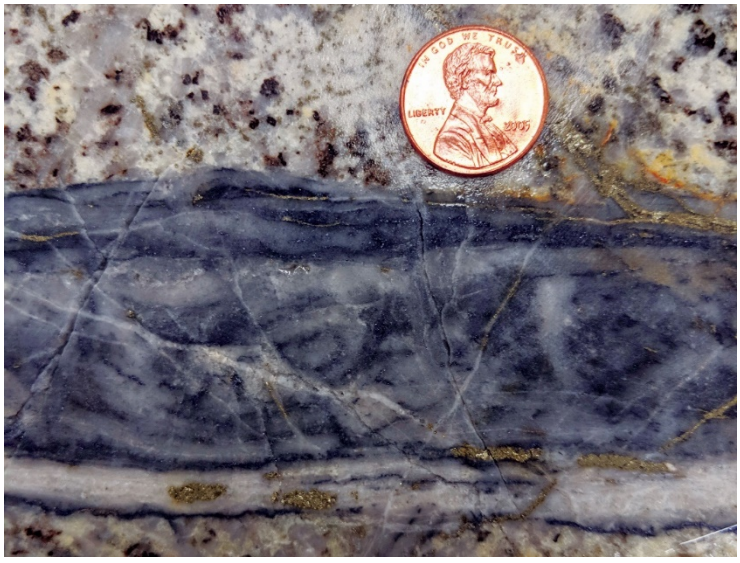

Main Stage vein hand sample

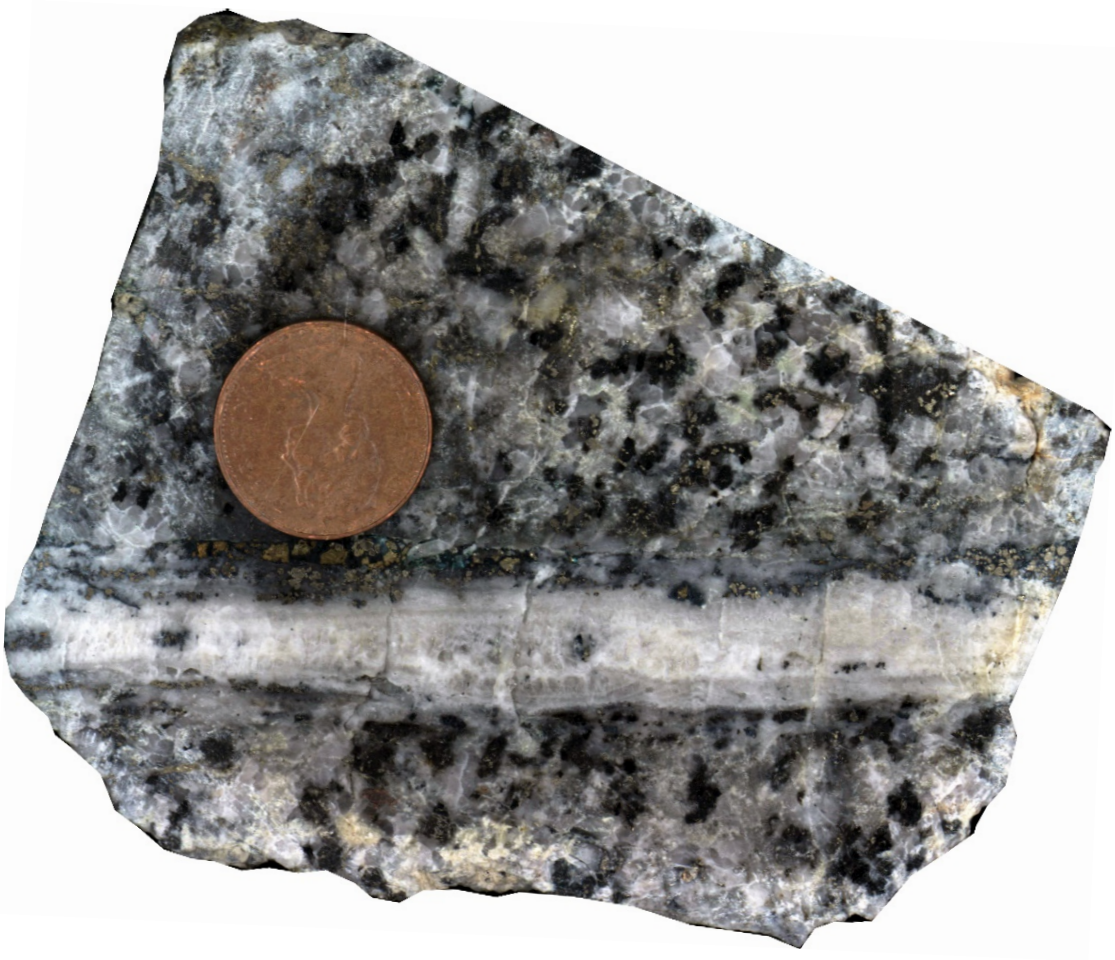

B.2 Main Stage vein CL images

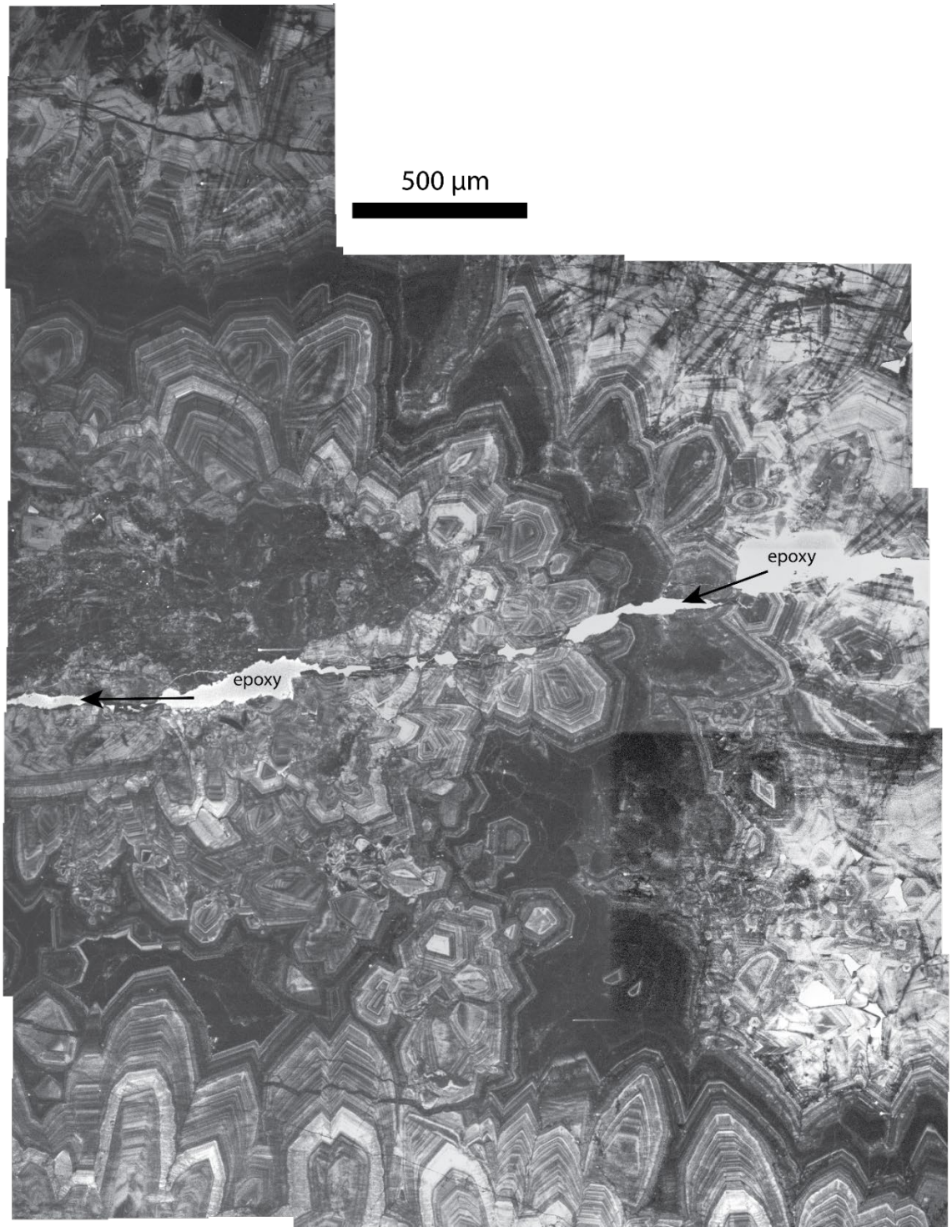

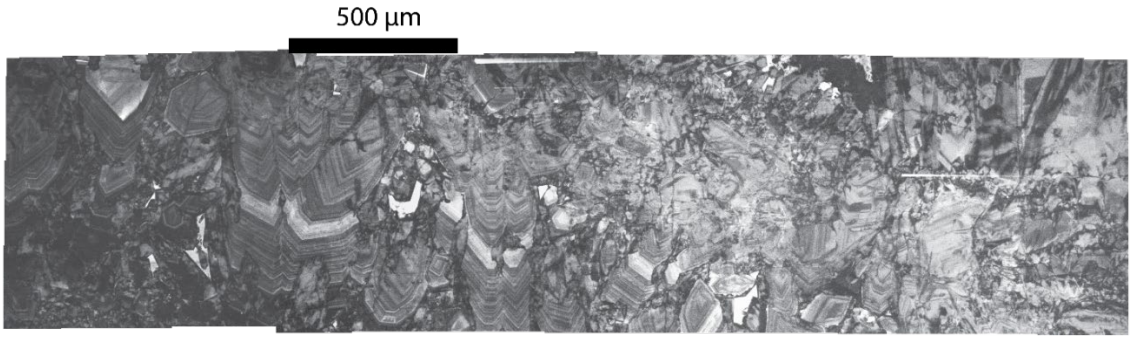

Micro-chaotic texture (all scale bars are 500 µm)

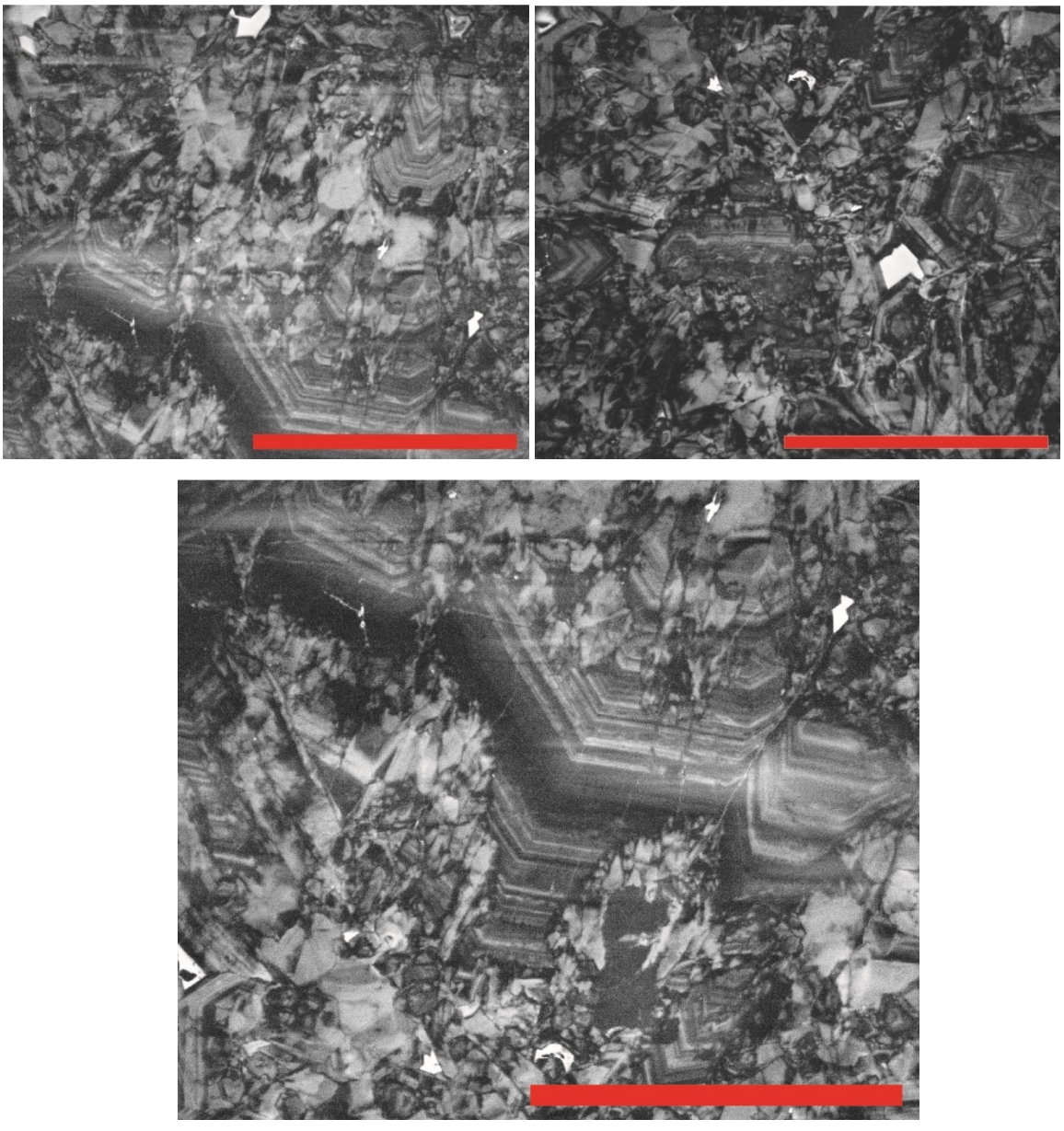

B.3 Ti data used in Chapter III

Table B.1 EPMA Ti concentrations of different CL-domains in single crystals from sample BMA-018-16fa.

Crystal 1

Bright	+ or - ppm error	Dark	+ or - ppm error
35.6	3.7	10.3	3.7
29.1	3.7	7.6	3.7
74.2	3.7	15.6	3.7
18.5	3.7	14.2	3.7
34.8	3.7	8.8	3.7
28.3	3.7	21.1	3.7
30.6	3.7	29.9	3.7
31.6	3.7		
26.5	3.7		
26.5	3.7		

Crystal 2

Bright	+ or - ppm error	Dark	+ or - ppm error
38.5	3.7	8.3	3.7
52.7	3.7	14.3	3.7
31.9	3.7	12.7	3.7
25.3	3.7	18.2	3.7
17.4	3.7	11.9	3.7
25.1	3.7	30.4	3.7
19.1	3.7		
40.4	3.7		

Table B.1, continued

Crystal 3

Bright	+ or - ppm error	Dark	+ or - ppm error	Mottled Edge	+ or - ppm error
77.0	3.7	28.2	3.7	32.9	3.7
124.0	3.8	33.4	3.7	26.2	3.7
96.1	3.7	31.5	3.7	29.4	3.7
133.5	3.8	27.4	3.7	36.6	3.7
76.7	3.7	33.4	3.7	37.5	3.7
62.2	3.7	33.2	3.7	31.9	3.7
70.0	3.7	38.0	3.7	32.6	3.7
113.2	3.8	34.5	3.7	24.7	3.7
45.1	3.7	22.7	3.7	40.1	3.7
50.2	3.7	24.3	3.7	45.3	3.7

Crystal 3, continued

Bright	+ or - ppm error	Dark	+ or - ppm error	Mottled Edge	+ or - ppm error
		26.3	3.7	31.7	3.7
		28.2	3.7	26.6	3.7
		39.6	3.7	41.5	3.7
		18.7	3.7	39.8	3.7
		30.0	3.7	41.9	3.7
		31.5	3.7	27.8	3.7
				24.0	3.7
				26.2	3.7
				33.9	3.7
				41.5	3.7
				34.8	3.7
				34.2	3.7
				28.7	3.7
				27.4	3.7
				34.4	3.7
				35.8	3.7
				28.6	3.7
				34.2	3.7

Table B.1, continued

Crystal 4

Bright	+ or - ppm error	Dark	+ or - ppm error	Mottled Edge	+ or - ppm error
293.5	3.9	21.8	3.7	14.3	3.7
164.9	3.8	23.1	3.7	15.8	3.7
143.6	3.8	25.5	3.7	25.7	3.7
322.9	3.9	30.5	3.7	18.3	3.7
172.6	3.8	23.9	3.7	24.6	3.7
32.9	3.7	31.9	3.7	30.0	3.7
159.9	3.8	16.6	3.7	44.1	3.7
153.5	3.8	16.2	3.7	33.4	3.7
47.6	3.7	24.9	3.7	35.7	3.7
87.2	3.7	22.5	3.7	11.4	3.7
54.2	3.7	31.4	3.7	25.3	3.7
56.6	3.7	29.6	3.7	20.5	3.7
56.1	3.7	31.2	3.7	19.7	3.7
50.6	3.7	25.9	3.7	12.6	3.7
34.5	3.7	25.1	3.7	29.4	3.7
71.2	3.7	30.6	3.7	27.4	3.7
63.6	3.7	23.2	3.7	22.7	3.7

Crystal 4, continued

Bright	+ or - ppm error	Dark	+ or - ppm error	Mottled Edge	+ or - ppm error
76.9	3.7	20.9	3.7	25.2	3.7
99.2	3.7	21.6	3.7	10.5	3.7
125.2	3.8	32.7	3.7	7.2	3.7
62.1	3.7	29.3	3.7		
51.0	3.7	28.0	3.7		
59.6	3.7	26.6	3.7		
212.5	3.8	26.0	3.7		
148.2	3.8				
95.7	3.7				
57.0	3.7				
79.6	3.7				
86.2	3.7				
52.5	3.7				
88.2	3.7				

Table B.2 Mottled CL EPMA Ti data

Mottled from BMA-018-16fa_15	11052-6019	11052-6121
27.1 ±3.7	19.8 ±2.3	38.6 ±2.3
38.1 ±3.7	23.7 ±2.3	34.0 ±2.3
47.3 ±3.7	29.7 ±2.3	33.3 ±2.3
29.5 ±3.7	34.9 ±2.3	36.5 ±2.3
30.5 ±3.7	26.1 ±2.3	41.3 ±2.3
36.6 ±3.7	34.2 ±2.3	41.8 ±2.3
22.8 ±3.7	31.9 ±2.3	28.6 ±2.3
30.7 ±3.7	48.4 ±2.3	33.2 ±2.3
26.9 ±3.7	42.3 ±2.3	10.8 ±2.3
24.6 ±3.7	23.3 ±2.3	48.1 ±2.3
30.5 ±3.7	54.5 ±2.4	14.6 ±2.3
25.0 ±3.7	75.7 ±2.4	15.6 ±2.3
30.5 ±3.7	18.0 ±2.3	10.4 ±2.3
27.2 ±3.7	23.9 ±2.3	98.9 ±2.3
30.8 ±3.7	58.8 ±2.4	43.9 ±2.3
	49.2 ±2.3	80.8 ±2.3
	41.5 ±2.3	63.9 ±2.3
		12.4 ±2.3
		18.5 ±2.3
		13.7 ±2.3
		11.5 ±2.3
		36.3 ±2.3
		53.5 ±2.3
		44.4 ±2.3
		43.7 ±2.3
		51.4 ±2.3
		48.4 ±2.3
		49.0 ±2.3
		62.4 ±2.3
		31.4 ±2.4
		18.5 ±5.4
		52.6 ±6.7
		49.3 ±2.2
		11.8 ±2.3
		27.8 ±5.5
		50.8 ±4.3

Table B2, continued

11052-6121, continued
60.2 ±2.8
62.8 ±2.5
37.4 ±1.4
60.2 ±3.8
23.9 ±2.0
45.7 ±4.5
22.4 ±2.0
13.3 ±2.0
33.9 ±6.0
25.1 ±2.0

REFERENCES

Ackerson M. R., Mysen B. O., Tailby N. D. and Watson E. B. (2018) Low-temperature crystallization of granites and the implications for crustal magmatism. *Nature* **559**, 94–97.

Antignano A. and Manning C. E. (2008) Rutile solubility in H_2O, H_2O-SiO_2, and H_2O-$NaAlSi_3O_8$ fluids at 0.7-2.0 GPa and 700-1000 °C: Implications for mobility of nominally insoluble elements. *Chem. Geol.* **255**, 283–293.

Aquilano D. and Abbona F. (2010) Morphology of Crystals Grown from Solutions Epitaxial growth of Ca-sulfates (gypsum, bassanite) on Ca-carbonate (calcite) View project Morphology of crystals grown from solutions. *Springer*, 53–92.

Ashley K. T., Carlson W. D., Law R. D. and Tracy R. J. (2014) Ti resetting in quartz during dynamic recrystallization: Mechanisms and significance. *Am. Mineral.* **99**, 2025–2030.

Ashley K. T., Webb L. E., Spear F. S. and Thomas J. B. (2013) P-T-D histories from quartz: A case study of the application of the TitaniQ thermobarometer to progressive fabric development in metapelites. *Geochemistry, Geophys. Geosystems* **14**, 3821–3843.

Behr W. M. and Platt J. P. (2011) A naturally constrained stress profile through the middle crust in an extensional terrane. *Earth Planet. Sci. Lett.* **303**, 181–192.

Bergman H. and Piazolo S. (2012) The recognition of multiple magmatic events and pre-existing deformation zones in metamorphic rocks as illustrated by CL signatures and numerical modelling: examples from the Ballachulish contact aureole, Scotland. *Int. J. Earth Sci.* **101**, 1127–1148.

Besford, Q. A., Christofferson, A. J., Kalayan, J., Sommer, J. U., & Henchman, R. H. (2020). The Attraction of Water for Itself at Hydrophobic Quartz Interfaces. *The Journal of Physical Chemistry* B, **124**(29), 6369-6375.

Bestmann M. and Pennacchioni G. (2015) Ti distribution in quartz across a heterogeneous shear zone within a granodiorite: The effect of deformation mechanism and strain on Ti resetting. *Lithos* **227**, 37–56.

Betsi T. B. and Lentz D. R. (2010) The nature of "quartz eyes" hosted by dykes associated with Au-Bi-As-Cu, Mo-Cu, and base-metal-Au-Ag mineral occurrences in the mountain freegold region (Dawson Range), Yukon, Canada. *J. Geosci.* **55**, 347–368.

Björneholm O., Hansen M. H., Hodgson A., Liu L. M., Limmer D. T., Michaelides A., Pedevilla P., Rossmeisl J., Shen H., Tocci G., Tyrode E., Walz M. M., Werner J. and Bluhm H. (2016) Water at Interfaces. *Chem. Rev.* **116**, 7698–7726.

Borisova, A.Y., Zagrtdenov, N.R., Toplis, M.J., Donovan, J.J., Llovet, X., Asimow, P.D., de Parseval, P. and Gouy, S. (2018) Secondary fluorescence effects in microbeam analysis and their impacts on geospeedometry and geothermometry. *Chemical Geology* **490**, 22-29.

Brimhall G. H. (1973) Mineralogy, texture, and chemistry of early wall rock alteration in the deep underground mines and Continental area, Butte District, Montana. *Soc. Econ. Geol. Butte F. Meet. Proc.*, H1–H5.

Brimhall G. H. (1977) Early Fracture-Controlled Disseminated Mineralization at Butte , Montana ' Large. *Econ. Geol.* **72**, 37–59.

Bromiley G. D. and Hiscock M. (2016) Grain boundary diffusion of titanium in polycrystalline quartz and its implications for titanium in quartz (TitaniQ) geothermobarometry. *Geochim. Cosmochim. Acta* **178**, 281–290.

Burton W. K., Cabrera N. and Frank F. C. (1951) The growth of crystals and the equilibrium structure of their surfaces. *Philos. Trans. R. Soc. London. Ser. A, Math. Phys. Sci.* **243**, 299–358.

Cabrera N. and Vermilyea D. A. (1958) Growth and perfection of crystals. In (eds. R. H. Doremus, B. W. Roberts, and D. Turnbull). Chapman and Hall, London.

Cernuschi, F., Dilles, J. H., Grocke, S. B., Valley, J. W., Kitajima, K., & Tepley, F. J. (2018). Rapid formation of porphyry copper deposits evidenced by diffusion of oxygen and titanium in quartz. *Geology*, **46**(7), 611-614.

Chamberlain K. J., Morgan D. J. and Wilson C. J. N. (2014) Timescales of mixing and mobilisation in the Bishop Tuff magma body: perspectives from diffusion chronometry. *Contrib. to Mineral. Petrol.* **168**, 1034.

Cherniak D.J., Watson E.B. and Wark D.A. (2007) Ti diffusion in quartz. *Chem. Geol.* **236**, 65–74.

Covert, P. A., & Hore, D. K. (2016). Geochemical insight from nonlinear optical studies of mineral–water interfaces. *Annual Review of Physical Chemistry*, **67**, 233-257.

Darmali C., Mansouri S., Yazdanpanah N. and Woo M. W. (2019) Mechanisms and Control of Impurities in Continuous Crystallization: A Review. *Ind. Eng. Chem. Res.* **58**, 1463–1479.

Davey R. J. (1976) The effect of impurity adsorption on the kinetics of crystal growth from solution. *J. Cryst. Growth* **34**, 109–119.

De Yoreo, J.J., Zepeda-Ruiz, L.A., Friddle, R.W., Qiu, S.R., Wasylenki, L.E., Chernov, A.A., Gilmer, G.H. and Dove, P.M., 2009. Rethinking classical crystal growth models through molecular scale insights: consequences of kink-limited kinetics. *Crystal Growth & Design*, **9**(12), pp.5135-5144.

DelloStritto M. J., Kubicki J. D. and Sofo J. O. (2016) Effect of Ions on H-Bond Structure and Dynamics at the Quartz(101)-Water Interface. *Langmuir* **32**, 11353–11365.

DePaolo, D.J. (2011) Surface kinetic model for isotopic and trace element fractionation during precipitation of calcite from aqueous solutions. *Geochim. Cosmochim. Acta* **75**, 1039–1056.

Donovan J. J., Singer J. W. and Armstrong J. T. (2016) A new EPMA method for fast trace element analysis in simple matrices. *Am. Mineral.* **101**, 1839–1853.

Donovan J. J., Singer J. W. and Armstrong J. T. (2016) A New EPMA Method for Fast Trace Element Analysis in Simple Matrices. *Am. Mineral.* **101**, 1839–1853.

Donovan, J. J., Lowers, H. A., & Rusk, B. G. (2011). Improved electron probe microanalysis of trace elements in quartz. American Mineralogist, 96(2-3), 274-282.

Einaudi M. T., Hedenquist J. W. and Esra Inan E. (2003) Sulfidation State of Fluids in Active and Extinct Hydrothermal Systems: Transitions from Porphyry to Epithermal Environments. *Spec. Publ. Econ. Geol.* **10**, 285–314.

Field C. W., Zhang L., Dilles J. H., Rye R. O. and Reed M. H. (2005) Sulfur and oxygen isotopic record in sulfate and sulfide minerals of early, deep, pre-Main Stage porphyry Cu-Mo and late Main Stage base-metal mineral deposits, Butte district, Montana. *Chem. Geol.* **215**, 61–93.

Field C. W., Zhang L., Dilles J. H., Rye R. O. and Reed M. H. (2005) Sulfur and oxygen isotopic record in sulfate and sulfide minerals of early, deep, pre-Main Stage porphyry Cu–Mo and late Main Stage base-metal mineral deposits, Butte district, Montana. *Chem. Geol.* **215**, 61–93.

Fournier R. (1985) The behavior of silica in hydrothermal solutions. *Rev. Econ. Geol.* **2**, 45–60.

Frank F. C. (1949) The influence of dislocations on crystal growth. *Discuss. Faraday Soc.* **5**, 48–54.

Gabitov, R. I., & Watson, E. B. (2006) Partitioning of strontium between calcite and fluid. *Geochemistry, Geophysics, Geosystems* **7**(11).

Ghiorso M. S. and Evans B. W. (2008) Thermodynamics of rhombohedral oxide solid solutions and a revision of the Fe-Ti two-oxide geothermometer and oxygen-barometer. *Am. J. Sci.* **308**, 957–1039.

Girard G. and Stix J. (2012) Future volcanism at Yellowstone caldera: Insights from geochemistry of young volcanic units and monitoring of volcanic unrest. *GSA Today* **22**, 4–10

Gouma P. I. and Mills M. J. (2001) Anatase-to-Rutile Transformation in Titania Powders. *J. Am. Ceram. Soc.* **84**, 619–622.

Grigor′ev, D. P., Brenner, Y., & Israel Program for Scientific Translations. (1965). Ontogeny of minerals (p. 250). Jerusalem: Israel Program for Scientific Translations.

Grujic D., Stipp M. and Wooden J. L. (2011) Thermometry of quartz mylonites: Importance of dynamic recrystallization on Ti-in-quartz reequilibration. *Geochemistry, Geophys. Geosystems* **12**.

Haertel M., Herwegh M. and Pettke T. (2013) Titanium-in-quartz thermometry on synkinematic quartz veins in a retrograde crustal-scale normal fault zone. *Tectonophysics* **608**, 468–481.

Hanaor D. A. H. and Sorrell C. C. (2011) Review of the anatase to rutile phase transformation. *J. Mater. Sci.* **46**, 855–874.

Heinrich C. A. (2005) The physical and chemical evolution of low-salinity magmatic fluids at the porphyry to epithermal transition: a thermodynamic study. *Miner. Depos.* **39**, 864–889.

Houston R. A. and Dilles J. H. (2013) Structural geologic evolution of the Butte district, Montana. *Econ. Geol.* **108**, 1397–1424.

Houston R. A. and Dilles J. H. (2013) Structural geologic evolution of the Butte district, Montana. *Econ. Geol.* **108**, 1397–1424.

Huang R. and Audétat A. (2012) The titanium-in-quartz (TitaniQ) thermobarometer: A critical examination and re-calibration. *Geochim. Cosmochim. Acta* **84**, 75–89.

Huang R. and Audétat A. (2012) The titanium-in-quartz (TitaniQ) thermobarometer: A critical examination and re-calibration. *Geochim. Cosmochim. Acta* **84**, 75–89.

Johnson, J., Oelkers, E., and Helgeson, H., 1992, SUPCRT92: A software package for calculating the standard molal thermodynamic properties of minerals, gases, aqueous species, and reactions from 1 to 5000 bar and 0 to 1000°C: Computers and Geosciences, v. 18, p. 899–947.

Jollands M. C., Bloch E. and Muntener O. (2020) New Ti-in-quartz diffusivities reconcile natural Ti zoning with time scales and temperatures of upper crustal magma reservoirs. *Geology* **48**, 654–657.

Joshi M. S., Kotru P. N. and Vagh A. S. (1968) Microtopographical studies of first order prism faces of synthetic quartz. *J. Cryst. Growth* **2**, 329–336.

Kalyani V., Vasile B. S., Ianculescu A., Testino A., Carino A., Buscaglia M. T., Buscaglia V. and Nanni P. (2015a) Hydrothermal Synthesis of SrTiO3: Role of Interfaces. *Cryst. Growth Des.* **15**, 5712–5725.

Kamenetsky V. S., MacRae C. M., Goemann K., Wilson N. C. and Vasyukova O. V. (2012) Cathodoluminescence properties of quartz eyes from porphyry-type deposits: Implications for the origin of quartz. *Am. Mineral.* **98**, 98–109.

Khatib, R., Backus, E. H., Bonn, M., Perez-Haro, M. J., Gaigeot, M. P., & Sulpizi, M. (2016). Water orientation and hydrogen-bond structure at the fluorite/water interface. *Scientific reports*, **6**, 24287.

Kossel W. (1927) Zur theorie des kristallwachstums. *Nachrichten von der Gesellschaft der Wissenschaften zu Göttingen, Math. Klasse*, 135–143.

Kubota N. and Mullin J. W. (1995) A kinetic model for crystal growth from aqueous solution in the presence of impurity. *J. Cryst. Growth* **152**, 203–208.

Kularatne K. and Audétat A. (2014) Rutile solubility in hydrous rhyolite melts at 750-900°C and 2kbar, with application to titanium-in-quartz (TitaniQ) thermobarometry. *Geochim. Cosmochim. Acta* **125**, 196–209. Available at:

Li, H. L., Xu, W. N., Jia, F. F., Li, J. B., Song, S. X., & Nahmad, Y. (2020). Correlation between surface charge and hydration on mineral surfaces in aqueous solutions: A critical review. *International Journal of Minerals Metallurgy and Materials*, **27**(7), 857-871.

Li Y. and Ishigaki T. (2002) Thermodynamic analysis of nucleation of anatase and rutile from TiO2 melt. *J. Cryst. Growth* **242**, 511–516.

Lopez Ortiz J. I., Quiroga E., Narambuena C. F. and Ramirez-Pastor A. J. (2019) Crystal Growth from Aqueous Solution in the Presence of Structured Impurities. *Cryst. Growth Des.* **19**, 134–140.

Lowers H. A. (2007) Application of the titaniq geothermometer. *GSA Denver Annu. Meet.*, 80225. Available at: https://gsa.confex.com/gsa/2007AM/finalprogram/abstract_129097.htm

Lutsko J. F., Van Driessche A. E. S., Durán-Olivencia M. A., Maes D. and Sleutel M. (2016) Step Crowding Effects Dampen the Stochasticity of Crystal Growth Kinetics. *Phys. Rev. Lett.* **116**, 015501.

Lynne B. Y., Campbell K. A., James B. J., Browne P. R. J. and Moore J. (2007) Tracking crystallinity in siliceous hot-spring deposits. *Am. J. Sci.* **307**, 612–641.

Lyu Y., Wang Y., Wang S., Liu B. and Du H. (2019) Potassium Hydroxide Concentration-Dependent Water Structure on the Quartz Surface Studied by Combining Sum-Frequency Generation (SFG) Spectroscopy and Molecular Simulations. *Langmuir* **35**, 11651–11661.

Maydagán L., Franchini M., Rusk B., Lentz D., McFarlane C., Impiccini A., Rios F. J. and Rey R. (2015) Porphyry to epithermal transition in the Altar Cu-(Au-Mo) deposit, Argentina, studied by cathodoluminescence, LA-ICP-MS, and fluid inclusion analysis. *Econ. Geol.* **110**, 889–923.

McIntire, W.L. (1963) Trace element partition coefficients – a review of theory and applications to geology. *Geochim. Cosmochim. Acta* **27**, 1209-1264.

Mercer C. N. and Reed M. H. (2013) Porphyry Cu-Mo stockwork formation by dynamic, transient hydrothermal pulses: Mineralogic insights from the deposit at Butte, Montana. *Econ. Geol.* **108**, 1347–1377.

Mercer C. N. and Reed M. H. (2013) Porphyry Cu-Mo stockwork formation by dynamic, transient hydrothermal pulses: Mineralogic insights from the deposit at Butte, Montana. *Econ. Geol.* **108**, 1347–1377.

Miura H. (2020) Crystal Growth Hysteresis in Spiral Growth. *Cryst. Growth Des.* **20**, 245–254.

Miura H. and Tsukamoto K. (2013) Role of Impurity on Growth Hysteresis and Oscillatory Growth of Crystals. *Cryst. Growth Des.* **13**, 3588–3595.

Monecke T., Monecke J., James Reynolds T., Tsuruoka S., Bennett M. M., Skewes W. B. and Palin R. M. (2018) Quartz solubility in the H2O-NaCl system: A framework for understanding vein formation in porphyry copper deposits. *Econ. Geol.* **113**, 1007–1046.

Müller A., Herrington R., Armstrong R., Seltmann R., Kirwin D. J., Stenina N. G. and Kronz A. (2010) Trace elements and cathodoluminescence of quartz in stockwork veins of Mongolian porphyry-style deposits. *Miner. Depos.* **45**, 707–727.

Müller A., Herrington R., Armstrong R., Seltmann R., Kirwin D. J., Stenina N. G. and Kronz A. (2010) Trace elements and cathodoluminescence of quartz in stockwork veins of Mongolian porphyry-style deposits. *Miner. Depos.* **45**, 707–727.

Mysen B. (2019) Aqueous fluids as transport medium at high pressure and temperature: Ti4+ solubility, solution mechanisms, and fluid composition. *Chem. Geol.* **505**, 57–65.

Nachlas W. O. and Hirth G. (2015) Experimental constraints on the role of dynamic recrystallization on resetting the Ti-in-quartz thermobarometer. *J. Geophys. Res. Solid Earth* **120**, 8120–8137.

Nachlas W. O. and Hirth G. (2015) Experimental constraints on the role of dynamic recrystallization on resetting the Ti-in-quartz thermobarometer. *J. Geophys. Res. Solid Earth* **120**, 8120–8137.

Nachlas W. O., Thomas J. B. and Hirth G. (2018) TitaniQ deformed: Experimental deformation of out-of-equilibrium quartz porphyroclasts. *J. Struct. Geol.* **116**, 207–222.

Nielsen, L. C., De Yoreo, J. J., & DePaolo, D. J. (2013) General model for calcite growth kinetics in the presence of impurity ions. *Geochimica et Cosmochimica Acta* **115**, 100-114.

Nollet S., Hilgers C. and Urai J. L. (2006) Experimental study of polycrystal growth from an advecting supersaturated fluid in a model fracture. *Geofluids* **6**, 185–200.

Okada K., Yamamoto N., Kameshima Y., Yasumori A. and MacKenzie K. J. D. (2001) Effect of Silica Additive on the Anatase-to-Rutile Phase Transition. *J. Am. Ceram. Soc.* **84**, 1591–1596.

Ostapenko, G. T., Gamarnik, M. Y., Gorogotskaya, L. I., Kuznetsov, G. V., Tarashchan, A. N., and Timoshkova, L. P. (1987). Isomorphism of titanium substitution for silicon in quartz: experimental data. *Mineral Zh*. **9**, 30-40.

Ostapenko, G. T., Tarashchan, A. N., & Mitsyuk, B. M. (2007) Rutile-quartz geothermobarometer. *Geochemistry International*, **45**(5), 506-508.

Parashar, S., Lesnicki, D., & Sulpizi, M. (2018). Increased acid dissociation at the quartz/water interface. *Journal of Physical Chemistry Letters*, **9**(9), 2186-2189.

Penniston-Dorland S. C. (2001) Illumination of vein quartz textures in a porphyry copper ore deposit using scanned cathodoluminescence: Grasberg Igneous Complex, Irian Jaya, Indonesia. *Am. Mineral.* **86**, 652–666.

Pfeiffer-Laplaud M. and Gaigeot M. P. (2016) Adsorption of Singly Charged Ions at the Hydroxylated (0001) α-Quartz/Water Interface. *J. Phys. Chem. C* **120**, 4866–4880.

Piana S., Jones F. and Gale J. D. (2007) Aspartic acid as a crystal growth catalyst. *CrystEngComm* **9**, 1187–1191.

Pudack C., Halter W., Heinrich C. A. and Pettke T. (2009) Evolution of magmatic vapor to gold-rich epithermal liquid: The porphyry to epithermal transition at Nevados de Famatina, northwest Argentina. *Econ. Geol.* **104**, 449–477.

Quezada G. R., Rozas R. E. and Toledo P. G. (2017) Molecular Dynamics Simulations of Quartz (101)-Water and Corundum (001)-Water Interfaces: Effect of Surface Charge and Ions on Cation Adsorption, Water Orientation, and Surface Charge Reversal. *J. Phys. Chem. C* **121**, 25271–25282.

Rashkovich, L. N., & Kronsky, N. V. (1997) Influence of Fe^{3+} and Al^{3+} ions on the kinetics of steps on the {1 0 0} faces of KDP. *Journal of Crystal Growth*, **182**(3-4), 434-441.

Reed, M, and Dilles, J. (2020) Ore Deposits of Butte, Montana. *Montana Bureau of Mines and Geology Special Publication.*

Reed M., Rusk B. and Palandri J. (2013) The Butte magmatic-hydrothermal system: One fluid yields all alteration and veins. *Econ. Geol.* **108**, 1379–1396.

Roberts S. A. (1975) Early hydrothermal alteration and mineralization in the Butte district, Montana. Harvard University.

Roberts, S.A., 1975, Early hydrothermal alteration and mineralization in the Butte district, Montana: Ph.D. dissertation, Harvard University, 157 p.

Rusk B. G., Reed M. H. and Dilles J. H. (2008a) Fluid inclusion Evidence for Magmatic-hydrothermal Fluid Evolution in the Porphyry Copper-Molybdenum Deposit st Butte, Montana. *Econ. Geol.* **103**, 307–334.

Rusk B., Lowers H. and Reed M. (2008b) Trace elements in hydrothermal quartz: Relationships to cathodoluminescent textures and insights into vein formation. *Geology* **36**, 547–550.

Rusk B. G., Reed M. H., Dilles J. H. and Kent A. J. R. (2006) Intensity of quartz cathodoluminescence and trace-element content in quartz from the porphyry copper deposit at Butte, Montana. *Am. Mineral.* **91**, 1300–1312.

Rusk B., Reed, M. H. (2002) Scanning electron microscope–cathodoluminescence analysis of quartz reveals complex growth histories in veins from the Butte porphyry copper deposit. *Geology.* **30**, 727-730.

Sabyrov K., Burrows N. D. and Penn R. L. (2013) Size-dependent anatase to rutile phase transformation and particle growth. *Chem. Mater.* **25**, 1408–1415.

Sander M. V and Black J. E. (1988) Crystallization and recrystallization of growth-zoned vein quartz crystals from epithermal systems; implications for fluid inclusion studies. *Econ. Geol.* **83**, 1052–1060.

Sangwal K. (1993) Effect of impurities on the processes of crystal growth. *J. Cryst. Growth* **128**, 1236–1244.

Shane P., Smith V. C. and Nairn I. (2008) Millennial timescale resolution of rhyolite magma recharge at Tarawera volcano: insights from quartz chemistry and melt inclusions. *Contrib. to Mineral. Petrol.* **156**, 397–411.

Shannon R. D. and Pask J. A. (1965) Kinetics of the Anatase-Rutile Transformation. *J. Am. Ceram. Soc.* **48**, 391–398. Size-dependent anatase to rutile phase transformation and particle growth

Shimizu T. (2014) Reinterpretation of quartz textures in terms of hydrothermal fluid evolution at the Koryu Au-Ag deposit, Japan. *Econ. Geol.* **109**, 2051–2065.

Sillitoe R. H. (2010) Porphyry Copper Systems. *Econ. Geol.*, 3–41.

Sillitoe R. H. and Hedenquist J. W. (2003) Linkages between Volcanotectonic Settings, Ore-Fluid Compositions, and Epithermal Precious Metal Deposits. *Soc. Econ. Geol. Spec. Publ.* **10**, 000–000.

Sleutel M., Lutsko J. and Van Driessche A. E. S. (2018) Mineral Growth beyond the Limits of Impurity Poisoning. *Cryst. Growth Des.* **18**, 171–178.

Smedes H. Regional geologic setting of the Boulder batholith, Montana.

Stranski I. N. (1928) Zur theorie des kristallwachstums. *Zeitschrift für Phys. Chemie* **136**, 259–278.

Tanner D., Henley R. W., Mavrogenes J. A. and Holden P. (2013) Combining in situ isotopic, trace element and textural analyses of quartz from four magmatic-hydrothermal ore deposits. *Contrib. to Mineral. Petrol.* **166**, 1119–1142.

Tesoriero, A. J., & Pankow, J. F. (1996) Solid solution partitioning of Sr^{2+}, Ba^{2+}, and Cd^{2+} to calcite. *Geochimica et Cosmochimica Acta*, **60**(6), 1053-1063.

Thomas J. B., Bruce Watson E., Spear F. S., Shemella P. T., Nayak S. K. and Lanzirotti A. (2010) TitaniQ under pressure: the effect of pressure and temperature on the solubility of Ti in quartz. *Contrib. to Mineral. Petrol.* **160**, 743–759.

Thomas J. B., Watson E. B., Spear F. S. and Wark D. A. (2015) TitaniQ recrystallized: experimental confirmation of the original Ti-in-quartz calibrations. *Contrib. to Mineral. Petrol.* **169**, 27.

Thomas T. N., Land T. A., Casey W. H. and DeYoreo J. J. (2004) Emergence of supersteps on KH2PO4 crystal surfaces. *Phys. Rev. Lett.* **92**, 1–4.

Thomas, J. B., Nachlas, W. O., Osborne, Z. R., Hoff, C., & Watson, B. (2019, December). Extended and improved Ti-in-quartz solubility model. In *AGU Fall Meeting 2019*. AGU.

Tilling R. I. (1974) Composition and time relations of plutonic and associated Volcanic Rocks, Boulder Batholith Region, Montana. *Bull. Geol. Soc. Am.* **85**, 1925–1930.

Tuladhar A., Dewan S., Pezzotti S., Brigiano F. S., Creazzo F., Gaigeot M. P. and Borguet E. (2020) Ions Tune Interfacial Water Structure and Modulate Hydrophobic Interactions at Silica Surfaces. *J. Am. Chem. Soc.* **142**, 6991–7000.

van den kerkhof A. M., Kronz A., Simon K. and Scherer T. (2004) Fluid-controlled quartz recovery in granulite as revealed by cathodoluminescence and trace element analysis (Bamble sector, Norway). *Contrib. to Mineral. Petrol.* **146**, 637–652.

van der Eerden J. P. and Müller-Krumbhaar H. (1986) Formation of macrosteps due to time dependent impurity adsorption. *Electrochim. Acta* **31**, 1007–1012.

Van Rosmalen G. M. and Bennema P. (1990) Characterization of additive performance on crystallization: Habit modification. *J. Cryst. Growth* **99**, 1053–1060.

Vasyukova, O. V., Goemann, K., Kamenetsky, V. S., MacRae, C. M., & Wilson, N. C. (2013). Cathodoluminescence properties of quartz eyes from porphyry-type deposits: Implications for the origin of quartz. American Mineralogist, 98(1), 98-109.

Vearncombe J. R. (1993) Quartz vein morphology and implications for formation depth and classification of Archaean gold-vein deposits. *Ore Geol. Rev.* **8**, 407–424.

Volmer M. (1922) Zum problem des kristallwachstums. *Zeitschrift für Phys. Chemie* **102**, 267–275.

Walther, J.V. and Helgeson, H.C. (1977) Calculation of the thermodynamic properties of aqueous silica and the solubility of quartz and its polymorphs at high pressures and temperatures. *Am. J. Sci*. **277**, 1315-1351.

Wark D. A. and Watson E. B. (2006) TitaniQ: a titanium-in-quartz geothermometer. *Contrib. to Mineral. Petrol.* **152**, 743–754.

Wark D. A., Hildreth W., Spear F. S., Cherniak D. J. and Watson E. B. (2007) Pre-eruption recharge of the Bishop magma system. *Geology* **35**, 235–238.

Watkins J. M., DePaolo D. J. and Watson E. B. (2017) Kinetic Fractionation of Non-Traditional Stable Isotopes by Diffusion and Crystal Growth Reactions. *Rev. Mineral. Geochemistry* **82**, 85–125.

Watson B. E. (2004) A conceptual model for near-surface kinetic controls on the trace-element and stable isotope composition of abiogenic calcite crystals. *Geochim. Cosmochim. Acta* **68**, 1473–1488.

Wendler F., Okamoto A. and Blum P. (2016) Phase-field modeling of epitaxial growth of polycrystalline quartz veins in hydrothermal experiments. *Geofluids* **16**, 211–230.

Wilson C. J. N., Seward T. M., Allan A. S. R., Charlier B. L. A. and Bello L. (2012) A comment on: "TitaniQ under pressure: The effect of pressure and temperature on the solubility of Ti in quartz", by Jay B. Thomas, E. Bruce Watson, Frank S. Spear, Philip T. Shemella, Saroj K. Nayak and Antonio Lanzirotti. *Contrib. to Mineral. Petrol.* **164**, 359–368.

Zaitseva, N., Carman, L., Smolsky, I., Torres, R., & Yan, M. (1999) The effect of impurities and supersaturation on the rapid growth of KDP crystals. *Journal of crystal growth*, **204**(4), 512-524.

Zhang H. and Banfield J. F. (1999) New kinetic model for the nanocrystalline anatase-to-rutile transformation revealing rate dependence on number of particles. *Am. Mineral.* **84**, 528–535.

Zhang, C., Li, X., Almeev, R. R., Horn, I., Behrens, H., & Holtz, F. (2020). Ti-in-quartz thermobarometry and TiO_2 solubility in rhyolitic melts: New experiments and parametrization. *Earth and Planetary Science Letters*, **538**, 116213.

Zhu, Y., & Granick, S. (2001). Viscosity of interfacial water. *Physical Review Letters*, **87**(9), 096104.